

# The 400d Galaxy Cluster Survey weak lensing programme

## II. Weak lensing study of seven clusters with MMT/MegaCam<sup>★,★★,★★★</sup>

H. Israel<sup>1</sup>, T. Erben<sup>1</sup>, T. H. Reiprich<sup>1</sup>, A. Vikhlinin<sup>2</sup>, C. L. Sarazin<sup>3</sup>, and P. Schneider<sup>1</sup>

<sup>1</sup> Argelander-Institut für Astronomie, Auf dem Hügel 71, 53121 Bonn, Germany  
e-mail: hisrael@astro.uni-bonn.de

<sup>2</sup> Harvard-Smithsonian Center for Astrophysics, 60 Garden Street, Cambridge, MA 02138, USA

<sup>3</sup> Department of Astronomy, University of Virginia, 530 McCormick Road, Charlottesville, VA 22904, USA

Received 19 December 2011 / Accepted 30 July 2012

### ABSTRACT

**Context.** Evolution in the mass function of galaxy clusters sensitively traces both the expansion history of the Universe and cosmological structure formation. Robust cluster mass determinations are a key ingredient for a reliable measurement of this evolution, especially at high redshift. Weak gravitational lensing is a promising tool for, on average, unbiased mass estimates.

**Aims.** This weak lensing project aims at measuring reliable weak lensing masses for a complete X-ray selected sample of 36 high redshift ( $0.35 < z < 0.9$ ) clusters. The goal of this paper is to demonstrate the robustness of the methodology against commonly encountered problems, including pure instrumental effects, the presence of bright (8–9 mag) stars close to the cluster centre, ground based measurements of high- $z$  ( $z \sim 0.8$ ) clusters, and the presence of massive unrelated structures along the line-of-sight.

**Methods.** We select a subsample of seven clusters observed with MMT/MegaCam. Instrumental effects are checked in detail by cross-comparison with an archival CFHT/MegaCam observation. We derive mass estimates for seven clusters by modelling the tangential shear with an NFW profile, in two cases with multiple components to account for projected structures in the line-of-sight.

**Results.** We firmly detect lensing signals from all seven clusters at more than  $3.5\sigma$  and determine their masses, ranging from  $10^{14} M_{\odot}$  to  $10^{15} M_{\odot}$ , despite the presence of nearby bright stars. We retrieve the lensing signal of more than one cluster in the CL 1701+6414 field, while apparently observing CL 1701+6414 through a massive foreground filament. We also find a multi-peaked shear signal in CL 1641+4001. Shear structures measured in the MMT and CFHT images of CL 1701+6414 are highly correlated.

**Conclusions.** We confirm the capability of MMT/MegaCam to infer weak lensing masses from high- $z$  clusters, demonstrated by the high level of consistency between MMT and CFHT results for CL 1701+6414. This shows that, when a sophisticated analysis is applied, instrumental effects are well under control.

**Key words.** galaxies: clusters: general – cosmology: observations – gravitational lensing: weak – X-rays: galaxies: clusters

## 1. Introduction

Cosmological observables probing different physics are found to agree within their uncertainties on a  $\Lambda$ CDM cosmological model dominated by dark energy and dark matter (e.g., Kowalski et al. 2008; Schrabback et al. 2010; Larson et al. 2011). Investigating the unknown physical nature of dark energy ranks among the foremost questions for cosmologists. In particular, the presence or absence of evolution in dark energy density is expressed by the equation-of-state parameter  $w_{DE}$ . State-of-the-art measurements (e.g., Vikhlinin et al. 2009b; Mantz et al. 2010; Komatsu et al. 2011) are consistent with  $w_{DE} = -1$ , and hence with dark energy being an Einsteinian cosmological constant (e.g. Blanchard 2010). The tightest constraints on  $w_{DE}$  can be

\* Observations reported here were obtained at the MMT Observatory, a joint facility of the Smithsonian Institution and the University of Arizona.

\*\* Appendices are available in electronic form at <http://www.aanda.org>

\*\*\* Reduced and coadded MMT image files are only available in electronic form at the CDS via anonymous ftp to [cdsarc.u-strasbg.fr](mailto:cdsarc.u-strasbg.fr) (130.79.128.5) or via <http://cdsarc.u-strasbg.fr/viz-bin/qcat?J/A+A/546/A79>

achieved only by combining results from different probes showing complementary dependencies on cosmological parameters.

The evolution of galaxy clusters is understood to be determined by cosmological parameters through both cosmic expansion and hierarchical structure formation. Thus, clusters provide information to constrain cosmological parameters that is complementary to other tests (using e.g., the cosmic microwave background, type Ia supernovae, or baryonic acoustic oscillations). Information about the expansion history of the Universe and structure formation is encoded in the cluster mass function  $n(M, z)$ ; different cosmological models imply a different cluster mass function at high  $z$ , compared to the local mass function (e.g. Eke et al. 1996; Rosati et al. 2002; Voit 2005; Schuecker 2005; Reiprich 2006). Refining the original analytic model of Press & Schechter (1974), various fitting formulae have been developed based on numerical simulations (see Pillepich et al. 2010, for an overview). The measured cluster mass function not only gives strong evidence for the existence of dark energy (e.g. Vikhlinin et al. 2009b) but also adds valuable information to the joint constraints of cosmological parameters (for a recent review, see Allen et al. 2011).

Galaxy cluster cosmology relies on the accurate determination of cluster masses and a thorough understanding of the

different mass proxies in use. Cluster masses are most commonly inferred from a variety of X-ray observables (X-ray luminosity  $L_X$ , gas mass  $M_{\text{gas}}$ , the quantity  $Y_X = T_X M_{\text{gas}}$ ) or gravitational lensing (both weak and strong), but as well using the Sunyaev-Zel'dovich effect or the motions of member galaxies. For distant galaxy clusters which have low masses owing to the early epoch of structure formation they represent, the small number of available photons prohibits a detailed (spectral) X-ray analyses available for local clusters. Nevertheless, weighing a large number of high-redshift clusters will yield the best constraints on cosmological parameters. This strategy will be adopted by the upcoming generation of cluster surveys, e.g. using eROSITA (Predehl et al. 2010; Pillepich et al. 2012). Hence, scaling relations connecting quantities like  $L_X$  or  $M_{\text{gas}}$  with the total cluster mass will continue to play important roles and need to be understood and calibrated thoroughly.

Rooted in the thermodynamics of the intracluster medium (ICM), X-ray methods rely on assumptions of hydrostatic equilibrium, elemental composition, and, to a large extent, sphericity of the cluster's gravitational potential well (Sarazin 1988; Böhringer & Werner 2010). Weak gravitational lensing (WL; e.g. Schneider 2006) offers an alternative avenue for determining cluster masses, which is completely independent of these assumptions, directly mapping the projected mass distribution of matter, Dark and luminous.

Merging clusters deviate strongly from thermal and hydrostatic equilibrium, with a significant amount of the internal energy being present as kinetic energy of bulk motions or turbulent processes, e.g. merger shocks. Thus, the expectation from numerical simulations is that X-ray masses for merging systems might be biased after a significant merger, with a relaxation timescale of  $O(1 \text{ Gyr})$ . Simulations agree with the expectation from the hierarchical structure formation picture that mergers are more frequent at higher redshifts than in the local Universe (e.g. Cohn & White 2005). There is no consensus between different simulations yet which of several suggested physical effects dominates after the phase in which a disturbed morphology can be seen (e.g., Kravtsov et al. 2006; Nagai et al. 2007a; Stanek et al. 2010). Most importantly, bulk motions induce non-thermal pressure, providing support for the gas against gravity, thus possibly leading the hydrostatic mass to underestimate the true mass by 5–20% even in relaxed clusters (Rasia et al. 2006; Nagai et al. 2007b; Meneghetti et al. 2010).

Therefore, studying scaling relations of X-ray observables with weak lensing masses has become an important ingredient in refining cluster masses from X-ray observations (e.g., Zhang et al. 2008, 2010; Meneghetti et al. 2010). Relative uncertainties of the individual WL cluster masses are higher than those from X-rays, largely due to intrinsic shape noise. But the power of weak lensing comes through the statistical analysis of  $M_{\text{wl}}/M_X$  for the whole sample, under the assumption that WL mass estimates are, on average, unbiased. This means, while WL mass estimates for individual clusters are subject to an error due to the projection of filaments or voids along the line-of-sight, the stochastic nature of these errors makes them cancel out when averaging over a well-defined cluster sample. Statistical comparisons to X-ray masses (e.g., Meneghetti et al. 2010) help us to investigate WL systematic uncertainties, i.e. triaxiality (Corless & King 2009) and projection of unrelated LSS (Hoekstra 2003), to which X-ray observables are far less sensitive.

This article presents the second part of a series on weak lensing analyses following up the 400 Square Degree Galaxy Cluster (400d) Survey, initiated in Israel et al. (2010, hereafter Paper I). The 400d Survey presents a flux-limited sample of

galaxy clusters detected serendipitously in a re-analysis of all suitable ROSAT PSPC pointings (Burenin et al. 2007). From the resulting catalogue, Vikhlinin et al. (2009a, V09) drew the cosmological subsample of 36 X-ray luminous and distant clusters, for which high-quality *Chandra* X-ray observations were obtained and analysed. The *Chandra*-based cluster mass function resulting from the *Chandra* Cluster Cosmology Project was published by V09, for the complete redshift range of  $0.35 \leq z < 0.90$  spanned by the clusters in the cosmological subsample, as well as divided into three redshift bins. Building on this mass function, Vikhlinin et al. (2009b) constrained cosmological parameters, in particular  $w_{\text{DE}}$ .

Determining accurate weak lensing masses for the distant clusters in the 400d cosmological subsample opens the way to observationally test the assumptions Vikhlinin et al. (2009a,b) make for the scaling relations and their evolution. Put briefly, the WL follow-up of the 400d cosmological sample clusters provides us with a control experiment for the resulting X-ray mass function. With 36 clusters, the 400d WL sample ranks among the largest complete high- $z$  WL samples.

In Paper I, we presented the results of our feasibility study, performing a detailed lensing and multi-method analysis of CL 0030+2618. In particular, we showed the MegaCam instrument to be well suited for WL studies. As the next step of the project, we investigate seven further clusters from our sample, all of which were also observed with MegaCam at MMT. The resulting WL mass determination and the status after 8 out of 36 clusters have been analysed are the subjects of this paper.

We consistently assume a  $\Lambda$ CDM cosmology specified by the dimensionless Hubble parameter  $h = 0.72$  and matter and dark energy density parameters of  $\Omega_{\text{m}} = 0.30$  and  $\Omega_{\Lambda} = 0.70$ .

This paper is organised as follows: After giving a short overview on our data set and its reduction in Sect. 2, we give salient details of the WL analysis methods we used in Sect. 3. In Sect. 4, we take a closer look at two clusters which show a more complicated shear morphology and devise a two-cluster shear model. Comparing our MMT results to a CFHT weak lensing analysis of one of our clusters, we once more prove MMT weak lensing to be reliable and provide an external calibration (Sect. 5). In Sect. 6, we provide details of the error analysis for our main results, the cluster masses, which are then discussed in Sect. 7. Section 8 presents our summary and conclusion.

## 2. Methodology

### 2.1. MMT/MegaCam data for the 400d WL survey

Table 1 summarises the observations of the eight  $\delta > 0^\circ$  galaxy clusters with right ascensions<sup>1</sup>  $0^{\text{h}} < \alpha < 8^{\text{h}}30^{\text{m}}$  and  $13^{\text{h}}30^{\text{m}} < \alpha < 24^{\text{h}}$  for which MMT/MegaCam observations in the lensing ( $r'-i'$ ) band have been completed. As CL 0030+2618 was studied in detail in Paper I, this work focusses on the remaining seven clusters. Following the observation strategy described in Paper I, with nominal exposures of  $T^{\text{nom}} = (7500 \text{ s}, 6000 \text{ s}, 4500 \text{ s})$  in ( $g'r'i'$ ), these seven clusters were observed in the four out of five MMT observing runs performed for the 400d WL survey in which weather conditions permitted usable observations during at least parts of the scheduled time.

MEGACAM (McLeod et al. 2000), then located at the Fred Lawrence Whipple Observatory's 6.5 m MMT telescope, is a high-resolution ( $0.08'' \text{ px}^{-1}$ ), wide-field ( $\sim 24' \times 24'$  field-of-view) camera, consisting of a  $4 \times 9$  CCD mosaic.

<sup>1</sup> Their J2000 coordinates are given by the designations in Table 1.

**Table 1.** Specifications of the data sets for all eight clusters analysed so far.

Cluster	Filter	Observation dates	$T_{\text{exp}}^{\text{ini}}$ [s]	$T_{\text{exp}}^{\text{fin}}$ [s]	Seeing	$m_{\text{lim}}$	PhC
CL 0030+2618	$r'$	2004-10-06/07	15300	6600	0'82	25.9	I
	$g'$	2005-10-30/31,11-01	9150	7950	0'87	26.8	D
	$i'$	2005-10-31	6000	5700	1'03	25.1	D
CL 0159+0030	$r'$	2005-10-30/31,11-01	9900	3600	0'85	25.7	D
	$g'$	2005-11-01,	6000	4800	1'05	27.7	D
	$i'$	2005-10-31, 11-01	8100	5700	1'14	25.0	D
CL 0230+1836	$r'$	2004-10-06/07; 2005-11-08	9600	2700	0'68	25.1	I
	$g'$	2005-11-08	6000	4200	0'80	27.2	I
	$i'$	2005-10-31, 11-01/08	9600	3600	0'98	24.7	D
CL 0809+2811	$r'$	2005-11-08; 2008-01-09	9300	3000	0'72	25.4	D
	$g'$	2005-10-31/11-08	6000	3600	1'04	26.3	D
	$i'$	2005-10-31/11-01	7500	5700	0'82	26.1	D
CL 1357+6232	$r'$	2005-06-07	7200	2700	0'90	25.4	D
CL 1416+4446	$r'$	2005-06-08	7500	4200	0'81	25.8	D
CL 1641+4001	$r'$	2005-06-07	8100	6900	0'91	26.0	D
CL 1701+6414	$r'$	2005-06-08	7500	6000	0'89	25.8	D

**Notes.** For each cluster and filter, the dates of observation, total MegaCam exposure time  $T_{\text{exp}}^{\text{ini}}$ , usable final exposure time  $T_{\text{exp}}^{\text{fin}}$ , seeing, and  $5\sigma$  limiting magnitude (Eq. (2) in Paper I) for the final image stack are given. The last column refers to a direct (D) or indirect (I) photometric calibration (PhC, Sect. 2.2). CL 0030+2618 is the cluster analysed in Paper I.

The four ‘‘winter’’ clusters CL 0030+2618, CL 0159+0030, CL 0230+1836, and CL 0809+2811 have completed observations in the  $g'r'i'$  filters, while due to scheduling constraints, only the  $r'$ -imaging could be completed for the ‘‘summer’’ clusters CL 1357+6232, CL 1416+4446, CL 1641+4001, and CL 1701+6414. Therefore, a different strategy has to be adopted for parts of the data reduction (Sect. 2.3) and the background source selection (Sect. 2.4) for these single-band clusters compared to three-band clusters.

As indicated in Table 1, some clusters were observed in the same filter in more than one observing run. Using the data reduction described in Sect. 2.2, we produced coadded (stacked) images, for which net exposure times  $T_{\text{exp}}^{\text{fin}}$ , seeing,  $5\sigma$  limiting magnitudes, and photometric calibration method (Sect. 2.2) are given in the four last columns of Table 1.

The most striking fact to note are the drastic reductions from the initial raw data exposure times  $T_{\text{exp}}^{\text{ini}}$  to the  $T_{\text{exp}}^{\text{fin}}$  used in the coadded images. In a number of cases, the required seeing in the coadded image of  $\lesssim 1''$  in the lensing band and  $\lesssim 1''.2$  in the other bands could only be achieved by removing images such that  $T_{\text{exp}}^{\text{fin}} < T_{\text{exp}}^{\text{nom}}$ . As this inevitably reduces the limiting magnitude (Eq. (2) in Paper I), the final stacks represent a compromise between seeing and depth, aiming at an optimal WL signal. Similarly, compromises had to be made between maintaining a low level of anisotropy (Sect. 2.3) in the point spread function (PSF) and limiting magnitude. The ramifications of the heterogeneous data quality and the – in some cases – shallow exposure times, for which the good overall  $r'$ -band seeing could be obtained, will be addressed at several occasions in this article.

## 2.2. Data reduction and calibration

The data reduction for the 400d WL survey has been described in detail in Paper I. Therefore, we give only a brief recapitulation here and refer the interested reader to Paper I.

The first stage, including all tasks of elementary data reduction (de-biasing, flatfielding, de-fringing, construction of weight images, astrometry, relative photometry, and coaddition) are performed using the THELI pipeline for optical data

reduction introduced by Erben et al. (2005) and adapted to MMT/MegaCam in Paper I. Generally, we achieve a high level of homogeneity in the noise backgrounds of coadded images, with our pipeline effectively correcting the position-dependent transmissivity of MegaCam filters (Appendix A). The additive stray-light from very bright stars is not removed by THELI, but regions in the image in which source counts deviate significantly from the mean are masked as unreliable using the algorithm described by Dietrich et al. (2007). The mask images we produce in the second stage of data reduction for each coadded image also contain masks for saturated stars (cf. Paper I) and a few manually inserted masks for, e.g., asteroid trails<sup>2</sup>. The first seven panels of Fig. 1 present the central regions of our clusters as observed with MMT/MegaCam. For the three-band clusters, we prepared pseudo-colour images using the  $g'r'i'$  coadded images.

Applying the method of Hildebrandt et al. (2006), we computed absolute photometric zeropoints for our coadded images. As photometric reference for this calibration, the Sloan Digital Sky Survey Data Release Six (SDSS DR6, Adelman-McCarthy et al. 2008) was employed, with which six of our clusters overlap. This direct calibration also yields zeropoints for fields outside the SDSS footprint observed in the same filter in the same photometric night, as for the  $i'$ -band of CL 0230+1836 (Table 1). The remaining observations were done in nights in which no cluster with SDSS overlap was observed under photometric conditions. To these data, labelled with ‘‘I’’ in Table 1, we applied an indirect calibration described in Paper I, basically a rudimentary but effective stellar locus regression (High et al. 2009). Details concerning the results and accuracy of the photometric calibration can be found in Appendix A.

## 2.3. From images to shape catalogues

A detailed description of how we distill from a coadded image a galaxy shape catalogue, containing positions, ellipticity measurements, and photometric data for sources that can be

<sup>2</sup> The more common satellite streaks are masked already during the basic data reduction, prior to coaddition.

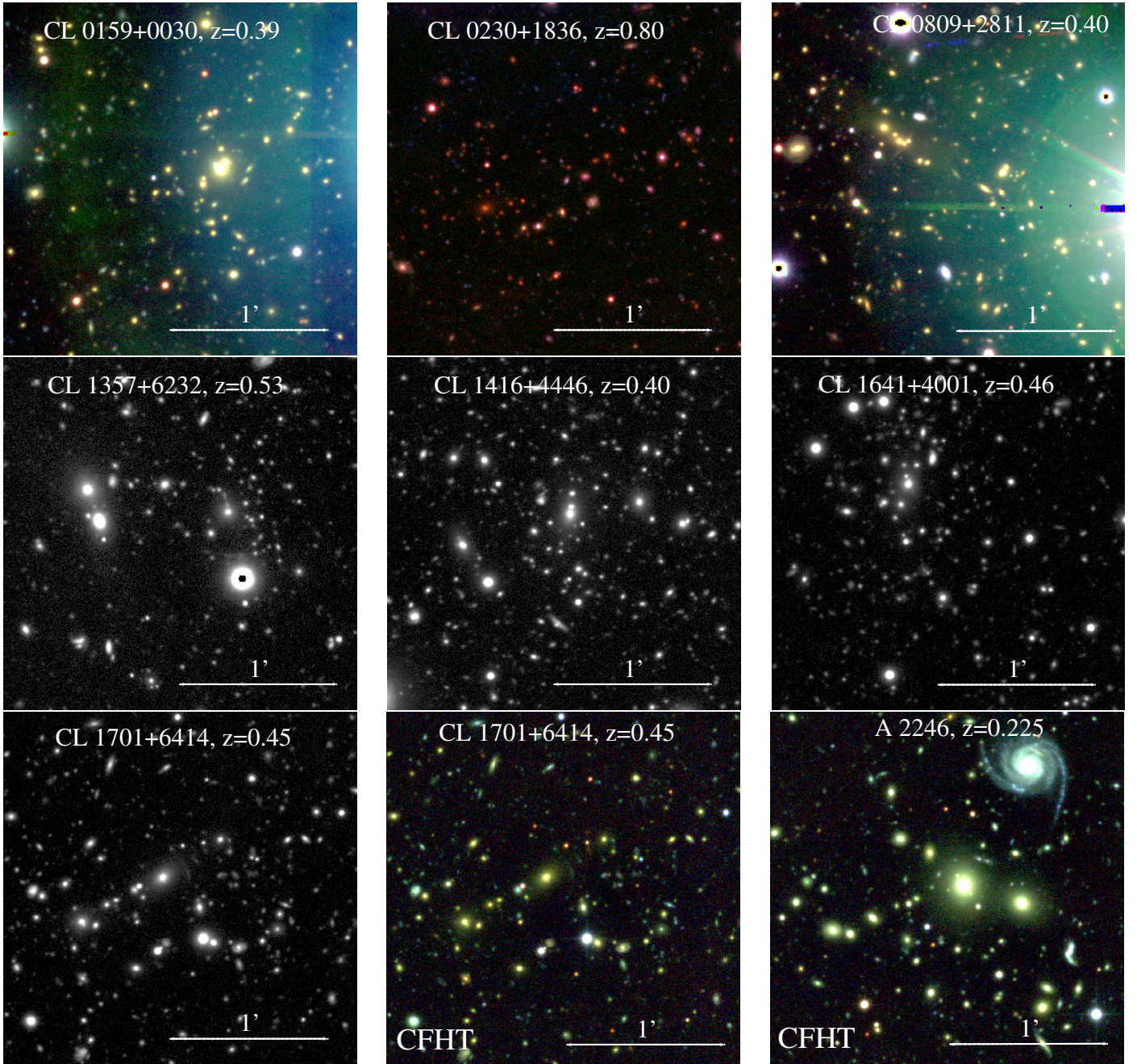


**Fig. 1.** Clusters discussed in this paper. We show pseudo-colour images for the cases where colour is available, using the MMT  $g'r'i'$  bands. For the CL 1701+6414 field, we also show pseudo-colour images using the CFHT  $g'r'i'$  bands, both for CL 1701+6414 and A 2246. We choose the ROSAT cluster coordinates as centre of the images. Note the variable background due to bright stars near CL 0159+0030 and CL 0809+2811.

considered galaxies can be found in Paper I. For the single-band clusters, we use straight-forward calls to **SExtractor** (Bertin & Arnouts 1996). For the three-band clusters, the convolution of images to the seeing in the poorest band and calls to **SExtractor** in double-detection mode, using the (unconvolved)  $r'$ -band image as the “detection image”, as described in Paper I are being performed.

We apply the “TS” shear measurement pipeline (Heymans et al. 2006; Schrabback et al. 2007; Hartlap et al. 2009), an implementation of the KSB+ algorithm (Kaiser et al. 1995; Erben et al. 2001), which determines moments of the brightness distribution for each source and corrects for the convolution with an anisotropic PSF. The PSF anisotropy is traced by measuring the brightness distribution of sources identified as stars in a plot of

their magnitude  $r'_{\text{AUTO}}$  against the half-light radius  $\vartheta$ . The values we used to define the boundaries of the stellar locus are given in Table 2. Only sources in the KSB catalogue, consisting of detections with a viable measurement of  $\vartheta$ , are further considered.

Consistent with our Paper I findings, MMT/MegaCam exhibits a smooth, albeit variable pattern of PSF anisotropy which can be modelled by a low-order ( $2 \leq d_{\text{ani}} \leq 5$ , see Table 2) polynomial in image coordinates such that the residual PSF anisotropy has a practically vanishing mean value and a dispersion  $0.005 \leq \sigma(e^{\text{ani}}) \leq 0.010$  in the  $r'$ -band image stacks. In terms of the uncorrected PSF anisotropy, however, there are considerable differences in the input images for different cluster fields. Excessive PSF anisotropy observed in several input frames – which thus had to be removed from the coadded

**Table 2.** Definitions of the galaxy shape and lensing catalogues.

Cluster field	$\vartheta_{\min}^*$ [px]	$\vartheta_{\min}^{\text{ana}}$ [px]	$\vartheta_{\max}^*$ [px]	$r'_{\min}^*$ [mag]	$r'_{\max}^*$ [mag]	$n_{\text{KSB}}$ [arcmin <sup>-2</sup> ]	$n_{\text{gal}}$ [arcmin <sup>-2</sup> ]	$d_{\text{ani}}$ (8)	$m_{\text{bright}}$ [mag]	$m_{\text{faint}}$ [mag]	$n_{\text{lc}}$ [arcmin <sup>-2</sup> ]	$\theta_{\text{out}}^{\text{opt}}$ (12)	$S_{\text{max}}$ (13)
	(1)	(2)	(3)	(4)	(5)	(6)	(7)		(9)	(10)	(11)		
CL 0030+2618	2.55	2.80	2.95	16.75	22.5	44.79	22.64	5	20.0	22.5	21.28	15'5	5.84
CL 0159+0030	2.65	2.95	3.10	17.5	22.5	37.27	18.91	3	20.0	24.6	11.58	10'5	4.12
CL 0230+1836	2.05	2.33	2.45	16.75	22.5	29.28	13.22	4	21.5	23.0	11.04	8'5	3.64
CL 0809+2811	2.35	2.66	2.80	17.0	22.5	33.39	16.56	2	22.5	24.8	10.31	13'5	5.39
CL 1357+6232	2.85	3.18	3.35	17.5	22.25	29.52	14.24	5	–	18.5	14.23	10'17	4.47
CL 1416+4446	2.55	2.80	2.95	16.75	22.5	42.50	21.51	5	–	18.5	21.50	4'83	4.25
CL 1641+4001	2.90	3.135	3.30	16.75	22.5	39.95	19.58	3	–	22.7	17.65	16'0 <sup>†</sup>	4.12
CL 1701+6414	2.60	2.95	3.10	16.75	22.5	40.71	20.72	4	–	21.9	19.47	15'5 <sup>†</sup>	3.75

**Notes.** The parameters  $\vartheta_{\min}^*$ ,  $\vartheta_{\max}^*$ ,  $r'_{\min}^*$ , and  $r'_{\max}^*$  delineate the stellar locus. The galaxy shape catalogue considers sources  $\vartheta > \vartheta_{\max}^*$  for  $r'_{\min}^* < r'_{\text{AUTO}} < r'_{\max}^*$  and  $\vartheta > \vartheta_{\min}^{\text{ana}}$  for  $r'_{\text{AUTO}} \geq r'_{\max}^*$  (Cols. (1) to (5)). The number densities  $n_{\text{KSB}}$  and  $n_{\text{gal}}$  of sources in the KSB and galaxy shape catalogues are shown in Cols. (6) and (7); followed by the degree  $d_{\text{ani}}$  of the polynomial for PSF anisotropy correction. Columns (9) to (13) present the photometric cuts  $m_{\text{bright}}$  and  $m_{\text{faint}}$ , defining the lensing catalogue with a source density  $n_{\text{lc}}$ . Using a filter scale of  $\theta_{\text{out}}$  in Eq. (1), we find a maximum shear peak significance  $S_{\text{max}}$ . CL 0030+2618 (Paper I) is included for completeness. <sup>(†)</sup> No significant decrease of  $S(\theta_{\text{out}})$  at the shear peak was found out to the largest probed value  $\theta_{\text{out}} = 16'$ . See Sect. 4 for more details on the CL 1701+6414 and CL 1641+4001 cases.

images – can be attributed to either tracking or focussing issues of the telescope. In most fields, no extreme outliers were present or could be easily identified. Only frames with average PSF ellipticity  $\langle e \rangle < 0.06$  entered the coaddition. No clear distinction leaving a sufficient number of low-anisotropy frames was possible for the CL 1641+4001 and CL 1701+6414 fields. In these cases, all frames with  $\langle e \rangle < 0.10$  were used for coaddition.

We classify as galaxies all sources fainter than the brightest unsaturated point sources ( $r'_{\text{AUTO}} > r'_{\min}^*$ ) and more extended than the PSF ( $\vartheta > \vartheta_{\max}^*$ ). Because even poorly resolved galaxies carry a lensing signal, we add sources  $r'_{\text{AUTO}} > r'_{\max}^*$  and  $\vartheta > \vartheta_{\min}^{\text{ana}}$  with  $\vartheta_{\min}^{\text{ana}} \approx 0.95\vartheta_{\max}^*$  to the galaxy shape catalogue (cf. Fig. 4 of Paper I). The parameters defining this catalogue for each field are tabulated in Table 2, together with its number density  $n_{\text{gal}} \approx n_{\text{KSB}}/2$ .

#### 2.4. Background selection

Cluster weak lensing studies rely on carefully selected catalogues of background galaxies, the carriers of the lensing signal. While falling short of yielding a reliable photometric redshift (photo- $z$ ) estimate for each individual galaxy, three-colour imaging makes possible a selection of foreground, cluster, and background sources based on their distribution in colour-colour-magnitude space (cf. Medezinski et al. 2010; Klein et al., in prep.). The method described below that we use for the three-band clusters is an improved version of the background selection in Paper I, to which we refer for concepts and terminology: While considering all galaxies fainter than  $m_{\text{faint}}$  in the lensing catalogue, galaxies brighter than  $m_{\text{bright}}$  are rejected. In the intermediate regime ( $m_{\text{bright}} < r' < m_{\text{faint}}$ ), we include galaxies whose  $g' - r'$  versus  $r' - i'$  colours are consistent with sitting in the background of the cluster, based on the – similarly deep – Ilbert et al. (2009) photo- $z$  catalogue (see Appendix B for more details).

For the single-band clusters, the background selection simplifies to a magnitude cut, meaning that lensing catalogue consists of all galaxies  $r' > m_{\text{faint}}$ . For each of these sources, our KSB+ implementation yields a PSF-corrected ellipticity  $\varepsilon = \varepsilon_1 + i\varepsilon_2$ , a noisy but, in principle, unbiased estimate of the reduced gravitational shear  $g = g_1 + ig_2$  (cf. Schneider 2006). We choose the values of  $m_{\text{faint}}$  (and  $m_{\text{bright}}$  where applicable) such

that the signal-to-noise ratio of the aperture mass estimator, or  $S$ -statistics (Schneider 1996) is optimised:

$$S(\boldsymbol{\theta}_{\text{c}}; \theta_{\text{out}}) = \frac{\sqrt{2} \sum_j \varepsilon_{t,j} Q_j(|\boldsymbol{\theta}_j - \boldsymbol{\theta}_{\text{c}}|/\theta_{\text{out}})}{\sigma_{\varepsilon} \sqrt{\sum_j Q_j^2(|\boldsymbol{\theta}_j - \boldsymbol{\theta}_{\text{c}}|/\theta_{\text{out}})}}. \quad (1)$$

By  $\varepsilon_{t,j} = \text{Re}[\varepsilon \exp(-2i\varphi)]$ , we denote the tangential ellipticity of the galaxy at position  $\boldsymbol{\theta}_j$ , which with respect to the point  $\boldsymbol{\theta}_{\text{c}}$  has a phase angle  $\varphi$ . Equation (1) considers the noise from intrinsic source ellipticity, measured as  $\sigma_{\varepsilon} = \langle \varepsilon_1^2 + \varepsilon_2^2 \rangle^{1/2}$ ; while  $Q_j(|\boldsymbol{\theta}_j - \boldsymbol{\theta}_{\text{c}}|/\theta_{\text{out}})$  is the Schirmer et al. (2007) filter function with outer radius  $\theta_{\text{out}}$ , maximising  $S$  for a cluster-like radial shear profile.

We evaluate Eq. (1) on a regular grid with 15'' mesh size. With the notable exception of CL 1701+6414 (Sect. 4.1), the signal peaks are found close to the ROSAT-determined cluster centres and can be easily identified with our clusters. The adopted values of  $m_{\text{bright}}$ ,  $m_{\text{faint}}$ , and  $\theta_{\text{out}}$ , yielding an optimal signal-to-noise ratio  $S_{\text{max}}$  are summarised in Table 2, as well as the number density  $n_{\text{lc}}$  in the lensing catalogue<sup>3</sup>. We refer to the grid cell in which  $S_{\text{max}}$  occurs as the cluster shear peak and discuss the significance of our cluster detections in Sect. 7.1.

#### 2.5. Shear profile modelling

Pursuing the approach adopted in Paper I, we model the tangential ellipticity profile  $\varepsilon_t(\theta)$  of our clusters with the reduced shear profile  $g(\theta; r_{200}, c_{\text{NFW}})$  (Bartelmann 1996; Wright & Brainerd 2000) corresponding to the Navarro et al. (1995, 1996, 1997, NFW) density profile. From the estimate of the radius  $r_{200}$  – defined such that the density of the enclosed matter exceeds the critical density  $\rho_{\text{c}}(z_{\text{d}})$  at the cluster redshift  $z_{\text{d}}$  by a factor of  $\Delta = 200$  – we infer the cluster mass  $M_{200}$  via

$$M_{\Delta} = \Delta \frac{4\pi}{3} \rho_{\text{c}}(z_{\text{d}}) r_{\Delta}^3. \quad (2)$$

The best matching cluster mass profile parameters  $r_{200}$  and  $c_{\text{NFW}}$  minimise the merit function

$$\chi^2 = \sum_{i=1}^N \frac{|g_i(\theta_i; r_{200}, c_{\text{NFW}}) - \tilde{\varepsilon}_{t,i}(\theta_i)|^2}{\tilde{\sigma}_i^2(\theta_i) (1 - |g_i(\theta_i; r_{200}, c_{\text{NFW}})|)^2}, \quad (3)$$

<sup>3</sup> In addition to the photometric cuts, we restrict ourselves to high-quality sources defined by  $|\varepsilon| < 0.8$ , SExtractor detection significance  $\nu > 4.5$  and  $\text{tr}(\mathbf{P}^{\varepsilon}) > 0.1$  for the KSB pre-seeing polarisability tensor.

**Table 3.** Additional parameters defining the “default” cluster models.

Cluster	$z_d$ (1)	$\langle\langle\beta\rangle\rangle$ (2)	$\sigma(\langle\beta\rangle)$ (3)	$\hat{f}_d$ (4)	$f_1(\theta)$ (5)	$\alpha_{c,J2000}$ (6)	$\delta_{c,J2000}$ (7)	$r_{\min}$ (8)	$r_{\max}$ (9)	$\theta_{\min}$ (10)	$\theta_{\max}$ (11)	$\Delta\theta$ (12)
CL 0030+2618	0.50	0.348 <sup>†</sup>	0.024 <sup>†</sup>	0.152 <sup>†</sup>	✓	00 <sup>h</sup> 30 <sup>m</sup> 33 <sup>s</sup> .6	+26°18′16″	0.2 Mpc	5.0 Mpc	0′56	14′04	23″
CL 0159+0030	0.39	0.447	0.023	0.087	✓	01 <sup>h</sup> 59 <sup>m</sup> 18 <sup>s</sup> .2	+00°30′09″	0.2 Mpc	5.0 Mpc	0′65	16′20	79″ <sup>§</sup>
CL 0230+1836	0.80	0.168	0.020	0.321	✓	02 <sup>h</sup> 30 <sup>m</sup> 26 <sup>s</sup> .6	+18°36′22″	0.2 Mpc	5.0 Mpc	0′46	11′42	20″
CL 0809+2811	0.40	0.437	0.023	0.105	✓	08 <sup>h</sup> 09 <sup>m</sup> 41 <sup>s</sup> .0	+28°11′58″	0.2 Mpc	5.0 Mpc	0′64	15′95	178″ <sup>§</sup>
CL 1357+6232	0.53	0.324	0.024	0.198	–	13 <sup>h</sup> 57 <sup>m</sup> 19 <sup>s</sup> .4	+62°32′42″	0.2 Mpc	5.0 Mpc	0′54	13′62	50″
CL 1416+4446	0.40	0.437	0.023	0.136	–	14 <sup>h</sup> 16 <sup>m</sup> 28 <sup>s</sup> .1	+44°46′38″	0.2 Mpc	5.0 Mpc	0′64	15′95	19″
CL 1641+4001	0.46	0.381	0.024	0.127	–	16 <sup>h</sup> 41 <sup>m</sup> 52 <sup>s</sup> .3	+40°01′27″	0.2 Mpc	5.0 Mpc	0′59	14′70	95″
CL 1701+6414	0.45	0.381	0.024	0.134	–	17 <sup>h</sup> 01 <sup>m</sup> 22 <sup>s</sup> .5	+64°14′08″	0.2 Mpc	5.0 Mpc	0′60	14′88	66″

**Notes.** Columns (1) to (5) tabulate the cluster redshift  $z_d$ , the average  $\langle\langle\beta\rangle\rangle$  and dispersion  $\sigma(\langle\beta\rangle)$  of the distance ratio estimated from the CFHTLS Deep fields, the estimated fraction  $\hat{f}_d$  of residual foreground galaxies in the lensing catalogue, based on the same Ilbert et al. (2006) photo- $z$  catalogue, and whether or not a dilution correction  $f_1(\theta)$  has been applied. Columns (6) and (7) present the celestial coordinates of the assumed cluster centre, with respect to which the fitting range  $r_{\min} \leq \theta \leq r_{\max}$  in Cols. (8) and (9) is defined. Columns (10) and (11) repeat the fitting range in terms of angular separation. Finally, we give the separation between ROSAT and lensing centres in Col. (12). <sup>(†)</sup> We use an improved fit for the redshift distribution and corrected  $\hat{f}_d$  for CL 0030+2618 with respect to Paper I. <sup>(§)</sup> Lensing centre is within a large masked area, which probably diminished the accuracy.

which we evaluate on a regular grid in  $r_{200}$  and  $c_{\text{NFW}}$ . By  $\tilde{\epsilon}_{t,i}$ , we denote the tangential component of the scaled ellipticity  $\tilde{\epsilon}_i = f_0 f_1(\theta_i) \epsilon_i$  for the  $i$ th galaxy, including a global shear calibration factor  $f_0 = 1.08$  (see Paper I and Hartlap et al. 2009) as well as a separation-dependent correction  $f_1(\theta)$  for the shear dilution by cluster members (detailed below). Accordingly, the error scales as  $\tilde{\sigma}_i(\theta_i) = f_0 f_1(\theta_i) \sigma_\epsilon / \sqrt{2}$  with  $\sigma_\epsilon$  from Sect. 2.4. The index  $i$  runs over all lensing catalogue galaxies with separations within the fitting range  $\theta_{\min} \leq \theta \leq \theta_{\max}$  from the assumed ROSAT cluster centre, presented in Table 3. We choose separations  $\theta_{\min}$  and  $\theta_{\max}$  corresponding to distances of  $r_{\min} = 0.2$  Mpc and  $r_{\max} = 5.0$  Mpc at the respective cluster redshift. The denominator of Eq. (3) accounts for the dependence of the noise on  $g_i(\theta_i)$  itself (Schneider et al. 2000).

**Source redshift distributions.** The reduced shear  $g_i(\theta_i)$  exerted by a lens on the image of a background source further depends on the ratio of angular diameter distances between deflector and source  $D_{\text{ds}}$  and source and observer  $D_s$ . For each of our fields, we estimate a catalogue-average  $\langle\beta\rangle = \langle D_{\text{ds}}/D_s \rangle_{i=1\dots N}$  using the Ilbert et al. (2006) photo- $z$  catalogue, drawn from the CFHTLS Deep fields with similar source number counts as a function of magnitude  $r'$  as our MMT observations. Applying the same photometric cuts as to the MMT data to the catalogues of reliable photo- $z$  sources (cf. Paper I), we thus obtain proxy redshift distributions for our cluster observations. We repeat the fit of a van Waerbeke et al. (2001) redshift distribution and subsequent calculation of  $\langle\beta\rangle$  as described in Paper I – but to an improved accuracy – for all combinations of MMT and CFHT Deep fields. As an input to Eq. (3), we use the mean  $\langle\langle\beta\rangle\rangle_{k=1\dots 4}$  (Table 3) measured for the Deep fields and consider its dispersion  $\sigma(\langle\beta\rangle)$  in the error analysis (Sect. 6.1).

We further employ the Ilbert et al. (2006) catalogue to test the efficacy of the background selection. Applying the respective background selection to the Deep 1 photo- $z$  catalogue, we determine the fraction  $\hat{f}_d$  of residual foreground galaxies in the lensing catalogues (Table 3, cf. Sect. 6.1).

**Dilution by cluster members.** Although the selection of lensing catalogue galaxies is designed to include preferentially background galaxies, we detect an increase in the fraction  $f_{\text{isc}}(\theta)$  of galaxies whose  $g' - i'$  colours are consistent with the red

sequences at  $z_d$  towards the centres of our three-band clusters. Tentative red sequence galaxies are defined using an interval in  $g' - i'$  empirically found in the  $g' - i'$  versus  $i'$  colour–magnitude diagram, around the expected colour of a Coleman et al. (1980) early-type galaxy calculated with the Bolzonella et al. (2000) photo- $z$  code. To correct for the dilution effect of these likely unlensed sources in the shear catalogues, the corrective factor  $f_1(\theta) = 1 + \Sigma(\theta)/[\Sigma(\theta) + B]$  is introduced. The NFW surface mass profile  $\Sigma(\theta)$  and background term  $B$  are determined by a fit to  $f_{\text{isc}}(\theta)$ . We apply this correction only to the three-band clusters for which the  $g' - i'$  information is available (see Table 3). Because we have  $f_1(\theta)$  measured for only four clusters, three of which suffer from large masks in the crucial central regions, we decide against using an averaged  $f_1(\theta)$  for the single-band clusters at this stage of the survey.

## 2.6. Surface mass maps

While we use the tangential shear profile to determine cluster masses, we are interested as well in the (projected) mass distributions of our clusters in order to distinguish possibly merging systems of disturbed morphology from relaxed clusters. The non-local relation between shear and convergence  $\kappa = \Sigma/\Sigma_{\text{crit}}$  can be inverted, as shown by Kaiser & Squires (1993). We perform mass reconstructions using the Seitz & Schneider (1996, 2001) finite-field inversion algorithm. Concerning the mass sheet degeneracy (cf. Schneider 2006), the mean  $\kappa$  along the edge of the field-of-view is assumed to vanish.

The dimensionless surface mass  $\tilde{\kappa} \propto \kappa$ , with an arbitrary normalisation, is calculated on a regular grid. Because each cluster field has to be divided into an integral number of grid cells, the mesh size cannot be fixed to the same constant for all clusters, but varies slightly, with a mean of 40′.93 and a standard deviation of 0′.36. For all clusters and grid points, the algorithm accounts for lensing catalogue galaxies within a radius of  $\theta_s = 2'$ . The input shear field is smoothed with a truncated Gaussian filter of 0.555  $\theta_s$  full-width half-maximum, which drops to zero at  $\theta_s$ .

## 3. Results for normal clusters

In this Section, we present the outcome of the WL modelling, by showing a comprehensive figure combining the lensing signal maps, shear profile, and NFW modelling for each cluster. CL 1357+6232 (Fig. 2) serves as our example; for more

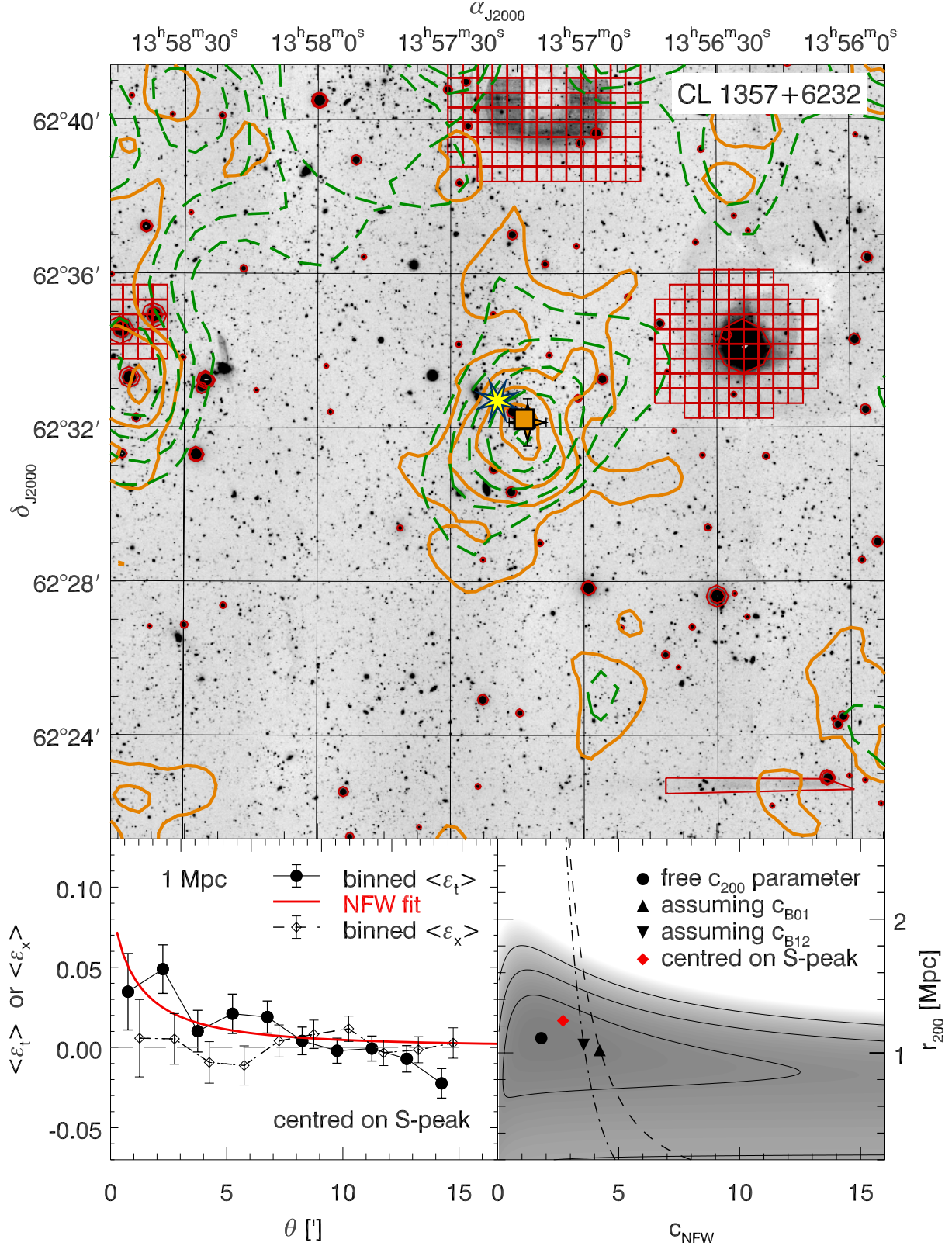


**Fig. 2.** Lensing results for CL 1357+6232. *Upper panel:* MegaCam  $r'$ -band image (cut-out of  $\sim 20'$  side length), overlaid with  $S$ -statistics (orange solid) and  $\bar{\kappa}$  (green dashed) contours. Contours start at  $S = 1.0$  and  $\bar{\kappa} = 0.01$ , with increments of  $\Delta S = 1.0$  and  $\Delta\bar{\kappa} = 0.01$ , respectively. The eight-pointed star symbol marks the ROSAT cluster centre, while the filled square shows the shear peak grid cell. A star symbol with error bars denotes the lensing centre from bootstrapping. Regions inside red polygons are masked out of the analysis. *Lower left panel:* profiles of the binned tangential ( $\langle \varepsilon_t \rangle$ , filled circles) and binned cross ( $\langle \varepsilon_x \rangle$ , open diamonds) ellipticities. Error bars give the bin dispersions. The thick blue curve denotes the best-fit NFW model (Eq. (3)). Here, the  $S$ -peak was assumed as centre. *Lower right panel:*  $\Delta\chi^2(r_{200}, c_{\text{NFW}})$  with respect to its minimum (filled circle), shown as grey shading and contours indicating  $1\sigma$ ,  $2\sigma$ , and  $3\sigma$  confidence. An upward (downward) triangle on a dashed (dash-dotted) curves mark the best-fit values assuming the B01 and B12 mass- $c_{200}$ -relations. A diamond marks cluster parameters assuming the  $S$ -peak as centre.

details on the other clusters, we refer to Figs. D.1 to Figs. D.4 in Appendix D. Two clusters, CL 1701+6414 (Fig. 3) and CL 1641+4001 (Fig. 5), exhibit multiple shear peaks and shear profiles that are very flat but positive over a large radial range. The more involved modelling of these “special cases” – as opposed to the “normal clusters” – is described in Sect. 4.

In the upper panel of Fig. 2, we present the  $S$ -statistics (solid orange) and  $\bar{\kappa}$ -contours (green dashed) for CL 1357+6232, overlaid on a cut-out of the MegaCam  $r'$ -band image with  $\sim 20'$  side length. Masked areas can be identified from the red polygons (mostly squares). The ROSAT centre is given by a yellow, eight-pointed star symbol. A filled orange square denotes the shear peak grid cell (Sect. 2.4), while a star symbol with error bars shows the WL centre from bootstrapping (Sect. 3.2).

The lower left panel of Fig. 2 shows the binned shear profile  $\langle \varepsilon_t(\theta) \rangle$  as filled circles with error bars giving the dispersion of the measured values. Open diamonds give the cross component  $\langle \varepsilon_x(\theta) \rangle$  which is on average expected to be consistent with zero for cluster lenses. The red solid line denotes the best-fit NFW model. Finally, the lower right panel of Fig. 2 presents  $\Delta\chi^2(r_{200}, c_{\text{NFW}}) = \chi^2 - \min(\chi^2)$ . The minimum is indicated by filled circle; contour lines enclose the 99.73%, 95.4%, and 68.3% confidence regions, (i.e.  $\Delta\chi^2 = 2.30, 6.17$ , and 11.30). An upward triangle marks the minimum of  $\Delta\chi^2$  when restricting  $c_{\text{NFW}}$  to its Bullock et al. (2001, dashed line) value.

### 3.1. Cluster detection and lensing morphology

We successfully detect all observed 400d clusters using the  $S$ -statistics with at least  $3.5\sigma$  significance and are able to derive a weak lensing mass estimate for each cluster. Table 2 summarises the maximum detection levels  $S$  and the optimal filter scales  $\theta_{\text{out}}^{\text{opt}}$ . The most significant detection is CL 0030+2618 at  $z = 0.50$  with  $S = 5.84$  (Paper I); the formally least significant detection is CL 0230+1836 at  $z = 0.80$  with  $S = 3.64$ . The  $S = 3.75$  measured for CL 1701+6414 has a contribution from the nearby cluster A 2246 at  $\theta \approx 270''$  separation (Sect. 4.1), rendering it the least secure detection: for  $\theta_{\text{out}} = 220''$ , we detect CL 1701+6414 at the  $2.5\sigma$  level. By detecting CL 0230+1836, we demonstrate the feasibility of MegaCam WL studies out to the highest redshifts accessible for current ground-based weak lensing.

In general, we find a very good agreement between the signal morphologies, of the  $S$ -statistics and mass reconstruction, i.e. we detect the same structures at comparable relative signal strength. This result reaffirms that our detections are not caused by artifacts in the (independent) analysis methods.

### 3.2. WL cluster centres

We define a “default” model for the NFW modelling of each cluster, determined by the parameters in Table 3, i.e. the cluster centre, fitting range,  $\langle \langle \beta \rangle \rangle$ , and dilution correction. We acknowledge that a careful and consistent treatment of cluster centres is important to prevent masses from being biased. In the default model, we use the lensing-independent ROSAT X-cluster centres. For comparison, we also consider cluster centres based on the  $S$ -map, which provide us with a high signal-to-noise shear profile. The shear peaks (most significant cell in the  $S$ -map) are thoroughly studied with respect to the background selection parameters and their interpretation as significances (Sect. 7.1).

The  $S$ -peak of CL 0159+0030 is located conspicuously close to the edge of an extended shear plateau which is likely caused by a large masked area<sup>4</sup> around a bright star ( $V = 8.3$ , Figs. 1 and D.1). Similarly bright stars are present also close to CL 0230+1836 and CL 0809+2811 (Figs. D.2 and D.3). In the latter case, where the  $S$ -peak lies within the masked area, we discuss the effect of masking in Sect. 7.5.

As noise can boost  $S$  in a grid cell compared to its neighbours, we perform a bootstrap resampling of the  $S$ -map (cf. Paper I) in two cases, CL 1357+6232 and CL 1416+4446. Averaging over  $10^5$  realisations, for which we draw  $N_{\text{lc}}$  galaxies with repetitions from the lensing catalogue, we determine a lensing centre. We find the bootstrap lensing centres to be in good agreement with the shear peaks of CL 1357+6232 and CL 1416+4446, well within the standard deviation of the bootstrap samples. In Sect. 7.2, the implications of the choice of cluster centres for the mass estimates are discussed.

### 3.3. Shear profiles and NFW modelling

Five of our clusters can be classified as “normal”, characterised by centrally increasing  $\langle \varepsilon_t \rangle(\theta)$  profiles, in good agreement with the NFW models. As expected, their  $\langle \varepsilon_x \rangle(\theta)$  profiles are consistent with zero, with fluctuations that can be explained by shape noise. The two other clusters, CL 1641+4001 and CL 1701+6414 show a more complicated morphology in their  $S$ -maps (Sect. 4).

Table 4 provides the cluster parameters resulting from the NFW modelling. Uncertainties in  $r_{200}$  and  $c_{\text{NFW}}$  are calculated from  $\Delta\chi^2$  corresponding to a 68.3% confidence limit for one interesting parameter ( $\Delta\chi^2 = 1$ ). Cluster masses  $M_{200}^{\text{wl}}(r_{200})$  are inferred via Eq. (2).

### 3.4. Mass-concentration relations

Weak lensing hardly constrains cluster concentration parameters, because the dependence on  $c_{\text{NFW}}$  is highest in the cluster centre where few lensed sources are observed. This is reflected also in our results, with huge uncertainties measured for  $c_{\text{NFW}}$  in several objects. Hence, we perform two additional measurements, in which we fix the value of  $c_{\text{NFW}}$ .

The first mass-concentration relation we assume is the one found by Bullock et al. (2001, B01) for simulated clusters:

$$c_{\text{B01}} = \frac{c_{\text{B01},0}}{1+z} \left( \frac{M_{\text{vir}}}{M_*} \right)^{\alpha_{\text{B01}}} \quad (4)$$

with  $c_{\text{B01},0} = 9.0$ ,  $\alpha_{\text{B01}} = -0.13$ , and  $M_* = 1.3 \times 10^{13} h^{-1} M_{\odot}$ . In their simulations, B01 observe a scatter of  $\sigma(\log c_{\text{vir}}) = 0.18$  for a fixed  $M_{\text{vir}}$ .

For our purposes, we insert  $M_{200}^{\text{wl}}(r_{200})$  for  $M_{\text{vir}}$  in Eq. (4). Due to the weak dependence of  $c_{\text{B01}}$  on  $M_{\text{vir}}$  this results only in a very small underestimate of  $c_{\text{B01}}$ . For two of the total of eight clusters we analysed,  $c_{\text{B01}}$  is very close to the  $c_{\text{NFW}}$  obtained by lensing, while for others it differs strongly (see Table 4).

Assuming the B01 mass-concentration relation, we apply a Gaussian prior  $p_c(r_{200}, c_{200})$  with standard deviation  $\sigma(\log c_{200}) = 0.18$  to the tabulated values of  $\Delta\chi^2(r_{200}, c_{\text{NFW}})$  for each of our clusters, and marginalise over the  $c_{200}$  dimension. The radii  $r_{200,\text{B01}}$  and the corresponding masses

<sup>4</sup> Due to the filtering with large scales  $\theta_{\text{out}}$ , we measure a signal also in masked areas. Naturally, the correlation between neighbouring grid cells is even higher than in unmasked regions.

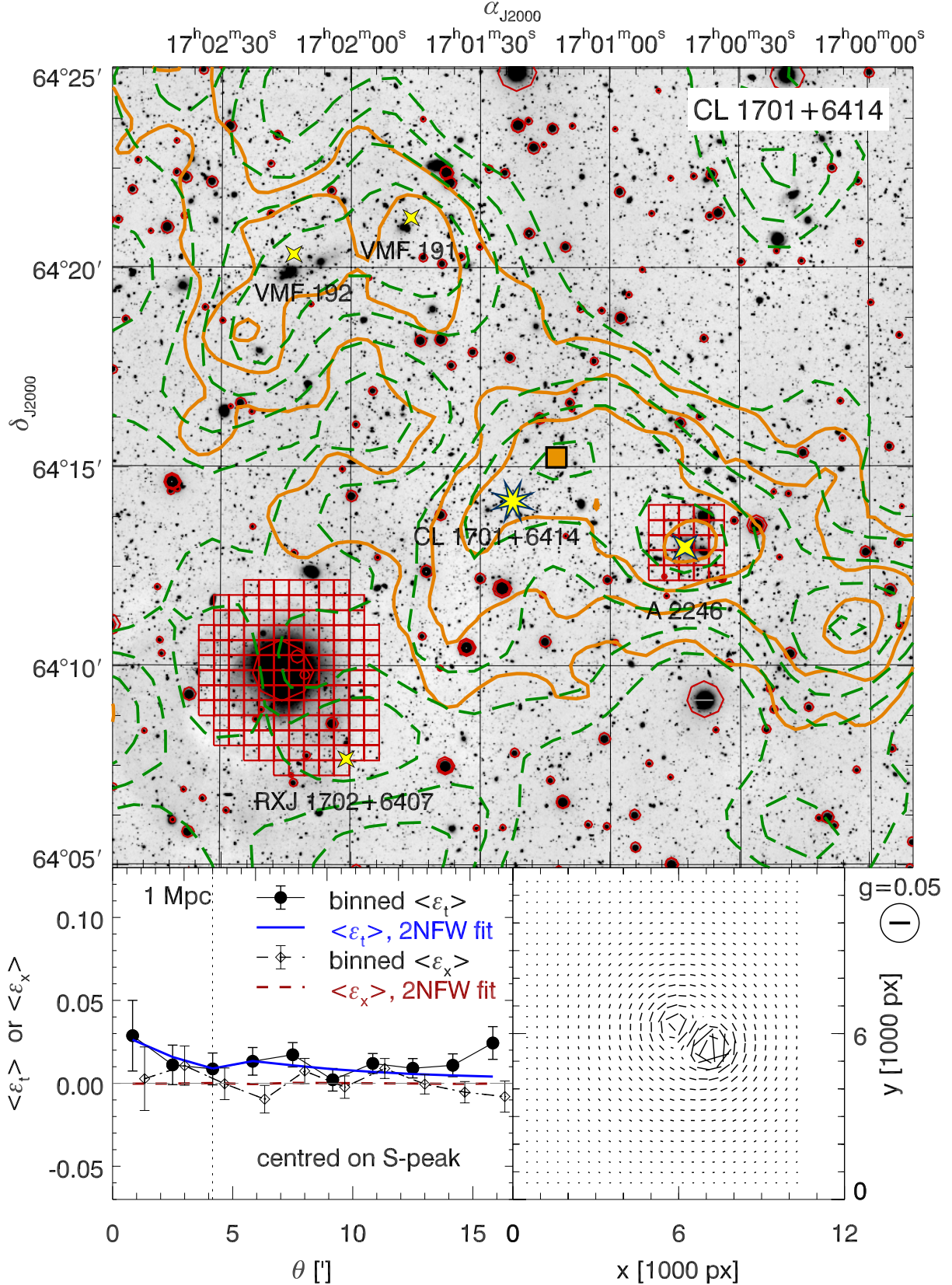


**Fig. 3.** Shear signal in the CL 1701+6414 field and its best-fit model with two NFW components accounting for CL 1701+6414 and A 2246. *Upper plot:* the layout follows Fig. 2. The ROSAT position of A 2246 is marked by a big four-pointed star symbol. Smaller star symbols denote positions of further X-ray clusters. *Lower left plot:* the layout follows Fig. 2. The solid blue and dashed red lines give the mean tangential and cross shear components, averaged in bins around the CL 1701+6414 shear peak, as expected from the two-cluster model. The separation of the two main clusters is indicated by a vertical dotted line. *Lower right plot:* the orientations and amplitudes of the shear, as expected from the best-fit two-cluster model, calculated on a regular grid.

**Table 4.** Synopsis of cluster parameters and resulting weak lensing masses.

Cluster	$r_{200}$ [Mpc]	$c_{\text{NFW}}$	$M_{200}^{\text{wl}}(r_{200})$ [ $10^{14} M_{\odot}$ ]	$r_{200, \text{B01}}$ [Mpc]	$c_{\text{B01, NFW}}$	$M_{200, \text{B01}}^{\text{wl}}(r_{200, \text{B01}})$ [ $10^{14} M_{\odot}$ ]	$r_{200, \text{B12}}$ [Mpc]	$c_{\text{B12, NFW}}$	$M_{200, \text{B12}}^{\text{wl}}(r_{200, \text{B12}})$ [ $10^{14} M_{\odot}$ ]
	(1)	(2)	(3)	(4)	(5)	(6)	(7)	(8)	(9)
CL 0030+2618	$1.52^{+0.14}_{-0.16}$	$1.7^{+1.3}_{-0.8}$	$7.25^{+2.19}_{-2.06}$	$1.39^{+0.13}_{-0.14}$	$3.9^{+2.0}_{-1.3}$	$5.50^{+1.65}_{-1.50}$	$1.45^{+0.13}_{-0.15}$	$3.4^{+1.7}_{-1.1}$	$6.23^{+1.87}_{-1.76}$
CL 0159+0030	$1.37^{+0.18}_{-0.22}$	> 20	$4.67^{+2.09}_{-1.91}$	$1.34^{+0.21}_{-0.25}$	$4.3^{+2.2}_{-1.5}$	$4.39^{+2.44}_{-2.03}$	$1.31^{+0.22}_{-0.27}$	$3.6^{+1.9}_{-1.2}$	$4.10^{+2.46}_{-1.76}$
CL 0230+1836	$1.54^{+0.28}_{-0.32}$	$2.8^{+3.7}_{-1.6}$	$10.78^{+7.01}_{-5.42}$	$1.49^{+0.26}_{-0.31}$	$3.0^{+1.5}_{-1.0}$	$9.68^{+6.02}_{-4.83}$	$1.51^{+0.27}_{-0.32}$	$2.9^{+1.5}_{-1.0}$	$10.23^{+6.59}_{-5.18}$
CL 0809+2811	$1.75^{+0.23}_{-0.28}$	$1.1^{+1.9}_{-0.8}$	$9.84^{+4.41}_{-4.01}$	$1.69^{+0.18}_{-0.21}$	$3.9^{+2.0}_{-1.3}$	$8.87^{+3.15}_{-2.93}$	$1.71^{+0.19}_{-0.22}$	$3.4^{+1.7}_{-1.2}$	$9.24^{+3.46}_{-3.14}$
CL 1357+6232	$1.11^{+0.21}_{-0.25}$	$1.8^{+3.3}_{-1.2}$	$2.92^{+1.99}_{-1.56}$	$1.02^{+0.18}_{-0.23}$	$4.2^{+2.2}_{-1.4}$	$2.26^{+1.46}_{-1.20}$	$1.06^{+0.20}_{-0.24}$	$3.6^{+1.8}_{-1.2}$	$2.52^{+1.74}_{-1.34}$
CL 1416+4446	$0.98^{+0.15}_{-0.18}$	$5.5^{+13.9}_{-3.3}$	$1.73^{+0.92}_{-0.79}$	$0.97^{+0.14}_{-0.17}$	$4.8^{+2.5}_{-1.6}$	$1.69^{+0.83}_{-0.74}$	$0.98^{+0.16}_{-0.18}$	$3.9^{+2.0}_{-1.3}$	$1.71^{+0.95}_{-0.79}$
CL 1641+4001	$1.06^{+0.30}_{-0.26}$	$0.1^{+0.3}_{-0.1}$	$2.34^{+2.61}_{-1.34}$	$0.86^{+0.22}_{-0.36}$	$4.8^{+2.5}_{-1.6}$	$1.27^{+1.26}_{-1.02}$	$1.01^{+0.21}_{-0.28}$	$3.7^{+1.9}_{-1.3}$	$2.05^{+1.51}_{-1.26}$
CL 1701+6414 <sup>†</sup>	$0.94^{+0.32}_{-0.29}$	$0.1^{+1.1}_{-0.1}$	$1.62^{+2.28}_{-1.08}$	$0.95^{+0.16}_{-0.19}$	$4.6^{+2.4}_{-1.6}$	$1.69^{+1.02}_{-0.83}$	$1.01^{+0.17}_{-0.20}$	$3.8^{+1.9}_{-1.3}$	$2.03^{+1.17}_{-0.98}$

**Notes.** Columns (1) to (3) give  $r_{200}$  and  $c_{\text{NFW}}$  from the default cluster models, and the corresponding mass,  $M_{200}^{\text{wl}}(r_{200})$ . Fixing the concentration to the value  $c_{\text{B01}}$  expected from the [Bullock et al. \(2001\)](#) mass-concentration relation, we obtain the best-fit radius  $r_{200, \text{B01}}$  and mass  $M_{200, \text{B01}}^{\text{wl}}(r_{200, \text{B01}})$ , in Cols. (4) to (6). Columns (7) to (9) contain the respective quantities calculated assuming the [Bhattacharya et al. \(2011\)](#) mass-concentration relation. <sup>†</sup> Fixing the radius and concentration of A 2246 to  $r_{s, 200} = 0.90$  Mpc and  $c_{\text{NFW}} = 20$  and hence using  $\Delta\chi^2 = 1$  for the  $1\sigma$  error margins.

$M_{200, \text{B01}}^{\text{wl}}(r_{200, \text{B01}})$ , found from the minimum of  $\sum_j p_c(r_{200}, c_{200, j}) \Delta\chi^2(r_{200}, c_{200, j})$  are listed in Table 4.

We notice that the simulations from which the B01 relation was measured assume  $\sigma_8 = 1.0$  to fix the normalisation of the matter power spectrum. This value is inconsistent with more recent measurements of cosmological parameters (e.g. [Larson et al. 2011](#); [Burenin & Vikhlinin 2012](#)). Hence, we consider a second mass-concentration relation, based on a recent suite of simulations employing  $\sigma_8 = 0.8$  as favoured by currents models: [Bhattacharya et al. \(2011, B12\)](#) study dark matter haloes of massive clusters and find that the concentration parameter can be modelled with a single power law when expressed in terms of the peak height parameter  $\nu$  from linear collapse theory<sup>5</sup>. Their simulated clusters are best represented by:

$$c_{200, \text{B12}}(\nu) = D(z)^{0.5} \times 5.9\nu^{-0.35}, \quad (5)$$

with a variance of  $\sigma_c = 0.33c_{200}$ . We compute the growth factor  $D(z)$  for a flat Universe with a cosmological constant. In complete analogy to the B01 relation, we compute cluster radii  $r_{200, \text{B12}}$  and masses  $M_{200, \text{B12}}^{\text{wl}}(r_{200, \text{B12}})$  for each cluster, given the  $c_{200}$ - $M_{200}$ -relation resulting from Eq. (5). The results are presented in Table 4.

## 4. Special cases

### 4.1. CL 1701+6414

#### 4.1.1. X-ray clusters and shear peaks

A weak lensing analysis of CL 1701+6414 has to deal with shear by multiple structures. The strongest shear peak ( $S = 4.3\sigma$ ) in Fig. 3 coincides with the most prominent cluster in the field amongst optical galaxies<sup>6</sup>, Abell 2246 (big four-pointed star symbol in Fig. 3), 4/2 to the west of CL 1701+6414. With a redshift of  $z = 0.225$  ([Vikhlinin et al. 1998](#); [Burenin et al. 2007](#)), A 2246 is part of the 400d parent sample, but not of the distant cosmological sample. CL 1701+6414, for whose detection in the  $S$ -statistics the lensing catalogue was optimised, is detected at the  $3.7\sigma$  level. The ROSAT catalogue of [Vikhlinin et al. \(1998\)](#)

<sup>5</sup> We use the fitting formula for  $\nu(M, z)$  from Table 2 of [Bhattacharya et al. \(2011\)](#).

<sup>6</sup> Due to the high concentration of galaxies, the region is masked.

lists two further clusters in the field, VMF 191 at  $z = 0.220$  and VMF 192 at  $z = 0.224$  (small star symbols in Fig. 3), which we identify with  $S$ -peaks of  $2.9\sigma$  and  $2.7\sigma$ , respectively. Another  $3.1\sigma$  peak lies close-by. A zone of positive shear signal extends over  $>20'$ , from the north-east of VMF 192 to a  $3.6\sigma$  shear peak south-west of A 2246, which does not correspond to a known cluster. Noticing the very similar redshifts of A 2246, VMF 191, and VMF 192, we likely are observing a physical filament at  $z = 0.22$ , through whose centre we see CL 1701+6414 in projection. Luckily, a likely strong lensing arc,  $10''$  to the west of the BCG of CL 1701+6414 ( $z = 0.44 \pm 0.01$ , [Reimers et al. 1997](#)) gives direct evidence that CL 1701+6414 acts as a gravitational lens. We find no significant WL signal near the ROSAT source RX J1702+6407 ([Donahue et al. 2002](#), cf. Appendix D.6).

#### 4.1.2. Two-cluster modelling of MMT data

Plotting the binned tangential shear around the lensing centre (lower left panel of Fig. 3), we find a flat profile whose average  $\langle \varepsilon_t(\theta) \rangle > 0$  is consistent with the extended shear signal in the  $S$ -map. The cross-component  $\langle \varepsilon_x(\theta) \rangle$  is consistent with zero. Acknowledging the prominent signal related to A 2246, we model the shear of CL 1701+6414 and A 2246, simultaneously, using an NFW shear profile for each deflector.

We assume both the shear  $g_p$  of the primary and  $g_s$  of the secondary component to be small. In this limit, the shear components originating from both lenses become additive:

$$g_{\text{add}, \alpha}(\boldsymbol{\theta}) = g_{p, \alpha}(\boldsymbol{\theta}; r_{p, 200}, c_{p, \text{NFW}}) + g_{s, \alpha}(\boldsymbol{\theta}; r_{s, 200}, c_{s, \text{NFW}}), \quad (6)$$

with  $\alpha = 1, 2$ . Here,  $r_{p, 200}$ ,  $r_{s, 200}$ ,  $c_{p, \text{NFW}}$ , and  $c_{s, \text{NFW}}$  are the radii and concentration parameters of the primary and secondary component. Note that  $g_{\text{add}, \alpha}(\boldsymbol{\theta})$  explicitly depends on the two-dimensional coordinate vector  $\boldsymbol{\theta}$ : the shear field of two clusters no longer has radial, but only axial symmetry. This is illustrated in the lower right panel of Fig. 3, showing the shear fit expected from the best-fit two-cluster model for the CL 1701+6414 lensing catalogue, evaluated on a regular grid. We consider a modification of the merit function given by Eq. (3):

$$\chi_4^2 = \sum_{i=1}^{N_{\text{gal}}} \frac{|g_{\text{add}, i}(r_{p, 200}, c_{p, \text{NFW}}, r_{s, 200}, c_{s, \text{NFW}}) - \varepsilon_i|^2}{\sigma_{\text{fit}}^2 \left(1 - |g_{\text{add}, i}(r_{p, 200}, c_{p, \text{NFW}}, r_{s, 200}, c_{s, \text{NFW}})|^2\right)^2}. \quad (7)$$

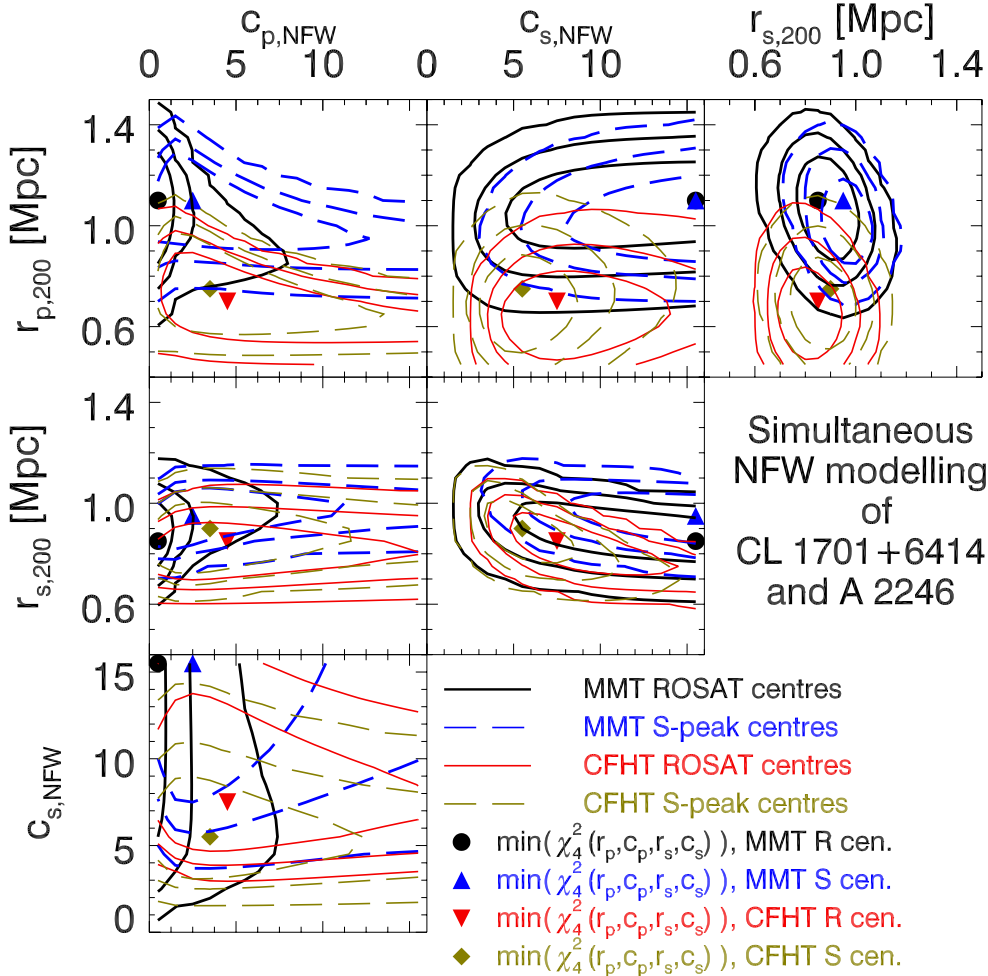


**Fig. 4.** Simultaneous NFW modelling of CL 1701+6414 and A 2246. Each panel shows the dependencies between two of the four parameters, with the other two marginalised. Solid confidence contours ( $1\sigma$ ,  $2\sigma$ ,  $3\sigma$ ) denote the default case, using the ROSAT centres; dashed contours denote models centred on the  $S$ -peaks. The respective parameters minimising  $\chi_4^2$  are indicated by a filled circle and an upward triangle. Sets of thin contours denote the confidence contours and parameters minimising  $\chi_4^2$  obtained from the analogous analysis of the CFHT lensing catalogue. The best-fit values for the CFHT data are marked by downward- and upward-pointing triangles for the ROSAT and  $S$ -peak centres, respectively.

The symbol  $\chi_4^2$  highlights the dependence on four parameters, the radii and concentrations of the two clusters. Note that  $\chi_4^2$  models the measured  $\varepsilon_i$  directly, without recourse to a definition of the tangential component.

We assumed  $\langle\langle\beta\rangle\rangle = 0.381$  for CL 1701+6414 (Table 3) and  $\langle\langle\beta\rangle\rangle = 0.640$  for A 2246, calculated the same way as for the other clusters. The average tangential and cross-component of the shear expected in concentric annuli around the centre of CL 1701+6414 are presented in the lower left panel of Fig. 3. A vertical dotted line denotes the separation of CL 1701+6414 and A 2246. We find a good agreement to the measured shear and note that due to the lack of radial symmetry the dispersion of the model values in the annuli is of the same order as the measurement errors. Although the cross-component can be large at some points in the image plane,  $\langle g_x \rangle$  cancels out nearly completely when averaging over the annuli.

Figure 4 presents the confidence contours and parameters minimising Eq. (7) for the default model (filled circle and solid contours). The panels of Fig. 4 show all combinations of two fit parameters, where we marginalised over the two remaining ones. Owing to the 4-dimensional parameter space, we tested a coarse grid of points to avoid excessive computing time. The picture emerges that  $r_{p,200}$  and  $r_{s,200}$  are relatively independent of each other (top right panel). Hence, the presence of the respective other cluster does not seem to affect the accuracy with which we can determine the masses of the two clusters strongly. The data favour the smallest tested value,  $c_{p,NFW} = 0.5$  for the concentration of CL 1701+6414, and the largest one,  $c_{s,NFW} = 15.5$ , for

A 2246. Using shear peak cluster centres (dashed contours and upward pointing triangle in Fig. 4),  $c_{p,NFW}$  is also very low, but the uncertainties are large. The poor constraint on  $c_{s,NFW}$  might be partly due to the masking of the centre of A 2246 or shear contribution by the BCG.

Given the absence of a strong covariance between the parameters of A 2264 and CL 1701+6414, we fix the parameters of the foreground cluster to  $r_{s,200} = 0.90$  Mpc and  $c_{s,NFW} = 20$  and repeat the analysis with our usual, finer parameter grid. The best model is found for  $r_{p,200}^{\min} = 0.94^{+0.32}_{-0.29}$  Mpc  $c_{p,NFW}^{\min} = 0.1^{+1.1}_{-0.1}$ , confirming the results from Fig. 4. We note that we find a low  $c_{p,NFW}$ , although our model explicitly accounts for the extra shear by A 2246. Using the default model, we compute masses of  $1.6^{+2.3}_{-1.1} \times 10^{14} M_\odot$  for CL 1701+6414 and  $1.1^{+0.4}_{-0.3} \times 10^{14} M_\odot$  for A 2246, based on  $r_{s,200}^{\min} = 0.9 \pm 0.1$  Mpc.

#### 4.1.3. Comparison to CFHT data

In addition, Fig. 4 shows confidence contours obtained from a WL analysis of CFHT observations of the CL 1701+6414 field ( $r'$ -band,  $\approx 7200$  s), which we discuss in greater detail in Sect. 5. We repeated the two-cluster modelling using Eq. (7) following the same data reduction and shear measurement pipelines. Besides  $m_{\text{faint}} = 20.2$  and the PSF-dependent galaxy selection, parameters are kept at their MMT values.

The resulting cluster parameters minimising  $\chi_4^2$  (red downward triangles for ROSAT and diamonds for  $S$ -peak centres)

and the corresponding thin confidence contours in Fig. 4 show agreement with the MMT data within the  $2\sigma$  margins or better. With  $r_{p,200}^{\min} = 0.70 \pm 0.20$  Mpc, and  $r_{s,200}^{\min} = 0.85^{+0.15}_{-0.10}$  Mpc, relating to WL masses of  $M_{200}^{\text{CFHT}} = 0.7^{+0.7}_{-0.4} \times 10^{14} M_{\odot}$  for CL 1701+6414 and  $M_{200}^{\text{CFHT}} = 0.9 \pm 0.4 \times 10^{14} M_{\odot}$  for A 2246, we arrive at lower masses, especially for CL 1701+6414, but consistently within the uncertainties of the MMT data. Using the  $S$ -peaks as centres yields very similar results.

Our CFHT data give more plausible best-fit concentration parameters of  $c_{s,\text{NFW}}^{\min} = 7.5^{+8}_{-3.0}$  for A 2246, and  $c_{p,\text{NFW}}^{\min} = 4.5^{+11}_{-4.5}$  for CL 1701+6414, although the constraints are poor. We conclude that a dual-NFW modelling is feasible, but more sensitive to the choice of cluster centres than a single NFW fit to  $r_{200}$  and  $c_{\text{NFW}}$ . Adding more cluster components would even increase these interdependencies. However, the main point here is that the MMT and CFHT analyses agree.

#### 4.2. CL 1641+4001

The  $S$ -statistics map of CL 1641+4001 exhibits several shear peaks which form a connected structure of  $>20'$  extent (Fig. 5). Located within a plateau of  $S > 3\sigma$  significance, the ROSAT centre of CL 1641+4001 (big star symbol) is separated by  $95''$  from the primary ( $S = 4.12$ ) shear peak and by  $125''$  from the secondary ( $S = 3.95$ , orange triangle in Fig. 5) shear peak. The BCG of CL 1641+4001 can be found between the ROSAT centre and primary shear peak.

The  $\langle \varepsilon_t(\theta) \rangle$  profile (lower left panel of Fig. 5) centred on the main shear peak profile is flat, with a positive average in all bins and the most significant positive signal at  $\sim 9'$  distance from the cluster centre. In the innermost two bins ( $\theta < 3'33$ ),  $\langle \varepsilon_x(\theta) \rangle$  is of similar amplitude as the tangential component, but consistent with zero at the  $1\sigma$  level. Similar to CL 1701+6414, the modelling using Eq. (3) finds a very low  $c_{\text{NFW}} = 0.1^{+0.3}_{-0.1}$ , consistent with zero and reflecting the flat shear profile.

The only cluster candidate in the literature besides CL 1641+4001 is SDSS-C4-DR3 3628 at  $z = 0.032$ , identified in the SDSS Data Release 3, using the Miller et al. (2005) algorithm, but published solely by von der Linden et al. (2007). We test a two-cluster model, introducing a second component at the redshift of SDSS-C4-DR3 3628, implying  $\langle \beta \rangle = 0.940$ . We choose the second-highest shear peak as the centre of the secondary component. The offset of  $\sim 3'$  to the coordinates of SDSS-C4-DR3 3628 (small star symbol in Fig. 5) is justified by the large mask at the latter position. The two-cluster fit yields a mass of order  $10^{14} M_{\odot}$  for both the primary and the secondary component. This estimate is in stark disagreement with the absence of a massive, nearby cluster from our MMT image, which would have had to be missed by all but one cluster surveys.

At the same coordinates as SDSS-C4-DR3 3628 and also at  $z = 0.032$ , NED lists CGCG 224–092, a galaxy pair, dominated by the bright elliptical UGC 10512. These two galaxies are what we see in the MegaCam image<sup>7</sup> and also in the SDSS image of the area. Inspection of the respective CHANDRA image shows significant X-ray emission, whose extent of  $\sim 30''$  in diameter ( $\sim 20$  kpc at  $z = 0.032$ ) is consistent with being caused by a massive elliptical galaxy or small galaxy group. With  $\approx 1.7 \times 10^{41}$  erg  $s^{-1}$  in the 2–10 keV range, its flux is high for a single galaxy, but the low temperature of  $\approx 0.6$  keV (obtained by fitting an absorbed APEC model) speaks against a galaxy group. In conclusion, we deem it unlikely that the complex

**Table 5.** Observation dates, final exposure times and seeing values in the coadded CFHT/MegaCam data for CL 1701+6414.

Filter	Observation dates	$T_{\text{exp}}$	Seeing
$g'$	2006-03-07	1601 s	0''.94
$r'$	2006-05-29	7179 s	0''.66
$i'$	2006-04-26	1922 s	0''.84
$z'$	2006-04-22, 2006-04-26	1801 s	0''.82

structure in the  $S$ -map of CL 1641+4001 bears a significant contribution from the  $z = 0.032$  structure.

We prefer the hypothesis that the shear is caused by a complex structure at the redshift of CL 1641+4001, although its X-ray morphology does not hint at a merger (Vikhlinin et al. 2009a). Despite its shortcomings, we return to the simplest explanation for the time being and model CL 1641+4001 by a single NFW component: we obtain a minimum of  $\chi^2$  for  $r_{200}^{\min} = 1.06^{+0.30}_{-0.26}$  Mpc and  $c_{\text{NFW}}^{\min} = 0.1^{+0.3}_{-0.1}$ . These results, entailing a mass estimate of  $2.3^{+2.6}_{-1.3} \times 10^{14} M_{\odot}$  are illustrated by the filled circle and solid contours in the lower right panel of Fig. 5. Interestingly, choosing the secondary shear peak as a centre yields similar cluster parameters to those found by choosing the primary shear peak. This could hint at a major merger of similarly massive substructures, but more observations are needed to test this hypothesis.

## 5. Verification with independent data

### 5.1. CFHT observations

CL 1701+6414 is the only cluster we observed with MMT/MegaCam for which deep, lensing-quality data obtained with another telescope exist. It has been observed in the  $g'r'i'z'$  filters (P.I.: G. Soucail, Run ID: 2006AF26) using the MegaPrime/MegaCam at the Canada-France-Hawaii Telescope (CFHT)<sup>8</sup>. Table 5 lists the specifications of the CFHT data set. The CFHT data are processed with THELI in the same way as the MMT data, with a few CFHT-specific modifications to the code (cf. Erben et al. 2009), making use of the pre-processing available for archival CFHT data. Hence, the results are a suite of coadded and calibrated images in the  $g'r'i'z'$  passbands, centred on CL 1701+6414, and with a side length of  $\sim 1^\circ$  each. From the  $g'r'i'$  images, we derived the pseudo-colour images of the centres of CL 1701+6414 and A 2246 in Fig. 1.

We employ the CFHT data for two kinds of consistency checks with the MMT data: First, we run the lensing pipeline on the deep CFHT  $r'$  band image, applying the same shape recovery technique to the same objects, but observed with different instruments. The results of this comparison are detailed in Sect. 5.2. Second, making use of the CFHT imaging in four bands, we produced a BPZ (Benítez 2000) photometric redshift catalogue (Sect. 5.4 and Appendix C) with the goal of testing the single-band (magnitude cut) background selection in the CL 1701+6414 MMT lensing catalogue.

### 5.2. Comparative shape analysis

In this Subsection, we compare shape measurements obtained in the same field (the one of CL 1701+6414) using the MMT/MegaCam and CFHT/MegaCam instruments

<sup>8</sup> For the sake of clarity, we use “MMT” and “CFHT” to distinguish the data sets.

<sup>7</sup> Strongly overexposed and therefore masked.

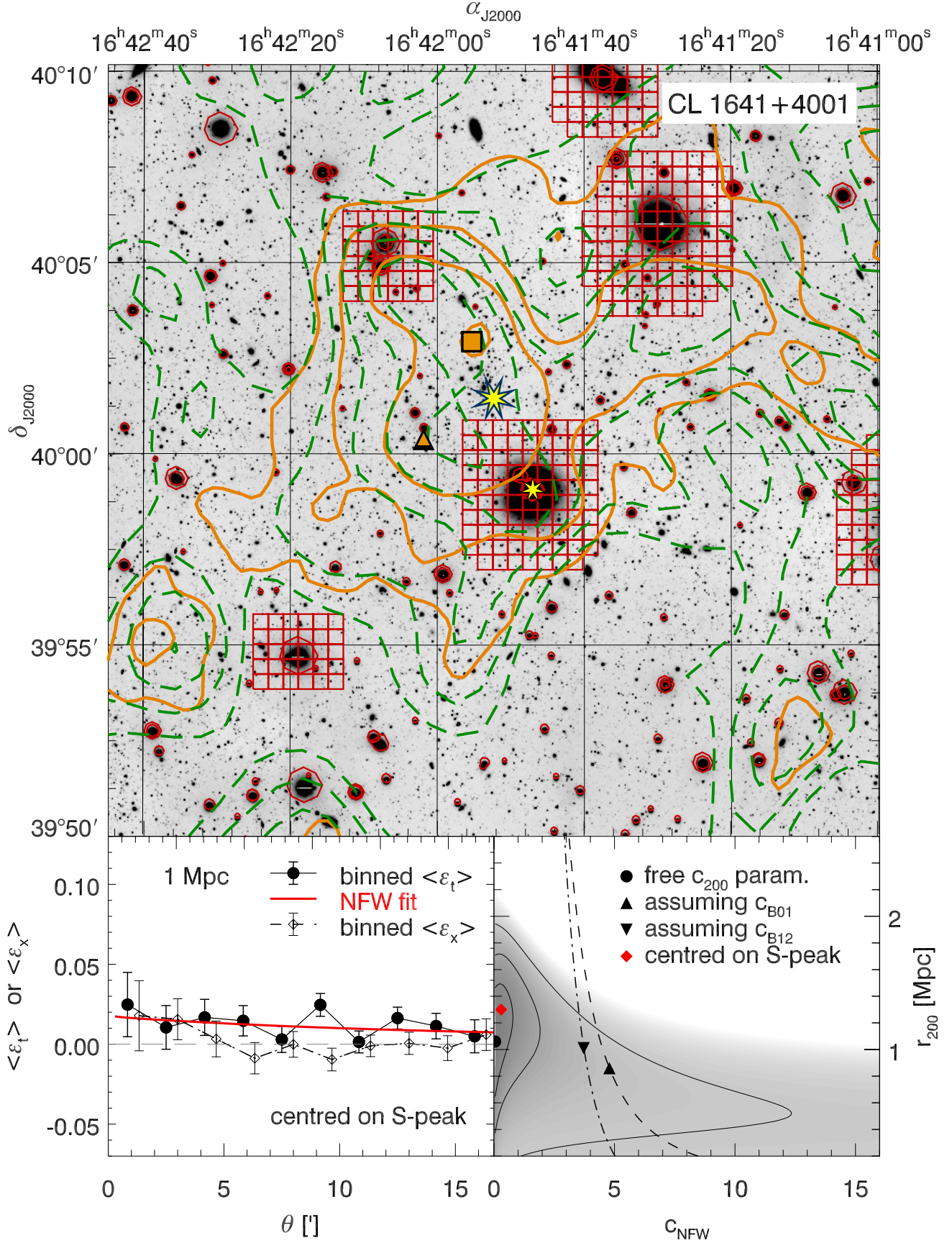


**Fig. 5.** Same as Fig. 2, but for CL 1641+4001. In the map, a triangle denotes the secondary shear peak, while a small star symbol marks the position of the von der Linden et al. (2007) cluster candidate. Note that no peak in the complex pattern of shear peaks correlates with its position.

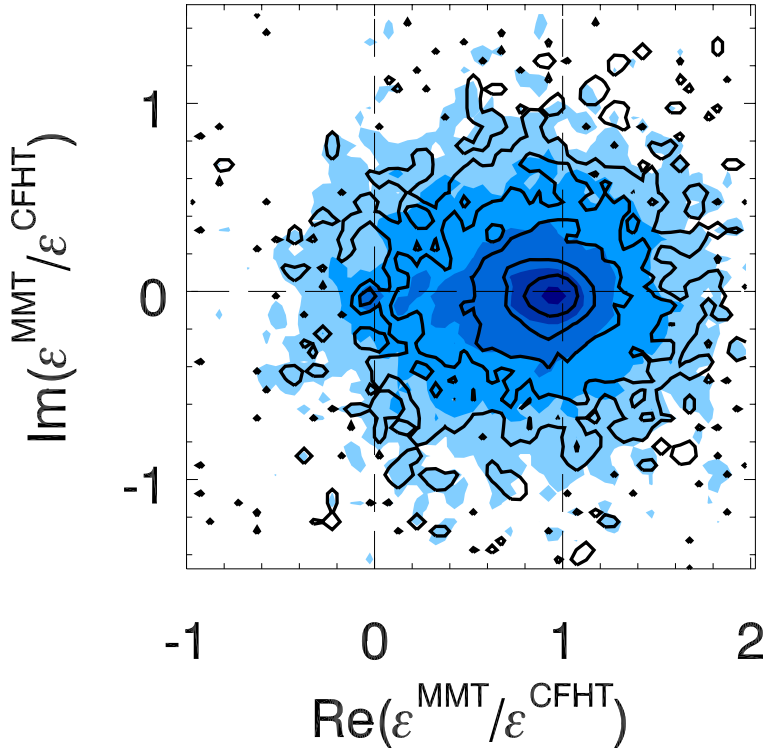


**Fig. 6.** Sample density of the ratio  $\epsilon^{\text{MMT}}/\epsilon^{\text{CFHT}}$  of the complex ellipticities measured for the matched galaxies from the MMT and CFHT  $r'$ -band catalogues, respectively. The shaded contours correspond to the logarithmic densities of all galaxies from the MMT lensing catalogue which have a match in the CFHT catalogue. Solid contours give the density of galaxies detected with a signal/noise ratio of  $\nu > 15$ , the top 32.6%. Note that the normalisation of the  $\nu > 15$  galaxies is scaled up by  $1/0.326$  to obtain the same logarithmic contour levels. A Gaussian smoothing kernel of full-width half-maximum 0.075 was applied to both contour maps.

(cf. Sect. 5.1). Using the same parameter settings for our KSB pipeline, we extracted a KSB catalogue from the CFHT  $r'$ -band image. Subsequently, the CFHT and MMT catalogues were matched, using the `associate` and `make_ssc` tools available in THELI. With the smaller field-of-view of MMT/MegaCam defining the location of possible matches, 68.2% of sources in the MMT KSB catalogue are matched to a CFHT detection. Larger masked areas in the CFHT image – in particular due to reflections (so-called ghosts) around very bright stars – are the main cause impeding a higher matching fraction. Inside the MMT area (measuring at a safe distance from its low-weight edges), we find 85.5% of the CFHT sources to be detected by MMT.

We note that objects in the matched catalogue have comparable SExtractor signal-to-noise ratios  $\nu$  in both  $r'$ -band images. Considering objects with  $\nu_{\text{MMT}} > 15$  – the top quartile of all objects in the catalogue of matches – for which selection effects should be negligible, we measure  $\langle \nu_{\text{CFHT}}/\nu_{\text{MMT}} \rangle = 0.832$ , with a dispersion of 0.057. These values show little dependence on the limiting value of  $\nu_{\text{MMT}}$ , and confirm the visual impression that the  $r'$ -band images are of similar depth<sup>9</sup>.

With these preparatory analyses in mind, we investigate the relation between the ellipticities observed with CFHT and MMT. Figure 6 presents the ratio  $\epsilon^{\text{MMT}}/\epsilon^{\text{CFHT}}$  of the complex ellipticities measured by KSB on the MMT and CFHT images<sup>10</sup>. Shaded contours in Fig. 6 mark lines of equal density of the distribution of  $\epsilon^{\text{MMT}}/\epsilon^{\text{CFHT}}$ , as measured from the sources passing the criteria for the MMT galaxy catalogue (cf. Sect. 2.4). Using a grid of mesh size as small as 0.01 for both the real and imaginary axes, we find the density distribution of  $\epsilon^{\text{MMT}}/\epsilon^{\text{CFHT}}$  to scatter around its peak at unity. Note that the logarithmic scaling in

Fig. 6 emphasises the wings of the distribution. When repeating the analysis restricted to galaxies detected with  $\nu_{\text{MMT}} > 15$  – the top 32.6% of the matched sources contained in the MMT galaxy catalogue – the peak at  $\epsilon^{\text{MMT}} = \epsilon^{\text{CFHT}}$  persists, while the scatter is slightly reduced (solid contours in Fig. 6). This can be seen comparing the two outermost solid contours to the shaded contours, indicating the same levels of number density.

This means, any systematic bias between shear measurements obtained with MMT and CFHT is smaller than a few percent. We expect a small bias, below the sensitivity of our measurement, to be present because of the dependence of the shear calibration factor  $f_0$  on magnitude and half-light radius  $\vartheta$  (cf. Appendix C of Hartlap et al. 2009). In addition to our results from Paper I, the consistent galaxy ellipticities measured with MMT and the well-established CFHT/MegaCam mark further evidence that MMT/MegaCam is well-suited for measuring weak gravitational lensing signals.

### 5.3. S-statistics from CFHT and MMT

Figure 7 provides a qualitative comparison of the  $S$ -maps for CL 1701+6414 obtained with both CFHT and MMT. Its upper two panels show the independent shear catalogues drawn from the  $r'$  images of both instruments, at the respective optimal values  $m_{\text{faint}}^{\text{MMT}} = 21.9$  and  $m_{\text{faint}}^{\text{CFHT}} = 20.2$  for  $\theta_{\text{out}} = 14.5$ . The distribution of the  $S$ -signal in the overlapping region inside the MMT field-of-view (black square in Fig. 7) is astonishingly similar: not only do we find the tentative filament from the north-east of VMF 192 to the south-west of A 2246 (compare Fig. 3 and the black lines in Fig. 7 indicating the  $\alpha_{J2000}$  and  $\delta_{J2000}$  of CL 1701+6414). Moreover, also the regions of high  $S$  at the eastern and north-western edges of the MMT field-of-view correspond to peaks in the CFHT  $S$ -map. Whereas the detection significance at the peak closest to the position of CL 1701+6414 is smaller for CFHT ( $S = 2.89$  compared to  $S = 3.75$ ), it is also more prominent in the sense of a deeper “valley” separating it

<sup>9</sup> While the good  $T_{\text{exp}}$  is similar for both data sets, the larger mirror area of MMT is probably offset by the better seeing in the CFHT image.

<sup>10</sup> As the complex ellipticity is the relevant observable, we prefer considering the components of the ratio  $\epsilon^{\text{MMT}}/\epsilon^{\text{CFHT}}$  over the ratios for the individual components as measured with the two instruments.

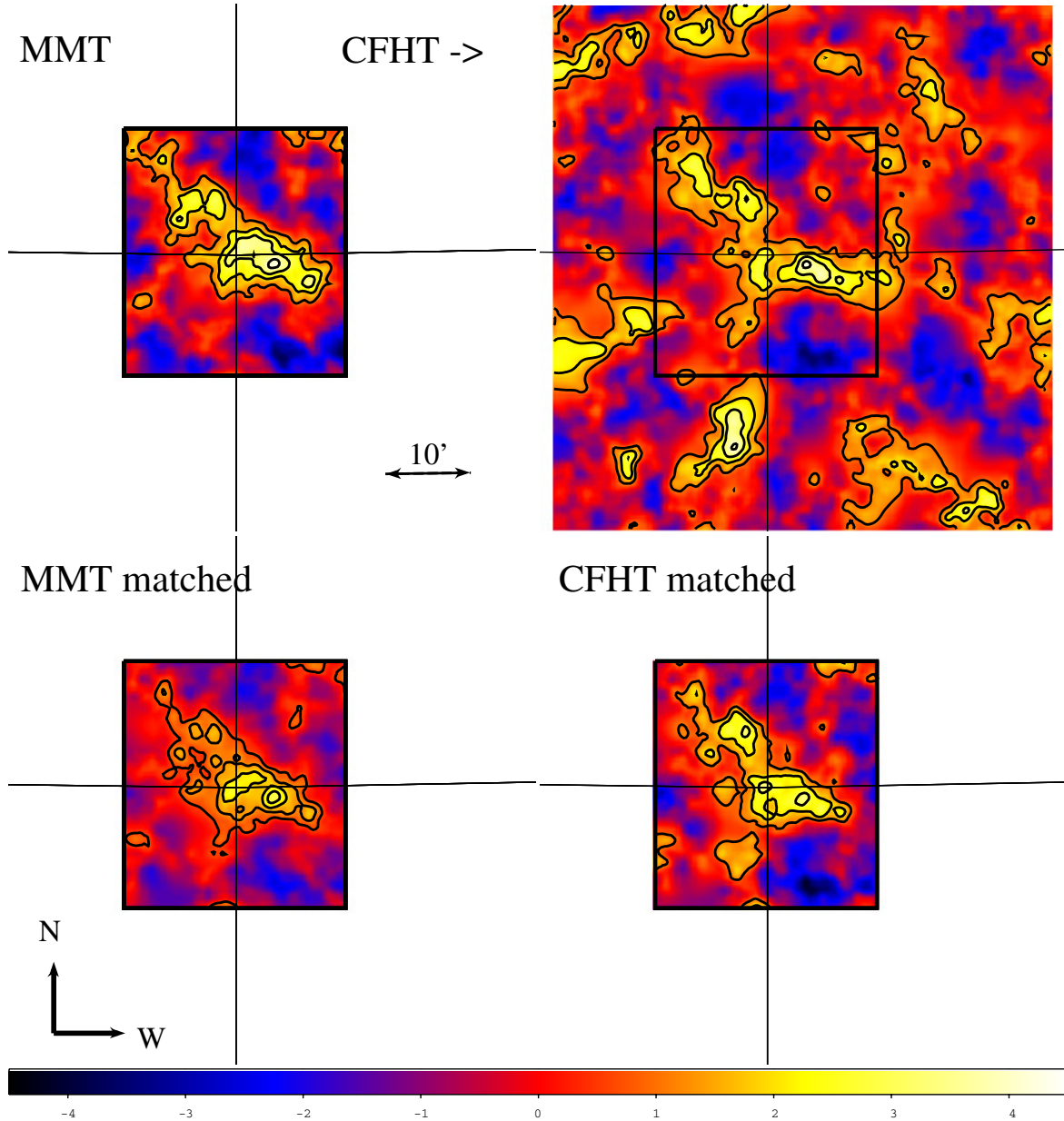


**Fig. 7.**  $S$ -statistics in the CL 1701+6414 field drawn from the MMT (*top left*), CFHT (*top right*), and matched sources catalogues (*bottom panels*). The linear colour scale, contours indicating levels of  $S = 1$  to  $S = 4$ ,  $\theta_{\text{out}} = 14'.5$ , and cross-hairs at the position of CL 1701+6414 are the same in all panels. Thick black squares outline the MMT field-of-view.

from the dominant A 2246 peak ( $S = 4.30$  in both the MMT and CFHT maps).

The second-most significant ( $4.08\sigma$ ) shear peak in the CFHT  $S$ -map is at  $\alpha_{J2000} = 17^{\text{h}}01^{\text{m}}57^{\text{s}}$ ,  $\delta_{J2000} = +63^{\circ}51'$ , outside the southern edge of the MMT field-of-view, with no known cluster but several brighter ( $r' < 20$ ) galaxies in the vicinity.

Can the subtle differences between the MMT and CFHT  $S$ -maps be attributed to shape noise or rather to selection of galaxies at the faint end? We investigate that by considering the matched-sources catalogue from Sect. 5.2 and apply to it the combined selection criteria for the MMT and CFHT lensing catalogues (e.g. both  $|e^{\text{MMT}}| < 0.8$  and  $|e^{\text{CFHT}}| < 0.8$ ). The resulting  $S$ -maps derived from the MMT and CFHT ellipticities of the exact same sources are displayed in the lower left and lower right panels of Fig. 7. Naturally, all matched sources are located within the MMT field-of-view. Qualitatively, the matched  $S$ -maps again show the same structure, although they do not

appear to be much more similar than the  $S$ -maps drawn from the individual catalogues. This indicates that galaxy selection plays a relevant role. We note that based on the CFHT shapes of the matched galaxies, CL 1701+6414 is the most significant detection with  $S = 3.46$ , while the A 2246 peak is suppressed by  $\approx 1\sigma$  compared to the pure CFHT map.

Quantitatively, the Pearson correlation coefficient of  $\varrho = 0.912$  between the matched-sources  $S$  maps substantiates the visual impression of a high correlation. When the faintest  $\approx 20\%$  of galaxies are removed from the matched catalogue, considering only galaxies brighter than  $r'_{\text{cut}} = 24.85$  in both the MMT and CFHT images, this value increases to  $\varrho = 0.926$ . Removing the faintest  $\approx 40\%$  of galaxies by imposing  $r'_{\text{cut}} = 24.45$ , it further rises to  $\varrho = 0.938$ .

The detection of the same shear peaks reassures us that the multi-peaked  $S$ -distribution analysed in detail in Sect. 4.1 traces an actual shear signal and removes any doubts that

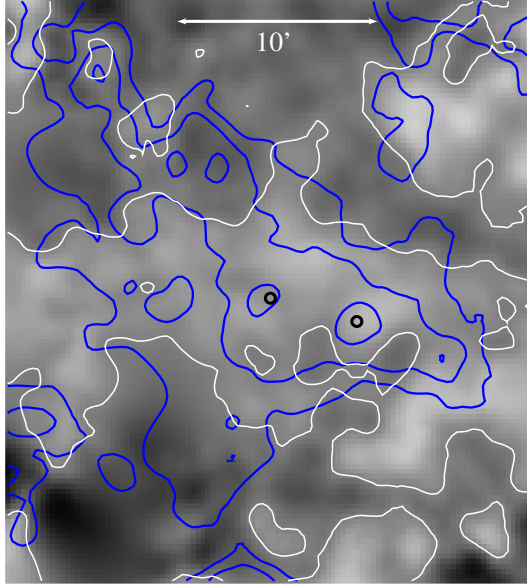


**Fig. 8.** Average and difference aperture mass  $\mathcal{M}^\pm$  (Eq. (8)), measured in the matched MMT-CFHT catalogue. The grey-scale and white contours give  $\mathcal{M}^-$ , the thicker blue contours show  $\mathcal{M}^+$ . The spacing for both contours is in multiples of 0.015, starting at 0. Black circles mark the positions of CL 1701+6414 and A 2246.

the  $S$ -filament across the MMT field-of-view could be merely an instrument-dependent artefact, e.g. residuals of improper PSF anisotropy correction.

As a final test to the hypothesis that we see the same shear signal measured in the ellipticities from both instruments, we consider the average and difference aperture mass of the matched sources:

$$\mathcal{M}^\pm = \pi \theta_{\text{out}}^2 N(\theta_c)^{-1} \sum_j \varepsilon_{t,j}^\pm Q_j (|\theta_j - \theta_c| / \theta_{\text{out}}) \quad (8)$$

with  $\varepsilon_{t,j}^\pm$  the tangential component of

$$\varepsilon_j^\pm = (\varepsilon_j^{\text{MMT}} \pm \varepsilon_j^{\text{CFHT}}) / 2 \quad (9)$$

and the index  $j$  running over all  $N(\theta_c)$  galaxies within a distance  $\theta_{\text{out}}$  from  $\theta_c$ . The outcome of this experiment is shown in Fig. 8: While  $\mathcal{M}^+$  (blue contours) retrieves the signal of both clusters (black circles), exhibiting the expected great similarity to the matched-sources  $S$ -maps in Fig. 7,  $\mathcal{M}^-$  (grey-scale and white contours in Fig. 8) has a much smaller amplitude. Its pattern is not obviously related to the one seen in  $\mathcal{M}^+$ : Although the main clusters reside in a region of enhanced  $\mathcal{M}^-$ , they do not correspond to peaks in  $\mathcal{M}^-$ . The absence of the  $\mathcal{M}^+$ -peaks in  $\mathcal{M}^-$  is consistent with the absence of a noticeable shear calibration bias between MMT and CFHT (cf. Sect. 5.2). A possible explanation for the stripe-like pattern in  $\mathcal{M}^-$  are differences in the spatially varying anisotropy correction. We conclude these effects to be small and no impediment to direct comparisons of MMT and CFHT WL measurements, which we conclude to be consistent.

The SW peak. A peculiar feature in the MMT  $S$ -map of CL 1701+6414 is the  $3.6\sigma$  shear peak at  $\alpha_{J2000} = 17^{\text{h}}00^{\text{m}}05^{\text{s}}$ ,  $\delta_{J2000} = +64^{\circ}11'00''$ , south-west of A 2246 (cf. Fig. 3). This peak does not correspond to an evident overdensity of galaxies in the MMT and CFHT  $r'$ -band images, nor to an extended emission in the *Chandra* X-ray images. The pure CFHT  $S$ -map

does not show a counterpart to the SW peak detected with MMT, although the  $S$ -contours of A 2246 are extended towards its direction. Interestingly, in the matched-sources  $S$ -maps, we detect a  $2.8\sigma$  peak from the MMT ellipticities and a  $2.4\sigma$  peak from the CFHT ellipticities. We checked that the SW peak in the MMT  $S$ -map does not arise from a chance alignment of a few galaxies with extraordinary high  $\varepsilon_t$  resulting from stochastic shape noise. Considering the observations in the CFHT and matched-catalogue  $S$ -maps, it seems likelier that we observe a true “shear peak” arising from the superposed light deflections of line-of-sight structure in the complex and dense environment of the CL 1701+6414/A 2246 field.

#### 5.4. Photometric redshift results

Using photo-zs based on the available  $g'r'i'z'$  observations (Table 5) is challenging because of the small spectral coverage and shallowness of the data. Nevertheless, a comparison with sources for which SDSS spectroscopic redshifts are known, revealed a coarse redshift sorting to be possible, with typical errors of  $\sigma(z_{\text{ph}}) \approx 0.25$  for the relevant  $z \lesssim 0.5$  redshift range (Appendix C.1). Matching the photo- $z$  catalogue with the CL 1701+6414 MMT data set, we can identify most sources in the galaxy catalogue with a photo- $z$  galaxy, albeit with low quality for most sources (Appendix C.2).

Drawing the  $S$ -statistics from this catalogue, whereby galaxies are sorted based on their CFHT photo-zs, we retrieve shear peaks similar to Fig. 3 for the background catalogue, while CL 1701+6414 does not show up as a shear peak in the foreground catalogue (Appendix C.3). From this, we draw two conclusions: First, we likely see an indication of shear emanating from more than one lens plane, namely CL 1701+6414 on the one hand and A 2246 and associated structures on the other hand. Second, owing to the poor quality of the four-band photo- $z$ , a desirable calibration of single-band shear catalogues lies beyond the grasp of this data set.

## 6. Accuracy of the mass estimates

### 6.1. Error analysis

The error analysis of the seven clusters analysed in Sect. 3 follows the method described in Paper I, i.e. we apply

$$\sigma_{\text{tot}}^2 = \sigma_{\text{stat}}^2 + \sigma_{\text{sys}}^2 = \sigma_{\text{stat}}^2 + \sigma_{\text{LSS}}^2 + \sigma_{\text{proj}}^2 + \sigma_{\text{geom}}^2 + \sigma_{\text{cali}}^2 \quad (10)$$

to calculate the total uncertainty in mass for each cluster. We will now discuss how we obtain the different terms in Eq. (10). The statistical error  $\sigma_{\text{stat}}$  is inferred from the tabulated  $\Delta\chi^2$  for the cluster on the grid in  $r_{200}$  and  $c_{\text{NFW}}$ : taking  $\Delta\chi^2 = 1$ , we find the upper and lower limits of  $r_{200}$  and then applying Eq. (2). Table 6 compares the masses of our eight clusters and their errors.

The components  $\sigma_{\text{cali}}$  and  $\sigma_{\text{geom}}$ , accounting for the uncertainties in the shear calibration factor  $f_0$  and the redshift distribution of the source galaxies are likewise determined from the analysis of the parameter grid. Assuming the redshift distribution to be well modelled by the fits to the CFHTLS Deep 1 photo- $z$  catalogue, we vary  $\langle\langle\beta\rangle\rangle$  by the uncertainties tabulated in Table 3. As expected,  $\sigma_{\text{geom}}$  increases with redshift because of the higher relative uncertainty in  $\langle\langle\beta\rangle\rangle$ .

### 6.2. Redshift distribution

Comparing the source number counts in the CFHTLS Deep 1 field with our MMT data, we find very good matches

**Table 6.** Weak lensing masses resulting from our analysis.

Cluster	$M_{\text{wl}}(r_{200,\text{wl}})$	$\sigma_{\text{stat}}^-$	$\sigma_{\text{stat}}^+$	$\sigma_{\text{sys}}^-$	$\sigma_{\text{sys}}^+$	$\sigma_{\text{tot}}^-$	$\sigma_{\text{tot}}^+$	$\frac{\sigma_{\text{stat}}^-}{M^{\text{wl}}}$	$\frac{\sigma_{\text{stat}}^+}{M^{\text{wl}}}$	$\frac{\sigma_{\text{sys}}^-}{M^{\text{wl}}}$	$\frac{\sigma_{\text{sys}}^+}{M^{\text{wl}}}$	$\frac{\sigma_{\text{tot}}^-}{M^{\text{wl}}}$	$\frac{\sigma_{\text{tot}}^+}{M^{\text{wl}}}$
CL 0030+2618	6.23	1.76	1.87	2.07	1.97	2.72	2.72	28%	30%	33%	32%	44%	44%
CL 0159+0030	4.10	2.07	2.46	1.25	1.31	2.42	2.78	50%	60%	30%	32%	59%	68%
CL 0230+1836	10.23	5.18	6.59	4.68	3.59	6.98	7.51	51%	64%	46%	35%	68%	73%
CL 0809+2811	9.24	3.14	3.46	2.59	2.62	4.07	4.34	34%	37%	28%	28%	44%	47%
CL 1357+6232	2.52	1.34	1.74	0.99	0.89	1.67	1.96	53%	69%	39%	35%	66%	78%
CL 1416+4446	1.71	0.79	0.95	0.60	0.58	1.00	1.12	46%	56%	35%	34%	58%	65%
CL 1641+4001	2.05	1.26	1.51	0.78	0.73	1.48	1.68	61%	74%	38%	36%	72%	82%
CL 1701+6414	2.03	0.98	1.17	0.78	0.70	1.25	1.37	48%	58%	38%	35%	61%	67%

**Notes.** Given are the WL masses  $M_{200,\text{B12}}^{\text{wl}}(r_{200,\text{B12}}^{\text{wl}})$ , assuming the B12 mass-concentration relation (cf. Table 4), their lower and upper statistical ( $\sigma_{\text{stat}}^-$  and  $\sigma_{\text{stat}}^+$ ), systematic ( $\sigma_{\text{sys}}^-$  and  $\sigma_{\text{sys}}^+$ ), and total error margins ( $\sigma_{\text{tot}}^-$  and  $\sigma_{\text{tot}}^+$ ). In addition, the corresponding relative errors are presented. All masses are given in units of  $10^{14} M_{\odot}$ .

**Table 7.** Components of the statistical error, assuming the B12 mass-concentration relation.

Cluster	$\sigma_{\text{cali}}^-$	$\sigma_{\text{cali}}^+$	$\sigma_{\text{geom}}^-$	$\sigma_{\text{geom}}^+$	$\sigma_{\text{proj}}^-$	$\sigma_{\text{proj}}^+$	$\sigma_{\text{LSS}}^-$	$\sigma_{\text{LSS}}^+$
CL 0030+2618	1.09 (18%)	0.26 (4%)	0.65 (10%)	0.73 (12%)	0.62 (10%)	1.00 (16%)	1.52 (24%)	1.62 (24%)
CL 0159+0030	0.38 (9%)	0.14 (3%)	0.27 (7%)	0.29 (7%)	0.41 (10%)	0.66 (16%)	1.08 (26%)	1.08 (26%)
CL 0230+1836	3.75 (37%)	0.58 (6%)	1.56 (16%)	2.36 (23%)	1.02 (10%)	1.64 (16%)	2.08 (20%)	2.08 (20%)
CL 0809+2811	1.19 (13%)	0.39 (4%)	0.74 (8%)	0.80 (9%)	0.92 (10%)	1.48 (16%)	1.97 (21%)	1.97 (21%)
CL 1357+6232	0.58 (23%)	0.14 (6%)	0.26 (10%)	0.33 (13%)	0.25 (10%)	0.40 (16%)	0.71 (28%)	0.71 (28%)
CL 1416+4446	0.28 (16%)	0.07 (4%)	0.11 (7%)	0.12 (7%)	0.17 (10%)	0.27 (16%)	0.44 (29%)	0.44 (29%)
CL 1641+4001	0.41 (20%)	0.12 (6%)	0.24 (12%)	0.27 (13%)	0.21 (10%)	0.33 (16%)	0.58 (29%)	0.58 (29%)
CL 1701+6414	0.42 (21%)	0.12 (6%)	0.21 (10%)	0.21 (10%)	0.20 (10%)	0.32 (16%)	0.58 (29%)	0.58 (29%)

**Notes.** We list all components entering (Eq. (10)): the uncertainties  $\sigma_{\text{cali}}^{\pm}$  due to shear calibration, and  $\sigma_{\text{geom}}^{\pm}$  from  $\langle D_{\text{ds}}/D_{\text{s}} \rangle$ , the projectional uncertainty  $\sigma_{\text{proj}}^{\pm}$  due to cluster triaxiality, and  $\sigma_{\text{LSS}}^{\pm}$  from the projection of unrelated LSS. All errors are given in units of  $10^{14} M_{\odot}$ ; the numbers in parentheses present the relative uncertainties. The relative statistical uncertainties are relatively independent of the choice of the concentration parameter.

to the  $r'$ -band source counts in the CL 0030+2618 and CL 1641+4001 fields, our observations with the deepest limiting magnitudes and a high density  $n_{\text{KSB}} \gtrsim 40 \text{ arcmin}^{-2}$  in the KSB catalogues (cf. Tables 1 and 2). The other cluster catalogues exhibit a completeness limit (peak in the source count histograms) at slightly brighter  $r'$ -magnitudes, but follow the Deep 1 closer than the corresponding, alternative  $r^+$ -band source counts from the COSMOS photo- $z$  catalogue (Ilbert et al. 2009). In order to test for a possible bias in  $\langle \beta \rangle$  for the shallower cluster fields, we repeat the fit to the redshift distributions from the four Deep fields with the following modification: Introducing a magnitude cut, we remove all galaxies with  $r' > r'_{\text{max}}$  from the CFHTLS catalogues. Virtually independent of  $z_{\text{d}}$ , we find the  $\langle \beta \rangle$  for the cases with and without magnitude cut to agree within mutual error bars for  $r'_{\text{max}} \gtrsim 25.2$ , meaning that the variation within the Deep fields has the same amplitude as the effect of removing the faintest sources. In our shallowest field, CL 0230+1836, we measure a limiting magnitude of  $r'_{\text{lim}} = 25.1$ , with 15% of galaxies in the galaxy shape catalogue at  $r' > 25.2$ . We thus conclude that no significant bias in  $\langle \beta \rangle$  is introduced by using the full Ilbert et al. (2006) catalogue as a redshift distribution proxy and the dispersion among the four fields as its uncertainty.

### 6.3. Dilution by cluster members

As in the case of CL 0030+2618, we not only consider the uncertainty of  $\pm 0.05$  we estimate for  $f_0$ , but also take into account the dilution by remaining foreground galaxies in the shear calibration error. Once again using the CFHTLS Deep 1 photo- $z$  catalogue as a proxy, we determine the fraction of galaxies

at  $z_{\text{ph}} < z_{\text{cl}}$  after applying the respective background selection. We measure this fraction  $\hat{f}_{\text{d}}$  to increase with  $z$ : it varies from 8.7% for CL 0159+0030 to 32.1% for CL 0230+1836 (Table 3). As can be seen for CL 0809+2811 and CL 1416+4446 at the same redshift  $z = 0.40$ , the background selection based on three bands results in a lower  $\hat{f}_{\text{d}} = 10.5\%$  than the mere magnitude cut ( $\hat{f}_{\text{d}} = 13.6\%$ ) for only one band. Adding the two components of the error in quadrature, the lower limit we consider for  $f_0$  ranges from 0.97 for CL 0159+0030 to 0.73 for CL 0230+1836.

### 6.4. Uncorrelated large scale structure

To calculate the error  $\sigma_{\text{LSS}}$  induced by LSS, we need to extrapolate the findings of Hoekstra (2003), covering only the cases of  $5h^{-1}$ ,  $10h^{-1}$ , and  $20h^{-1} \times 10^{14} M_{\odot}$  to lower masses. (Note that our  $M^{\text{wl}}$  estimate for CL 0030+2618 is very close to the first case.) The respective error contributions read from Fig. 6 of Hoekstra (2003) are  $\sim 1.2h^{-1}$ ,  $\sim 1.7h^{-1}$ , and  $\sim 2.7h^{-1} \times 10^{14} M_{\odot}$ . By assuming that the relative LSS error  $\sigma_{\text{LSS}}/M^{\text{wl}}$  increases linearly towards smaller masses, we arrive at the following relation:

$$\sigma_{\text{LSS}}/(10^{14} M_{\odot}) = aM_{14} + bM_{14}^2, \quad (11)$$

where  $a = 0.22h^{-1}$ ,  $b = -0.01$ , and  $M_{14} = M^{\text{wl}}/(10^{14} M_{\odot})$ . We understand Eq. (11) as an order-of-magnitude estimate for the LSS error and stress that simulated WL measurements are required to provide a better understanding of this important source of uncertainty. In particular, we expect a larger  $\sigma_{\text{LSS}}$  for higher  $z_{\text{d}}$  clusters, for which the existence of intervening massive

structure is more likely. We notice that the results of [Hoekstra \(2003\)](#) are obtained at  $z = 0.3$ , more nearby than our clusters.

In the special case of CL 1701+6414, the obvious LSS at  $z \approx 0.22$  was taken into account by explicit modelling, in addition to what is described here. We estimate the error associated with the covariance of the parameters describing the two clusters in our simultaneous model for CL 1701+6414 and A 2264 (cf. 4.1) by varying the otherwise fixed  $r_{200}$  of A 2264. The additional error from considering  $r_{s,200} = 0.8$  Mpc and  $r_{s,200} = 1.0$  Mpc, according to the uncertainties from our four-parameter fit, give a negligible contribution to the statistical error. Nevertheless, we caution that an additional uncertainty likely arises from our model choice.

### 6.5. Triaxiality projection bias

Applying the [Kasun & Evrard \(2005\)](#) fitting formula for the largest-to-smallest axis ratio of a triaxial halo as a function of mass to all our eight clusters, we arrive at expectation values of  $0.60 < \eta < 0.64$  for the largest-to-smallest axis ratio. Hence, considering the triaxiality biases of [Corless & King \(2007\)](#), we use  $\sigma_{\text{proj}}^+ = 0.16 M^{\text{wl}}$  for the error  $M^{\text{wl}}$  induced by overestimation and  $\sigma_{\text{proj}}^- = 0.10 M^{\text{wl}}$  for the one induced by underestimation caused by the projection of triaxial halos.

## 7. Discussion

The statistical, systematic, and total errors for all eight clusters are summarised in Table 6, both as absolute masses and as relative errors. Table 7 provides the details on the composition of the systematic error for the eight clusters. We note that for all our clusters, in particularly the ones with small WL masses, the statistical uncertainties are the largest component in the total error (the second largest usually being the projection of unrelated LSS). The relative statistical errors range between  $\approx 30\%$  and  $\approx 60\%$ . The reason for this can be twofold: First, the large statistical uncertainties *per se* are caused by the small signal-to-noise in the lensing signals and thus a consequence of the low net exposure times in the lensing-band images, once we removed frames with high PSF anisotropy (Table 1). Second, our account of the systematics might underestimate or neglect contributions to the systematic error.

For instance, uncertainties in the determination of the centres and the radial fitting ranges are not considered in Eq. (10), which we discuss in Sect. 7.2. After checking the statistical validity of our cluster detection in Sect. 7.1, we evaluate several effects influencing the accuracy with which we can measure weak lensing masses. A reliable quantification of all of these uncertainties is beyond the scope of this article but very desirable with respect to the constraints on cosmology at which the next generation of cluster weak lensing projects is aiming.

### 7.1. Significance of cluster detections

The  $S$ -statistics is known to produce spurious shear peaks even at high significance levels, although as simulations show, false detections above the  $\sim 4\sigma$  level are rare (e.g., [Hettterscheidt et al. 2005](#); [Dietrich et al. 2007](#)). Still, in principle, there is a nonzero, but small chance for one or the other of our detections to be false. Spurious detections are more sensitive against changes in the lensing catalogue or  $\theta_{\text{out}}$ . Our tests with different photometric cuts and values for  $\theta_{\text{out}}$  found our cluster shear peaks to be robust. Another reaffirmation is the persistence of signals when bootstrapping the lensing catalogue, which we performed for CL 1357+6232, and CL 1416+4446.

In order to test the interpretation of  $S$ -values as significances, we conducted the following test: for each galaxy in the catalogue, we add to the phase  $\varphi$  of the complex ellipticity estimator  $\varepsilon = |\varepsilon| \exp(2i\varphi)$  an additional term  $\varphi_{\text{rnd}}$  drawn randomly from a uniform distribution in the interval  $0 \leq \varphi_{\text{rnd}} < \pi$ . This procedure should completely remove the lensing signal from the data such that the resulting value of  $S$  be normally distributed around zero, with a standard deviation  $\sigma = 1$ .

We produced  $10^6$  realisations of such a randomised catalogue for each cluster and find the  $S$ -distributions for all eight cluster detection to be well represented by a Gaussian distribution. In all cases, the absolute of the mean value  $\mu$  of the fitted Gaussian is  $|\mu| < 0.002$ , and of the same order of magnitude as the uncertainty in  $\mu$  derived from the fit. We do not find a bias to either positive or negative  $S$ . For six of the eight clusters, we find for the standard deviations  $\sigma$  of the fitted Gaussians values of  $|1 - \sigma| < 0.01$ , with  $\sigma = 0.962$  and CL 1416+4446 and  $\sigma = 0.978$  for CL 1641+4001, respectively, the largest measured deviations from the expected  $\sigma = 1$ .

For only one cluster, we find one  $|S| > 5$  event among the  $10^6$  realisations, consistent with the expectation of one such event in  $1.7 \times 10^6$  realisations of the expected Gaussian distribution  $G$ . Therefore, we conclude that this randomisation test does not find indications for an overestimation of the significance of our cluster detections, as inferred from the  $S$ -statistics. On the contrary, the small standard deviations measured from the fits to the CL 1416+4446 and CL 1641+4001 correspond to very slightly underestimated significances of these two cluster detections.

### 7.2. The role of cluster centres

[Dietrich et al. \(2012\)](#) recently demonstrated that the  $S$ -peak gives a robust determination of the cluster centre, showing little susceptibility to projected large scale structure (LSS). However, using  $S$ -peaks as cluster centres for WL mass estimates is likely to result in a systematic overestimation of cluster masses, because we pick such centres that produce the highest masses. In addition to our default ROSAT centres, we partnered all cluster models with a model choosing the  $S$ -peak as cluster centre. While we plan to quantify the centring bias once a more complete sample of our clusters is available, we can show overall trends based on the eight clusters discussed here.

The separations between the shear peaks and ROSAT centres are  $< 3'$  in all cases and  $< 1'$  for four of the eight clusters (Table 3). This coincidence of X-ray and lensing centres adds further significance to the  $S$ -detections. Two out of the four remaining clusters, CL 0159+0030 and CL 0809+2811, have their  $S$ -peaks within larger masked areas, reducing the accuracy with which the centres can be determined. The complicated shear fields in the vicinities of CL 1701+6414 and CL 1641+4001, with separations  $> 1'$  between lensing and ROSAT centres are discussed in Sects. 4.1 and 4.2. We note that the ROSAT cluster centres themselves are accurate to  $\sim 10''$ .

First, we notice that the  $S$ -centred masses are biased high for six of the eight clusters (squares in Fig. 9). The median is a 9% higher mass using shear peak centres ( $M_{200}^{\text{S-cen}}$ ) than with ROSAT centres ( $M_{200}^{\text{R-cen}}$ ). We measure  $\langle M_{200}^{\text{S-cen}}/M_{200}^{\text{R-cen}} \rangle = 1.25$ , with a 0.36 standard deviation. This indicates the expected presence of a centring bias, although a small one compared to its scatter.

The most extreme differences are measured for the low-concentration clusters CL 1641+4001 and CL 1701+6414. The sorting in Fig. 9 by increasing  $c_{200}$  in the  $S$ -centred model seems to suggest a trend of a larger  $M_{200}^{\text{S-cen}}/M_{200}^{\text{R-cen}}$  in clusters

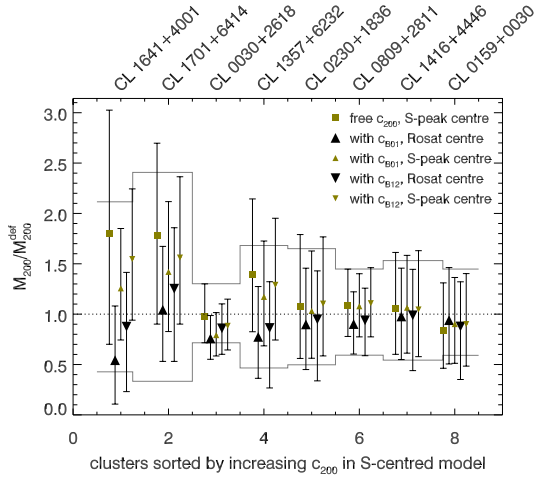


**Fig. 9.** Dependence of weak lensing cluster masses on the choice of centre and mass-concentration-relation. Upward and downward triangles show the masses using the B01 and B12 mass-concentration-relation relative to the case of a free  $c_{200}$ . The square and small triangles present models centred on the  $S$ -peaks for the free- $c_{200}$ , B01, and B12 cases, respectively. Clusters are ordered by increasing (free)  $c_{200}$  in the  $S$ -centred model. Grey lines denote the statistical error bars in the reference model (ROSAT-centred, free  $c_{200}$ ).

of low concentration. We do not see a similar trend when sorting clusters by  $\Delta\theta$ , the separation between the two types of centres (cf. Table 3), but caution that we deal with small number statistics. When applying the B01 (B12) mass–concentration relations (big and small upward and downward triangles in Fig. 9), we arrive at similar results, with higher median biases of 18% (20%), but still large scatter.

### 7.3. Low concentration clusters

As Fig. 9 shows, the relative differences between masses measured with the six different models for centre and concentration parameter are most pronounced for CL 1641+4001 and CL 1701+6414, the two clusters with the lowest intrinsic concentrations  $c_{200}^{S\text{-cen}}$ .

First we remark, that low values for  $c_{200}$  are neither unexpected nor unheard of in the weak lensing literature (cf., e.g., Oguri et al. 2010; Planck Collaboration 2012). Small concentration parameters as in CL 0809+2811 or CL 1357+6232 are not unique to our analysis method, especially when using a cluster centre significantly offset from the shear peak or in fields affected by masks in the data. Our analysis highlights the importance of such effects.

We note that, using an elliptical NFW cluster model, Oguri et al. (2010) found four out of the 25 X-ray selected clusters they analysed a best-fit  $c_{\text{vir}} < 1$ . These four extreme cases are among the clusters Oguri et al. (2010) exclude from further analysis for centring problems or obvious misfit of the assumed model. The authors do not, however, report similar problems for three further clusters with  $1 < c_{\text{vir}} < 2$ .

The more extreme cases of CL 1641+4001 and CL 1701+6414 point to the limitations of describing a cluster shear field using a single, spherically symmetric function, even if obvious line-of-sight structure like A 2264 is taken into account. Nevertheless, tests like the comparison of  $\kappa$ -maps for CL 1701+6414 from MMT and CFHT (Sect. 5.3) demonstrate that the measured low concentration parameters reflect the reality of the mass distribution and are not artifacts of the analysis. Concerning cosmological applications, the rejection of such clusters will likely result in a biased mass, which we

**Table 8.** Three bright stars exacerbating the analysis of the CL 0159+0030, CL 0230+1836, and CL 0809+2811 fields, identified by their BD and HD designations.

BD	HD	$\alpha_{J2000}$	$\delta_{J2000}$	$\theta$	$m_V$	Spec.
−00 301	12134	01:59:10.3	+00:30:24	1.94′	8.28	F0
+18 315	15551	02:30:30.1	+18:39:51	3.59′	8.25	K0
+28 1562	67543	08:09:34.3	+28:11:46	1.51′	8.60	F0

**Notes.** We cite SIMBAD (<http://simbad.u-strasbg.fr/simbad/>) for stellar positions,  $V$  magnitudes and spectral types (Spec.). By  $\theta$  we denote the separations between the respective ROSAT cluster centre and star.

prefer to avoid. We notice that, making different choices in the data analysis, High et al. (2012) likewise succeed in measuring masses of clusters showing a flat shear profile.

### 7.4. Influence of mass-concentration-relations

Comparing the masses obtained with the three different choices for  $c_{200}$  (free parameter, B01 and B12 mass-concentration relations; Fig. 9 and Table 4), we observe interesting trends. Intrinsically, the B12 relation yields lower concentrations for the same cluster than B01. This relates to the result that the mass assuming B01 exceeds the B12 mass, except for CL 0159+0030. Despite the overall agreement of the masses within their errors, the spread between the two masses seems to decrease with  $c_{200}$ , independent of the choice of centre.

On average, using a mass-concentration relation results in a lower mass estimate compared to a free  $c_{200}$ , with  $\sim 1\sigma$  significance for the B01 relation ( $\langle M_{200,B01}/M_{200,def} \rangle = 0.85 \pm 0.16$ ) and less so for the B12 relation ( $\langle M_{200,B12}/M_{200,def} \rangle = 0.95 \pm 0.13$ ).

For the  $S$ -peak-centred masses, we obtain a similar picture. The B01 masses increase relative to the free- $c_{200}$  masses, following this trend monotonically despite the statistical uncertainties. In Fig. 9, this can be seen looking at the squares and small upward triangles. The correlation can be explained by the shape found in the confidence contours of most of the clusters for which  $c_{200}$  can be constrained (e.g. CL 1357+6232; Fig. 2): Relatively high values for  $c_{200}$  only agree with the data for  $r_{200}$  smaller than the best-fit value. The underlying reason is the absolute value of the shear signal ruling out simultaneously higher values for  $c_{200}$  and  $r_{200}$ .

It will be interesting to see if the tentative trends in Fig. 9 will persist for a more complete cluster sample. We note that due to the substructure and non-sphericity of  $\Lambda$ CDM halos, we expect mass-concentration measured with weak lensing to be biased with respect to the more direct estimates from the simulations (e.g., Bahé et al. 2012). At the current level of eight clusters, all mass estimates agree with each other within their error margins. We notice the relative statistical uncertainties to be only weakly dependent on the choice of  $c_{200}$  (free parameter, B01, or B12 mass- $c_{200}$ -relations).

### 7.5. Masking of bright stars

In Table 8, we summarise the properties of the magnitude 8–9 stars that impede the analysis in the CL 0159+0030, CL 0230+1836, and CL 0809+2811 fields. By coincidence, these three most severe cases among the sample of 36 clusters are among our MegaCam targets, reminding us that such fields must not be discarded when analysing a statistically complete sample. Using the example of CL 0809+2811, we study the impact of these stars and their masking on the  $S$ -maps and mass estimates.

Removing the masks generated for regions of deviant source density (Sect. 2.2, red squares in Fig. D.3) does not increase the number of usable galaxies significantly: Where scattered light strongly affects the local background estimation, sources are discarded in an early stage of catalogue preparation. At the position of the ROSAT centre, there are no detections in the first place. Without masking, the  $S$ -peak of CL 0809+2811 is shifted by 2.4 to the north-east (closer to the ROSAT centre) and very slightly lower ( $S_{\max} = 5.27$  instead of  $S_{\max} = 5.39$ ). Because our default model excises galaxies at  $<1.5$  separation, to avoid the strong lensing regime, the impact on the mass is below 2%.

A more important point could be the extra uncertainty in the chosen cluster centre, as we find the largest offsets between WL and X-ray peaks for clusters with large masks. The  $M_{200}^{S-\text{cen}} < M_{200}^{R-\text{cen}}$  observed for CL 0159+0030 (Fig. 9) is likely due to a washed-out lensing peak. Nevertheless, we do not observe similar peculiarities for CL 0809+2811.

### 7.6. Further sources of uncertainty

There are several potential sources of uncertainty which are not considered in Eq. (10), for instance, uncertainties in the determination of the centres or the contamination correction available only for clusters imaged in  $g'r'i'$ . A reliable quantification of these errors will require further analysis.

We also do not consider the uncertainty in the choice of  $\max(|\epsilon|)$  in the error analysis. However, we account for its effect via the shear calibration such that we do not expect a significant additional systematic error. Carefully calibrated simulations of cluster lensing are necessary to test our assumptions on the shear calibration factor. In Paper I, we observed in CL 0030+2618 a counter-intuitive decrease of the best-fit value for  $r_{200}^{\min}$  with increasing  $\max(|\epsilon|)$ . Indeed, only CL 1357+6232 shows a similar relative decrease in  $r_{200}^{\min}$ . Averaging over all eight clusters, these cases are balanced by CL 0230+1836 and CL 1416+4446, for which we measure  $r_{200}^{\min}$  to increase with  $\max(|\epsilon|)$ . With  $\max(|\epsilon|) = 1.0$ , we measure for four cases a smaller  $r_{200}^{\min}$  than for  $\max(|\epsilon|) = 0.8$ , and in four cases a larger radius. The same holds for  $\max(|\epsilon|) = 10^4$ . These results suggest that the uncorrected bias due to  $\max(|\epsilon|)$  might be small.

We notice that the roles of the shear calibration  $f_0$ , considered in Eq. (10) as  $\sigma_{\text{cali}}$  and the correction  $f_1(\theta)$  for cluster members cannot be completely disentangled. On the one hand, considering the cluster member correction separately is justified by the radial dependence of  $f_1(\theta)$ . On the other hand, we stress that the uncertainty in  $f_1(\theta)$  might be large due to the weak detections of the cluster red sequence. In addition, the effect of cluster member decontamination on the mass estimate (3% to 7%; up to 11% using shear-peak centres) lies within the range of the related systematic error component  $\sigma_{\text{cali}}^-$  which is significantly smaller than the statistical uncertainty in the mass. Hence, a possible plan to consider cluster membership consistently – also for single-band clusters – would be to include it into the systematic error. Again, we suppose performing simulations of cluster WL fields to be helpful for the further investigations.

Finally, we note that total  $1\sigma$  error intervals consistent with cluster masses close to zero do not mean these clusters are detected merely at the  $\sim 1\sigma$  level: shear calibration,  $z_s$ -distribution, and triaxiality errors are multiplicative, such that they do not affect the detection significance.

## 8. Summary and conclusion

In this study, the second in the series on the 400d survey WL follow-up, we reduced and analysed MMT/MegaCam

observations for seven clusters of galaxies. Building on Paper I, data reduction is performed using THELI, and WL shear catalogues are extracted using an implementation of the KSB+ algorithm.

In the three cases, where we have MMT observations in  $g'r'i'$ , we define lensing catalogues based on a refined version of the three-colour method used in Paper I. By comparing with the colours observed for a Ilbert et al. (2006) photo- $z$  field, we exclude sources from regions in colour-colour-magnitude space containing a large fraction of foreground galaxies from the analysis. For clusters with only one MMT band, we apply a cut in magnitude as background selection.

We detect all of our  $0.39 < z < 0.80$  clusters using the aperture mass method ( $S$ -statistics) at the  $> 3.5\sigma$  level. Performing a Seitz & Schneider (2001) mass reconstruction, we find the projected mass to follow the  $S$ -statistics closely. The WL masses of our clusters are determined from NFW modelling of their tangential shear profiles, yielding masses in the  $10^{14} M_{\odot} \leq M_{200}^{\text{wl}} < 2 \times 10^{15} M_{\odot}$  interval.

Two of our clusters are exceptional due to their complicated shear morphology: For CL 1701+6414, where several known clusters lie close to one another in projection, we simultaneously fit the shear of the two strongest  $S$ -peaks, identified with A 2246 and our target. The field of CL 1641+4001 also exhibits multiple shear peaks, but we find no evidence for the presence of more than one cluster.

An independent analysis of the CL 1701+6414 field using archival CFHT data confirms the superposition of several weak lensing sources. By matching shear catalogues from MMT and CFHT, we find ellipticities measured with both instruments to be consistent with the assumption of noisy, but unbiased measurements of the same quantity. Hence, MMT/MegaCam is proven to be equally good for WL science as the well-established CFHT/MegaCam. We further produced a photo- $z$  catalogue based on CFHT  $g'r'i'z'$  data of the field. Despite the shallowness of three bands, we are able to devise a coarse foreground/background selection for CL 1701+6414. This experiment again confirms not only shear peaks for several known clusters but also the validity of the magnitude-cut selection. Better photo- $z$  data will be needed to potentially turn this cross-check into a calibration for single-band lensing data.

We find the error budgets for our cluster masses to be dominated by statistical uncertainties (which can be suppressed by using a large cluster sample), but with a significant contribution of systematic uncertainties. Statistical uncertainties are naturally higher for relatively high- $z$  clusters like ours, but the role of data quality (weather and instrumental conditions that led to drastic reductions in data depth) can hardly be overestimated. Our data show weak indications for clusters with low intrinsic concentration to be more susceptible to model choices, such as the concentration parameter or assumed centre.

As the second paper in the 400d WL series, the main results of this study are that:

- Instrumental effects are well under control.
- Reliable masses can be obtained in the presence of bright stars close to the cluster centre – an important finding for a successful follow-up of a complete sample!
- Ground-based WL works at least till  $z \approx 0.8$ .
- We can correct for extreme cases of massive foreground structures.
- Clusters of low concentration are a common occurrence in the high redshift, moderate mass population.

Furthermore, we identify areas of possible future improvements of the methods we applied: As observational constraints will forbid complete homogeneity of the data analysis to some degree for each survey. Therefore, better methods to calibrate WL analyses in particular with a different number of available filters need to be developed. This applies specifically to background selection and correction for cluster members.

Concerning the modelling of clusters with complex shear morphology, we point out that low-mass clusters with a strong fraction of disturbed or merging systems will build the bulk of the population observed by deep and wide future surveys like EROSITA or EUCLID. Hence, the question arises how clusters deviating from a simple NFW mass distribution can be weighed most accurately. A possible method is to apply methods that do not assume radial symmetry, e.g. aperture mass techniques. Nevertheless, profile-fitting methods are well established and increasingly well understood. Alternatively, by combining simulation efforts with improved data analysis and modelling, biases resulting from profile assumptions can be corrected. Thus, applying profile fits even to low-signal, merging clusters might prove the best method to measure reliable masses for large cluster samples.

*Acknowledgements.* H.I. likes to thank Frank Bertoldi for support of this work and Matthias Klein, Reiko Nakajima, Mischa Schirmer, Ismael Tereno, Bharadwaj Vijaysarathy, Daniela Wuttke, and Yu-Ying Zhang for helpful discussions. Partial support for this work has come from the Deutsche Forschungsgemeinschaft (DFG) through Transregional Collaborative Research Centre TRR 33 as well as through the Schwerpunkt Program 1177. T.H.R. acknowledges support from the DFG through Heisenberg grant RE 1462/5 and grant RE 1462/6. C.L.S. was supported in part by *Chandra* grants GO9-0135X, GO9-0148X, and GO1-12169X, and by the F. H. Levinson Fund of the Silicon Valley Community Foundation, which helped support the MMT observations. We acknowledge the grant of MMT observation time (program 2007B-0046) through NOAO public access.

## References

- Adelman-McCarthy, J. K., Agüeros, M. A., Allam, S. S., et al. 2008, *ApJS*, 175, 297
- Allen, S. W., Evrard, A. E., & Mantz, A. B. 2011, *ARA&A*, 49, 409
- Bahé, Y. M., McCarthy, I. G., & King, L. J. 2012, *MNRAS*, 421, 1073
- Barkhouse, W. A., Green, P. J., Vikhlinin, A., et al. 2006, *ApJ*, 645, 955
- Bartelmann, M. 1996, *A&A*, 313, 697
- Benítez, N. 2000, *ApJ*, 536, 571
- Bertin, E., & Arnouts, S. 1996, *A&AS*, 117, 393
- Bhattacharya, S., Habib, S., & Heitmann, K. 2011 [arXiv:1112.5479] (B12)
- Blanchard, A. 2010, *A&ARv*, 18, 595
- Böhringer, H., & Werner, N. 2010, *A&ARv*, 18, 127
- Bolzonella, M., Miralles, J., & Pelló, R. 2000, *A&A*, 363, 476
- Bullock, J. S., Kolatt, T. S., Sigad, Y., et al. 2001, *MNRAS*, 321, 559 (B01)
- Burenin, R. A., & Vikhlinin, A. A. 2012, *Astron. Lett.*, 38, 647
- Burenin, R. A., Vikhlinin, A., Hornstrup, A., et al. 2007, *ApJS*, 172, 561
- Cohn, J. D., & White, M. 2005, *Astropart. Phys.*, 24, 316
- Coleman, G. D., Wu, C.-C., & Weedman, D. W. 1980, *ApJS*, 43, 393
- Corless, V. L., & King, L. J. 2007, *MNRAS*, 380, 149
- Corless, V. L., & King, L. J. 2009, *MNRAS*, 396, 315
- Dietrich, J. P., Erben, T., Lamer, G., et al. 2007, *A&A*, 470, 821
- Dietrich, J. P., Böhnert, A., Lombardi, M., Hilbert, S., & Hartlap, J. 2012, *MNRAS*, 419, 3547
- Donahue, M., Scharf, C. A., Mack, J., et al. 2002, *ApJ*, 569, 689
- Eke, V. R., Cole, S., & Frenk, C. S. 1996, *MNRAS*, 282, 263
- Erben, T., van Waerbeke, L., Bertin, E., Mellier, Y., & Schneider, P. 2001, *A&A*, 366, 717
- Erben, T., Schirmer, M., Dietrich, J. P., et al. 2005, *Astron. Nachr.*, 326, 432
- Erben, T., Hildebrandt, H., Lerchster, M., et al. 2009, *A&A*, 493, 1197
- Goto, T., Sekiguchi, M., Nichol, R. C., et al. 2002, *AJ*, 123, 1807
- Hartlap, J., Schrabback, T., Simon, P., & Schneider, P. 2009, *A&A*, 504, 689
- Hetterscheidt, M., Erben, T., Schneider, P., et al. 2005, *A&A*, 442, 43
- Heymans, C., van Waerbeke, L., Bacon, D., et al. 2006, *MNRAS*, 368, 1323
- High, F. W., Stubbs, C. W., Rest, A., Stalder, B., & Challis, P. 2009, *AJ*, 138, 110
- High, F. W., Hoekstra, H., Leethochawalit, N., et al. 2012, *ApJ*, 758, 68
- Hildebrandt, H., Erben, T., Dietrich, J. P., et al. 2006, *A&A*, 452, 1121
- Hoekstra, H. 2003, *MNRAS*, 339, 1155
- Ilbert, O., Arnouts, S., McCracken, H. J., et al. 2006, *A&A*, 457, 841
- Ilbert, O., Capak, P., Salvato, M., et al. 2009, *ApJ*, 690, 1236
- Israel, H., Erben, T., Reiprich, T. H., et al. 2010, *A&A*, 520, A58
- Kaiser, N., & Squires, G. 1993, *ApJ*, 404, 441
- Kaiser, N., Squires, G., & Broadhurst, T. 1995, *ApJ*, 449, 460
- Kasun, S. F., & Evrard, A. E. 2005, *ApJ*, 629, 781
- Komatsu, E., Smith, K. M., Dunkley, J., et al. 2011, *ApJS*, 192, 18
- Kowalski, M., Rubin, D., Aldering, G., et al. 2008, *ApJ*, 686, 749
- Kravtsov, A. V., Vikhlinin, A., & Nagai, D. 2006, *ApJ*, 650, 128
- Larson, D., Dunkley, J., Hinshaw, G., et al. 2011, *ApJS*, 192, 16
- Lopes, P. A. A., de Carvalho, R. R., Gal, R. R., et al. 2004, *AJ*, 128, 1017
- Mantz, A., Allen, S. W., Rapetti, D., & Ebeling, H. 2010, *MNRAS*, 406, 1759
- McLeod, B. A., Conroy, M., Gauron, T. M., Geary, J. C., & Orndway, M. P. 2000, in *Further Developments in Scientific Optical Imaging*, ed. M. B. Denton, 11
- Medezinski, E., Broadhurst, T., Umetsu, K., et al. 2010, *MNRAS*, 405, 257
- Meneghetti, M., Rasia, E., Merten, J., et al. 2010, *A&A*, 514, A93
- Miller, C. J., Nichol, R. C., Reichart, D., et al. 2005, *AJ*, 130, 968
- Nagai, D., Kravtsov, A. V., & Vikhlinin, A. 2007a, *ApJ*, 668, 1
- Nagai, D., Vikhlinin, A., & Kravtsov, A. V. 2007b, *ApJ*, 655, 98
- Navarro, J. F., Frenk, C. S., & White, S. D. M. 1995, *MNRAS*, 275, 720
- Navarro, J. F., Frenk, C. S., & White, S. D. M. 1996, *ApJ*, 462, 563
- Navarro, J. F., Frenk, C. S., & White, S. D. M. 1997, *ApJ*, 490, 493
- Oguri, M., Takada, M., Okabe, N., & Smith, G. P. 2010, *MNRAS*, 405, 2215
- Pillepich, A., Porciani, C., & Hahn, O. 2010, *MNRAS*, 402, 191
- Pillepich, A., Porciani, C., & Reiprich, T. H. 2012, *MNRAS*, 422, 44
- Planck Collaboration 2012, *A&A*, in press, DOI: 10.1051/0004-6361/201219398
- Pionis, M., Basilakos, S., Georgantopoulos, I., & Georgakakis, A. 2005, *ApJ*, 622, L17
- Predehl, P., Andritschke, R., Böhringer, H., et al. 2010, in *SPIE Conf. Ser.*, 7732
- Press, W. H., & Schechter, P. 1974, *ApJ*, 187, 425
- Rasia, E., Ettori, S., Moscardini, L., et al. 2006, *MNRAS*, 369, 1013
- Reimers, D., Toussaint, F., Hagen, H., Hippelein, H., & Meisenheimer, K. 1997, *A&A*, 326, 489
- Reiprich, T. H. 2006, *A&A*, 453, L39
- Romer, A. K., Nichol, R. C., Holden, B. P., et al. 2000, *ApJS*, 126, 209
- Rosat, P., Borgani, S., & Norman, C. 2002, *ARA&A*, 40, 539
- Sarazin, C. L. 1988, *X-ray emission from clusters of galaxies* (Cambridge University Press)
- Schirmer, M., Erben, T., Hetterscheidt, M., & Schneider, P. 2007, *A&A*, 462, 875
- Schneider, P. 1996, *MNRAS*, 283, 837
- Schneider, P. 2006, *Weak Gravitational Lensing in: Gravitational Lensing: Strong, Weak and Micro: Saas-Fee Advanced Courses* (Springer-Verlag Berlin Heidelberg), 33, 269
- Schneider, P., King, L., & Erben, T. 2000, *A&A*, 353, 41
- Schrabback, T., Erben, T., Simon, P., et al. 2007, *A&A*, 468, 823
- Schrabback, T., Hartlap, J., Joachimi, B., et al. 2010, *A&A*, 516, A63
- Schuecker, P. 2005, in *Rev. Mod. Astron.*, 18, ed. S. Röser, 76
- Seitz, S., & Schneider, P. 1996, *A&A*, 305, 383
- Seitz, S., & Schneider, P. 2001, *A&A*, 374, 740
- Stanek, R., Rasia, E., Evrard, A. E., Pearce, F., & Gazzola, L. 2010, *ApJ*, 715, 1508
- van Waerbeke, L., Mellier, Y., Radovich, M., et al. 2001, *A&A*, 374, 757
- Vikhlinin, A., McNamara, B. R., Forman, W., et al. 1998, *ApJ*, 502, 558
- Vikhlinin, A., Burenin, R. A., Ebeling, H., et al. 2009a, *ApJ*, 692, 1033
- Vikhlinin, A., Kravtsov, A. V., Burenin, R. A., et al. 2009b, *ApJ*, 692, 1060
- Voit, G. M. 2005, *Rev. Mod. Phys.*, 77, 207
- von der Linden, A., Best, P. N., Kauffmann, G., & White, S. D. M. 2007, *MNRAS*, 379, 867
- Wright, C. O., & Brainerd, T. G. 2000, *ApJ*, 534, 34
- Zhang, Y.-Y., Finoguenov, A., Böhringer, H., et al. 2008, *A&A*, 482, 451
- Zhang, Y.-Y., Okabe, N., Finoguenov, A., et al. 2010, *ApJ*, 711, 1033

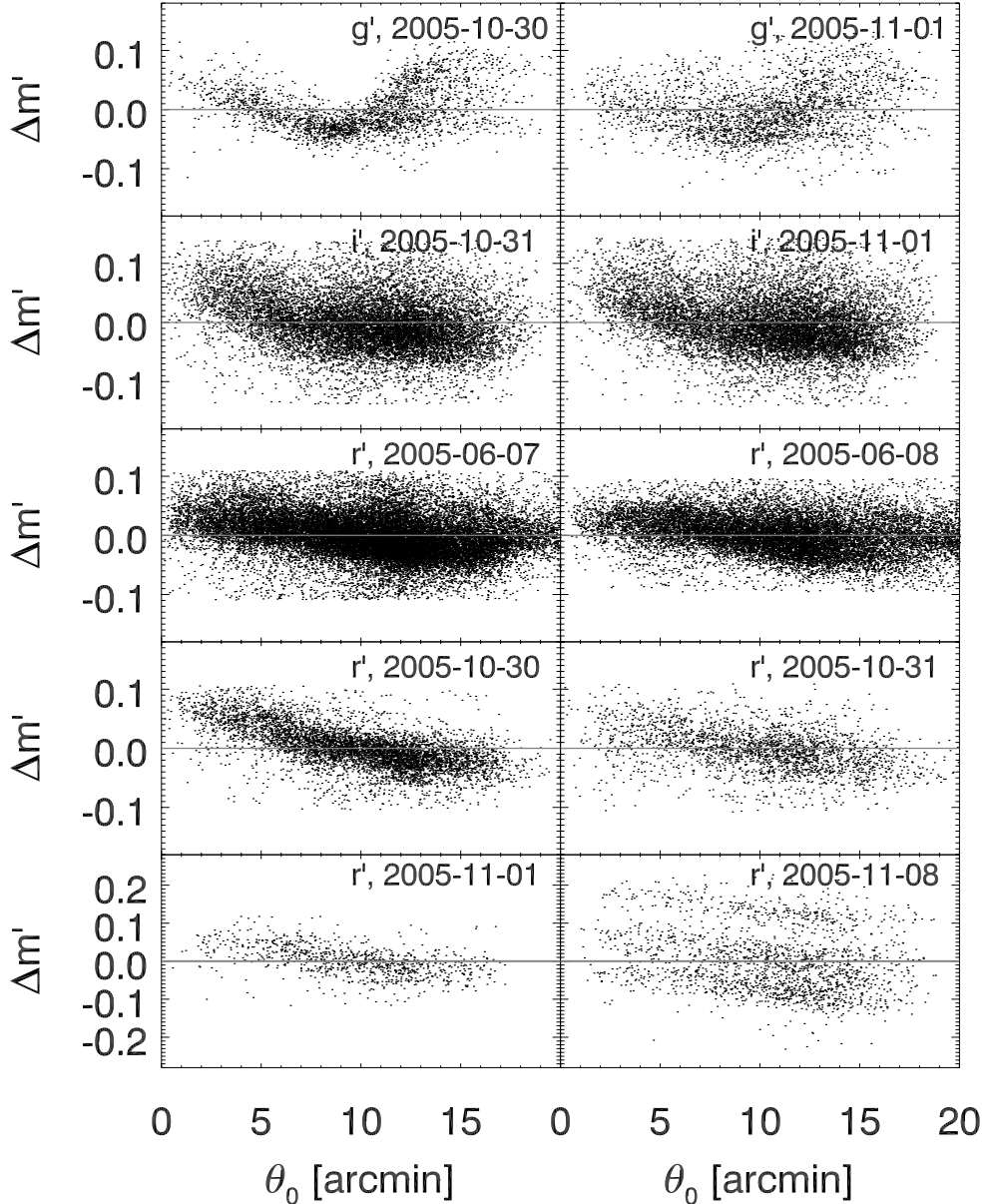


**Fig. A.1.** Accuracy of the photometric calibration: For the different combinations of filters and nights used to calibrate the data sets discussed in this work and Paper I, the scatter  $\Delta m'$  around the best-fit solution (solid line) is shown. Each point corresponds to an SDSS standard source for which the abscissae give the separation  $\theta_0$  in arc minutes from the centre of the pointing. Note that for each panel a maximum  $\Delta m'$  has been determined by iterative  $3\sigma$ -clipping.

## Appendix A: Photometric calibration details

Applying the [Hildebrandt et al. \(2006\)](#) method, photometric calibration of our data is established by fitting instrumental ( $m_{\text{inst}}$ ) to reference ( $m_{\text{SDSS}}$ ) magnitudes for a sample of objects, taking into account variable airmass  $a$  and a colour term  $c_{\text{SDSS},f}$  describing the transformation between MegaCam and SDSS filter systems:

$$m_{\text{inst}} - m_{\text{SDSS}} = \beta_f c_{\text{SDSS},f} + \gamma_f a + Z_f, \quad (\text{A.1})$$

Depending on the photometric quality of the observations, we fit the zeropoint  $Z_f$  together with the parameters  $\beta_f$  or  $\gamma_f$  in optimal conditions, or keep  $\gamma_f$  fixed at the default value depending on the filter  $f$  for poorer conditions.

The resulting values for the fit parameters, as well as the colour indices  $c_{\text{SDSS},f}$  for the different filters are presented in

Table A.1, for all photometric nights of our MegaCam runs<sup>11</sup>. We find the zeropoints  $Z_f$  of the photometric nights to agree among the  $g'r'i'$  filters, with a largest deviation of  $\approx 0.15$  mag. The scatter  $\Delta m' = m_{\text{inst}} - m_{\text{SDSS}} + \beta_f c_{\text{SDSS},f} + \gamma_f a + Z_f$  of the individual SDSS standards about the best-fit solution (Fig. A.1) has a comparable amplitude. The errors of  $Z_f$  given in Table A.1 are the formal fitting errors. Figure A.1 presents the data from which the fit parameters have been determined, applying an iterative  $3\sigma$ -clipping fit of Eq. (A.1).

Comparing the colour terms  $\beta_f$  for the different nights, we find considerable agreement within the values for each of the three bands, although the formal errors underestimate the true uncertainties. We suggest that the large span in values of  $\beta_g$

<sup>11</sup> Note that some values in Table A.1 are corrected w.r.t. Table A.1 in Paper I. The amount of these corrections is of the order of, and in most cases smaller than, the scatter observed in Fig. A.1.

**Table A.1.** Coefficients of photometric calibration defined by Eq. (A.1) for all photometric nights within our MMT/MegaCam 400d observations.

Filter	Obs. Date	$Z_r^\dagger$	$\beta_r$	$c_{\text{SDSS}}$	$\gamma_r$	$n_{\text{par}}^{\ddagger}$
$g'$	2005-10-30	$27.277 \pm 0.005$	$0.106 \pm 0.007$	$g' - r'$	$(-0.15)^\S$	2
	2005-11-01	$27.286 \pm 0.005$	$0.116 \pm 0.005$	$g' - r'$	$(-0.15)^\S$	2
$i'$	2005-10-31	$26.426 \pm 0.002$	$0.124 \pm 0.002$	$r' - i'$	$(-0.05)^\S$	2
	2005-11-01	$27.408 \pm 0.009$	$0.119 \pm 0.002$	$r' - i'$	$-0.03 \pm 0.01$	3
$r'$	2005-06-07	$26.819 \pm 0.001$	$0.040 \pm 0.001$	$g' - i'$	$(-0.10)^\S$	2
	2005-06-08	$26.834 \pm 0.008$	$0.048 \pm 0.001$	$g' - i'$	$-0.12 \pm 0.01$	3
	2005-10-30	$26.950 \pm 0.018$	$0.046 \pm 0.002$	$g' - i'$	$-0.10 \pm 0.02$	3
	2005-10-31	$26.959 \pm 0.004$	$0.042 \pm 0.003$	$g' - i'$	$(-0.10)^\S$	2
	2005-11-01	$26.960 \pm 0.008$	$0.048 \pm 0.004$	$g' - i'$	$(-0.10)^\S$	2
	2005-11-08	$26.807 \pm 0.005$	$0.046 \pm 0.003$	$g' - i'$	$(-0.10)^\S$	2

**Notes.** <sup>(†)</sup> Normalised to an exposure time of 1s and an airmass  $a = 0$ . <sup>(‡)</sup> Number of parameters used in the fit. <sup>(§)</sup> Fixed at the default value.

might be caused by the known dependence of the filter throughput on the distance to the optical axis. Plotting the scatter  $\Delta m'$  as a function of the separation  $\theta_0$  of the source from the optical axis of MegaCam (Fig. A.1), given by the pointing position in the fits header, we can confirm trends of  $\Delta m'(\theta_0)$  in all filters, most pronounced for the  $g'$  band data taken on 2005 October 30. This trend is likely caused by a combination of the sky concentration effect (position-dependent illumination due to scattering in the telescope optics) and the position-dependent transmissivity of the MegaCam filters, which is strongest in the  $g'$  band (cf. Fig. A.3 in Paper I). A more conclusive investigation of this issue, requiring full propagation of errors on instrumental magnitude, lies beyond the scope of this paper. Because the radial dependence observed in Fig. A.1 does not exceed the residual scatter for sources at the same  $\theta_0$ , the global photometric fits (Eq. (A.1)) fulfil the requirements of our analysis.

## Appendix B: Details of background selection

In the intermediate magnitude range  $m_{\text{bright}} \leq r' \leq m_{\text{faint}}$ , our lensing catalogues for three-band clusters include galaxies selected from  $g' - r'$  versus  $r' - i'$  colour-colour diagrams (Sect. 2.4). We find our method justified by considering the Ilbert et al. (2006) photo- $z$  catalogue:

Figure B.1 presents the galaxy numbers and the fraction of  $z_{\text{ph}} \leq 0.50$  sources in the Deep 1 photo- $z$  catalogue as a function of the  $r'$  magnitude and  $g' - r'$  and  $r' - i'$  colours. First, the catalogue is divided into its dodeciles in  $r'$ , i.e. twelve magnitude bins of equal population are defined where the  $k$ -th bin consists of the galaxies  $r'_{k-1} \leq r' < r'_k$ . By  $r'_k$ , we denote the magnitude of a source such there is a fraction of  $k/12$  of brighter galaxies in the catalogue. Second, for each dodecile, we show the number  $N_{ij}$  of galaxies falling into grid cells of mesh size  $\Delta(g' - r') = \Delta(r' - i') = 0.1$ , using a grey scale. Figure B.1 highlights that at bright  $r'$ , only a narrow strip in the colour-colour space spanned by  $g' - r'$  and  $r' - i'$  is populated, while the locus of galaxies becomes much more diffuse towards fainter  $r'$ . Third, for each grid cell, we determine the fraction of galaxies we define as foreground sources, i.e. the sources with a redshift estimate  $z_{\text{ph}} \leq 0.40$ . The red, green, and blue contours in Fig. B.1 mark regions of the colour-colour space populated by 25%, 50%, and 75% of foreground galaxies compared to the  $z_d = 0.40$  clusters, CL 0159+0030 and CL 0809+2811. The contours are defined such that  $f_{\text{fg}}$  exceeds the respective threshold in all grid cells enclosed by the contour.

As expected,  $f_{\text{fg}}$  generally decreases towards fainter magnitudes, with only a few  $z_{\text{ph}} \leq 0.40$  sources at  $r' > 26.0$ . For all

magnitudes, foreground sources with  $r' - i' > 0.5$  are rare. In the brightest three dodeciles, a well-defined region with a distinctive edge towards redder  $r' - i'$  colours exists<sup>12</sup> Although the preferred locus of  $z_{\text{ph}} \leq 0.40$  galaxies depends little on the  $r'$  magnitude, the zone populated by low- $z$  objects becomes more diffuse for fainter sources. The insignificant role of foreground galaxies  $r' > 25.0$  justifies that our background selection includes all galaxies fainter than  $m_{\text{faint}}$ . Furthermore, the secondary role of  $m_{\text{bright}}$  compared to  $m_{\text{faint}}$  becomes clear from Fig. B.1, noticing the small number of  $r' < 20$  galaxies.

Calculating  $f_{\text{fg}}$  for a cluster redshift of  $z_d = 0.80$ , the regions in colour-colour space where a given value of  $f_{\text{fg}}$  is exceeded extend as well towards fainter  $r'$  as towards redder  $g' - r'$  and  $r' - i'$  colours. For  $z_d = 0.80$ , only a small number of background sources remain in the first dodecile, while there are significant foreground objects even in the  $r'_{10} < r' < r'_{11}$  bin.

We adjust our background selection polygon to  $z_d = 0.40$  and  $z_d = 0.80$  by defining criteria based on  $f_{\text{fg}} > 0.25$  contours in the three brightest dodeciles ( $r' < 23.91$ ) of the Deep 1 photo- $z$  catalogue (Table B.1 and yellow polygon in Fig. B.1). We exclude galaxies at  $m_{\text{bright}} \leq r' \leq m_{\text{faint}}$  and matching these criteria from the lensing catalogues. Performing a cross-check for  $z_d = 0.50$ , we confirm the background selection in Paper I to be sensible, although not optimal. In fact, more ‘‘self-calibrations’’ can be achieved by combining three-colour photometry with photo- $z$  catalogues (Klein et al., in prep.).

## Appendix C: Details of photo- $z$ analysis

### C.1. Spectroscopic calibration

Because our photo- $z$  catalogue for the CFHT CL 1701+6414 field was distilled from only four bands, three of which have rather shallow exposure time (Table 5), we tested its quality by comparison with publicly available SDSS spectroscopy redshifts of the same field. SDSS spectra are only available for a selection of the brightest ( $r' \lesssim 19$ ) sources, with a total of 88 matches for the  $\approx 270\,000$  object photo- $z$  catalogue. Out of the 58 sources flagged as good by BPZ in all four filters, 45 are identified as normal galaxies by SDSS, nine are identified as stars, and four as QSOs. Figure C.1 displays  $z_{\text{ph}}$  as a function of  $z_{\text{spec}}$  of the matched sources for which the BPZ quality parameter ODDS is  $o > 0.7$ . The size of the symbols in Fig. C.1 (star symbols

<sup>12</sup> Towards very blue  $r' - i'$  colours, few galaxies are found in the CFHTLS D1 catalogue, basically all of them at low  $z < 0.4$  redshift. This can be seen from the contours in Fig. B.1 which follow the irregular shape of the point cloud. We choose a conservative  $\min(r' - i') = -1.0$  limit for the selection polygons.

**Table B.1.** Cuts defining the polygons used for background selection for the  $z \approx 0.40$  and  $z = 0.80$  clusters, based on the colours of foreground galaxies (Fig. B.1).

Redshift	$\min(r' - i')$	$\max(r' - i')$	$\min(g' - r')$	$\max(g' - r')$	$\beta$	$\min(s_\beta)$	$\max(s_\beta)$
$z = 0.4$	-1.0	0.7	0.1	1.6	2.5	-3.5	0.5
$z = 0.8$	-1.0	1.2	0.3	1.7	1.5	-3.0	0.7

**Notes.** We specify the values of  $g' - r'$ ,  $r' - i'$ , and  $s_\beta = \beta(r' - i') - (g' - r')$  at the edges of the exclusion polygons for  $m_{\text{bright}} < r' < m_{\text{faint}}$ .

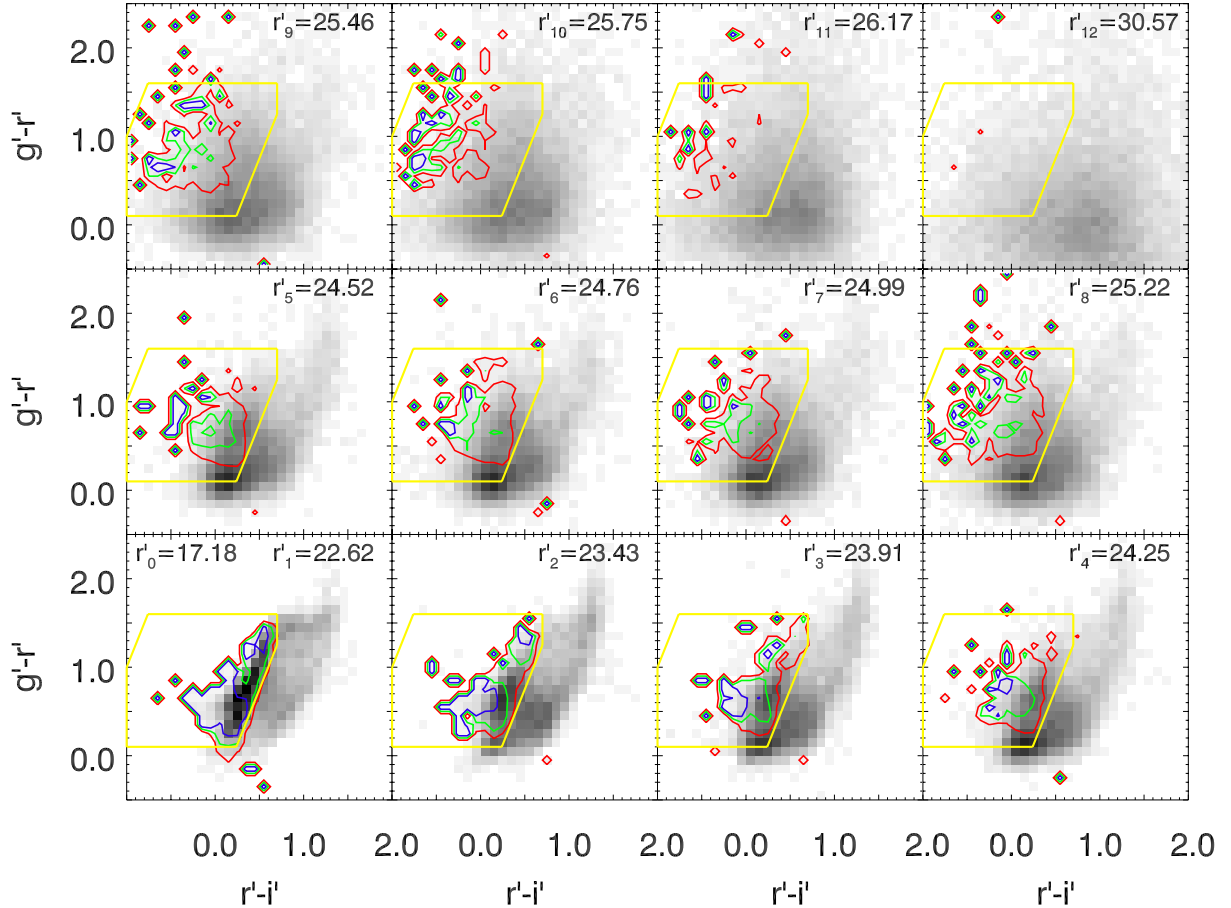


**Fig. B.1.** Fraction of  $z_{\text{ph}} \leq 0.40$  galaxies in the Deep 1 (Ilbert et al. 2006) field as a function of their  $g' - r'$  and  $r' - i'$  colours and  $r'$  magnitude. Each panel shows a dodecile of the photo- $z$  catalogue, i.e. one of twelve equally populated magnitude bins, where the  $k$ -th dodecile includes all galaxies  $r'_{k-1} \leq r' < r'_k$ . In each panel, the number  $N_{ij}$  of galaxies within cells of mesh size  $\Delta(g' - r') = \Delta(r' - i') = 0.1$  is shown, using the same grey scale  $\propto \sqrt{N_{ij}}$ . White grid cells are empty. The red, green, and blue contours enclose regions in which 25% (50%, 75%) of galaxies have a  $z_{\text{ph}} \leq 0.40$ . Based on the distribution of  $z_{\text{ph}} \leq 0.40$  galaxies in the three brightest dodeciles, we define the yellow polygon (see Table B.1), in order to remove foreground galaxies from the CL0159+0030 and CL0809+2811 fields.

for stars, filled circles for normal galaxies, and filled squares for QSOs) corresponds to the value of  $o$ .

Generally, the photo- $z$  uncertainties (given by the BPZ  $Z_{\text{B\_MIN}}$  and  $Z_{\text{B\_MAX}}$  parameters) are large, although the sources in Fig. C.1 rank among the brightest in the catalogue. Nevertheless, the  $z_{\text{ph}}$  estimates for normal galaxies seem to follow a remarkably narrow and monotonic function of  $z_{\text{spec}}$ , in the range  $0 < z_{\text{spec}} \leq 0.45$  probed by the SDSS spectral targets in Fig. C.1. The step at  $z_{\text{spec}} \approx 0.10$ , below which galaxies get assigned  $z_{\text{ph}} \approx 0.0$  and above which they are overestimated to be at  $z_{\text{ph}} \approx 0.3$ , can be explained by the lack of a  $u'$  filter crucial for detecting the 400 nm break at these redshifts. In particular, this applies to galaxies in the  $z \approx 0.22$  structures in the foreground to CL 1701+6414, as exemplified by the  $z_{\text{ph}} \approx 0.40$  for one of the A 2246 BCG candidates at  $z_{\text{spec}} \approx 0.235$ .

Photo- $z$  estimates for the highest redshift ( $z \approx 0.45$ ) galaxies with SDSS spectra are stunningly accurate, despite the large uncertainties. The overall trend seen in Fig. C.1 is consistent with the results of the CFHTLS-Archive-Research Survey (Erben et al. 2009). In their analogous comparison of CFHT BPZ photo- $z$ s to SDSS spectra, they find a turnover to  $z_{\text{ph}} < z_{\text{spec}}$  for  $z_{\text{spec}} \gtrsim 0.45$  (for a small absolute number of such galaxies).

It is a lucky coincidence that the  $z_{\text{ph}}-z_{\text{spec}}$ -relation intersects the dotted equality line precisely at the redshift of our cluster of interest. There are six galaxies  $0.448 < z_{\text{spec}} < 0.457$  among the SDSS spectral targets (inlay in Fig. C.1), while there are none in the  $0.36 < z_{\text{spec}} < 0.44$  range. These six include the BCG of CL 1701+6414 at  $z_{\text{spec}} = 0.4523 \pm 0.0001$ , for which BPZ returns  $z_{\text{ph}} = 0.45 \pm 0.19$ . However, even the closest of the other five is separated by 12'0 or 4.0 Mpc in projection and

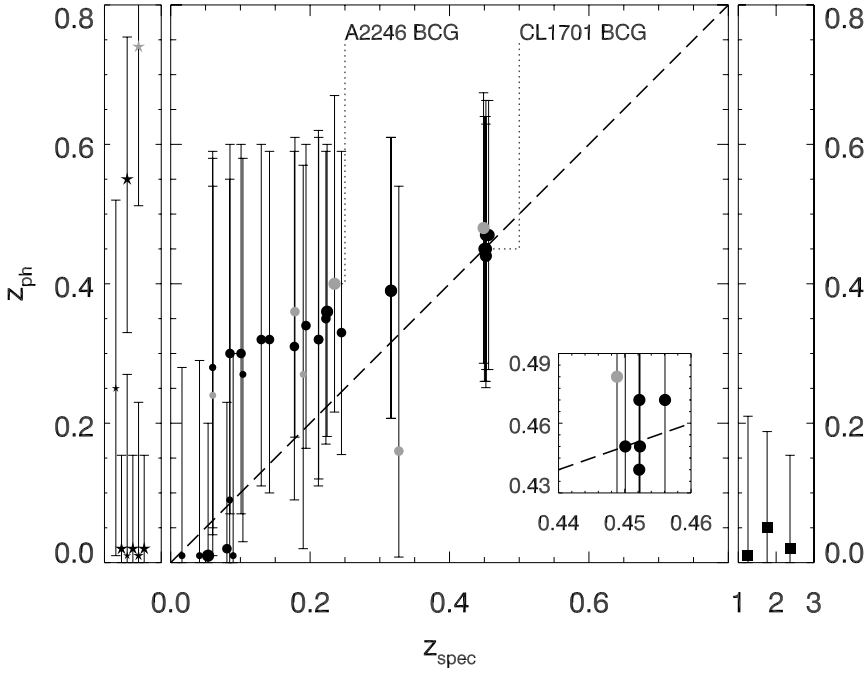


**Fig. C.1.** CFHT photometric redshifts plotted against spectroscopic redshifts from SDSS. The *left panel* (star symbols) shows the  $z_{\text{ph}}$  for objects identified as stars in SDSS, the *middle panel* (filled circles) for normal galaxies, and the *right panel* (filled squares) for QSOs. A small inlay gives a zoomed version for  $z_{\text{spec}} \approx 0.45$  galaxies. The size of the symbols marking the photo- $z$  estimate correspond to the quality parameter  $o$  (ODDS): big symbols for  $o > 0.9$ , medium-sized symbols for  $0.8 < o < 0.9$ , and small symbols for  $0.7 < o < 0.8$ . Error bars for the  $z_{\text{ph}}$  give the uncertainty interval defined by the BPZ  $Z\_B\_MIN$  and  $Z\_B\_MAX$  parameters. Objects inside a flagged region of one of the CFHT images ( $CANDMASK=1$ ) are shown in grey.

thus not part of or closely interacting with CL 1701+6414. Still, its  $z_{\text{spec}} = 0.4522 \pm 0.0001$  indicates they might belong to the same large-scale structure.

The photo- $z$  estimates for QSOs (right panel of Fig. C.1) are clearly off, which doesn't come as a surprise as there is no QSO spectrum among the templates employed by BPZ. Although five out of eight stars in Fig. C.1 (left panel) get assigned  $z_{\text{ph}} \leq 0.02$ , there are also three cases in which our photo- $z$  catalogue suggests higher  $z_{\text{ph}}$  for objects that by visual inspection and SDSS classification clearly stellar: The available CFHT photometry alone does not allow for an accurate star/galaxy classification.

## C.2. Matching with MMT

To investigate what benefit the four-band photo- $z$ s yield, once the usual selection of galaxies by magnitude and half-light radius (Sect. 2.4) is applied, we now match the photo- $z$  catalogue with the MMT KSB catalogue. We first notice that although 95.6% of galaxies in the MMT KSB catalogue are matched bijectively to a CFHT photo- $z$  source, only 20.4% of the MMT lensing sources satisfy the quality criteria of four usable CFHT bands ( $NBPZ\_GOODFILT=4$ ),  $o > 0.8$ , and no masking ( $CANDMASK=0$ ). We call these estimates *high-quality* photo- $z$ s.

Counter-intuitive at the first glance, 76% of the high-quality matches have  $z_{\text{ph}} > 0.5$ , i.e. are likely background galaxies to CL 1701+6414. However, this effect can be traced back to the near-absence of high-quality estimates of  $z_{\text{ph}} < 0.3$ . This is consistent with our expectation from the comparison to the spectroscopic redshifts (Fig. C.1), where the lack of a  $u'$  filter systematically offsets  $z_{\text{ph}}$  for  $z_{\text{spec}} < 0.45$  galaxies to higher values. The  $z_{\text{ph}}$  distribution derived from the four-band CFHT data deviates far from the redshift distributions known from well-studied photo- $z$  fields (Ilbert et al. 2006, 2009, also see Fig. B.6 in Paper I). This holds in particular for the high-quality sub-catalogue which, containing brighter galaxies on average, traces a different population than our MMT lensing catalogue.

The upper panel of Fig. C.2, showing the magnitude distributions of the high-quality photo- $z$  catalogue (solid blue line)

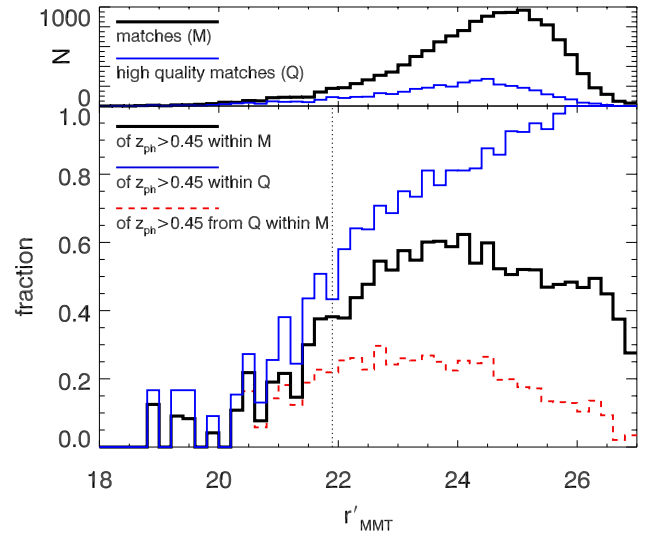


**Fig. C.2.** *Upper panel:* histograms of the MMT-photo- $z$  matched catalogue as a function of MMT  $r'$  magnitude: Plotted are all matches (thick black line) and the subset of matches with photo- $z$ s passing all quality criteria (“high quality”, blue line). *Lower panel:* fractions of galaxies  $z_{\text{ph}} > 0.45$  within: all MMT-photo- $z$  matches (thick black line), the “high quality” matches (blue line), and of high-quality matches  $z_{\text{ph}} > 0.45$  within M (dashed red line). A thin dotted line gives the magnitude cut at  $m_{\text{faint}} = 21.9$ .

compared to all matches (thick black line) demonstrates that high-quality photo- $z$ s tend to belong to brighter galaxies. This can be seen from the modes of the histograms and is not surprising given the necessary detection in the shallow  $g'i'z'$  images. While 98.5% of the sources in the MMT galaxy catalogue get matched to a photo- $z$  galaxy, only for 26.7% the photo- $z$  passes all quality cuts.

In particular, the decline with magnitude of the fraction of high-quality matches affects the fraction of background galaxies with respect to CL 1701+6414 at  $z = 0.45$  using our photo- $z$ s: considering high-quality matches only (solid blue curve in the

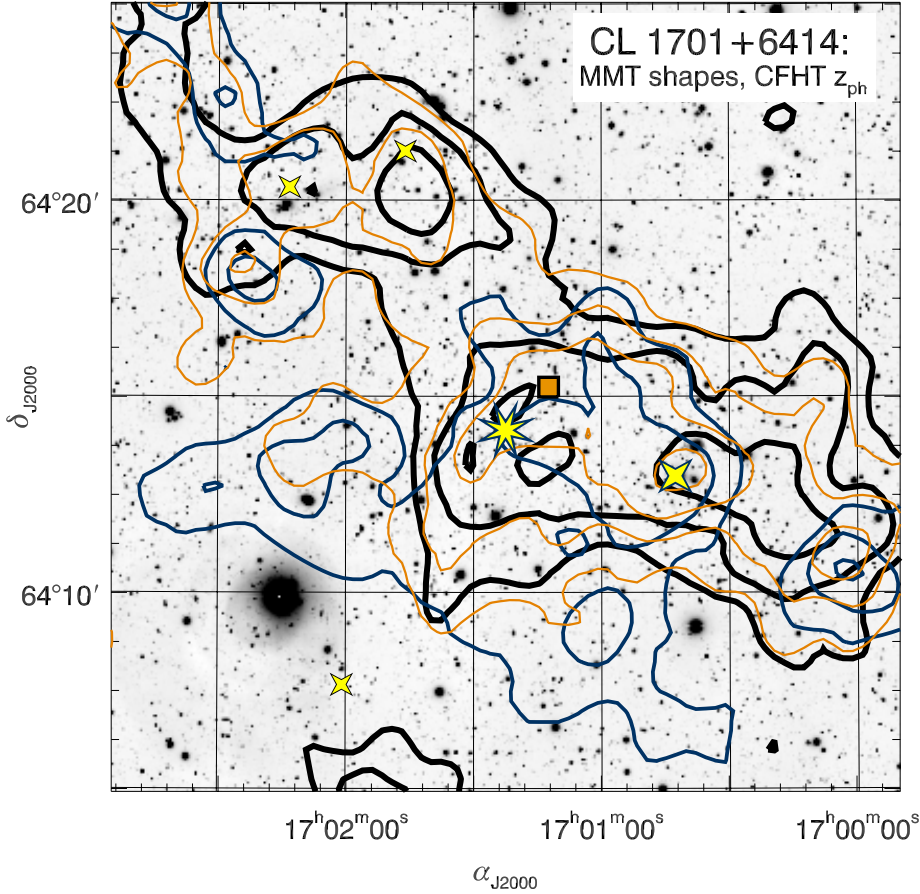


**Fig. C.3.**  $S$ -statistics in the CL 1701+6414 field using the CFHT photo- $z$  catalogue. Thick black contours mark the shear signal from the  $z_{\text{ph}} < 0.45$  catalogue, medium-thick blue contours are derived from the complementary  $z_{\text{ph}} \geq 0.45$  sources. Thin orange contours show the signal from the complete MMT galaxy catalogue. All contours start at  $S = 1$  and are spaced by  $\Delta S = 1$ . The underlying image and other contours are the same as in Fig. 3.

lower panel of Fig. C.2), the fraction of “photometric background” ( $z_{\text{ph}} > 0.45$ ) increases strongly with MMT  $r'$  magnitude. In fact, all of the few  $r'_{\text{MMT}} > 25.8$  high-quality matches show  $z_{\text{ph}} > 0.45$ . With respect to the complete catalogue (thick black line), however, the fraction of photometric background galaxies peaks at  $r'_{\text{MMT}} \approx 24$  and  $\sim 0.6$  and decreases towards fainter  $r'_{\text{MMT}}$ . The fraction of high-quality  $z_{\text{ph}} > 0.45$  galaxies compared to all matches (red dashed line in Fig. C.2) runs rather flat with  $r'_{\text{MMT}}$ , never exceeding 0.3 and subsuming only 15.9% of all matches.

We conclude that the quality of the CFHT data entering the photo- $z$  estimation makes possible a rough estimation of a normal galaxy’s redshift, i.e. to decide if it is more likely to be in the foreground or in the background, but not a precise redshift distribution from which  $\langle \beta \rangle$  could be inferred more precisely than using a proxy photo- $z$  catalogue of high quality (Sect. 2.5).

### C.3. A photo- $z$ shear catalogue

The photo- $z$ s drawn from the CFHT  $g'r'i'z'$  bands provide us with a rough redshift estimate. In order to test whether this information can be used to disentangle the shear signals of CL 1701+6414 and the foreground structure, in particular A 2246, we divide the MMT galaxy catalogue: galaxies with  $z_{\text{ph}} < 0.45$  are sorted into the “photo- $z$  foreground” catalogue, galaxies with  $z_{\text{ph}} \geq 0.45$  are sorted into the “photo- $z$  background” catalogue. Because of the poor quality of most photo- $z$  estimates we expect only a crude selection.

Figure C.3 shows the  $S$ -maps resulting from these two catalogues, overlaid on the MMT  $r'$ -image in the same fashion as for Fig. 3. Thick black contours denote iso- $S$ -contours from

the photo- $z$  background catalogue, including 49.9% of the lensing catalogue ( $10.3 \text{ galaxies/arcmin}^{-2}$ ). Solid blue contours in Fig. C.3 are drawn from the complementary photometric foreground catalogue; the signal from the complete galaxy catalogue is shown as thin orange contours.

The morphology of the  $S$ -peaks in the photo- $z$  background map follows in its main features the complete catalogue, as we expect from a sample of true  $z > 0.45$  galaxies. With  $S_{\text{max}} = 3.14$ , the peak to be associated with CL 1701+6414 is nearly as strong as for the full catalogue, and closer to the cluster’s ROSAT position. The A 2246 peak shows a similar high fraction of the complete catalogue signal, but the two clusters appear to be better separated. The photo- $z$ -foreground  $S$ -morphology bears little resemblance to Fig. 3: although we still measure  $S \approx 2$  close to the position of CL 1701+6414, it can not be seen as a distinct peak. A 2246 is detected just below  $3\sigma$ , with  $S > 3$  only measured for the “SW peak”. This is consistent with our expectations: As A 2246 is at lower redshift, some signal should persist in a true foreground catalogue.

Re-defining the photo- $z$  catalogue such that it only contains high-quality photo- $z$ s  $> 0.45$  (cf. Sect. C.2) results in a good resolution between the  $S$ -signals of the two main clusters but such catalogue suffers from the sparsity of sources ( $4.8 \text{ galaxies/arcmin}^{-2}$ ).

Despite the outcome of this experiment matching our expectations, we keep in mind the typical uncertainty of  $\sigma(z_{\text{ph}}) \approx 0.25$  even for the high-quality photo- $z$ s (Fig. C.1), similar to the redshift separation of CL 1701+6414 and A 2246. Hence, the photo- $z$  selection using the available data is not inherently better than the Sect. 4.1 magnitude cut. Nonetheless, the CFHT photo- $z$ s and lensing measurements confirm the detection of

CL 1701+6414 as a shear source distinct from A 2246 and give credibility to its mass estimate, the aim of our investigations.

## Appendix D: Notes on individual clusters

### D.1. CL 0159+0030

Being located in the SDSS equatorial strip, CL 0159+0030 has been detected by Goto et al. (2002) in the SDSS commissioning data, using their photometric “cut and enhance” cluster finder. Plionis et al. (2005) followed up Goto et al. (2002) cluster candidates using archival *XMM-Newton* observations. From the 3800 s PN observation Plionis et al. (2005) analysed, only a  $3\sigma$  upper flux limit of  $2.1 \times 10^{-14}$  erg cm $^{-2}$  s $^{-1}$  in the 0.5–2.0 keV energy range could be inferred. This non-detection disagrees both with the flux of  $3.3 \pm 0.4 \times 10^{13}$  erg cm $^{-2}$  s $^{-1}$  Vikhlinin et al. (2009a) measure for CL 0159+0030 with ROSAT and with their *Chandra* flux of  $3.6 \times 10^{13}$  erg cm $^{-2}$  s $^{-1}$  in the same band.

### D.2. CL 0230+1836

For CL 0230+1836, there are neither detections of the cluster itself, independent from the 400d survey, nor other galaxy clusters within a 20' radius listed in NED. To our knowledge, we are the first to study this high- $z$  cluster with deep optical observations.

### D.3. CL 0809+2811

We hypothesise that CL 0809+2811 is identical to ZwCl 0806.5+2822 at  $\alpha_{J2000} = 08^{\text{h}}09^{\text{m}}34^{\text{s}}$ ,  $\delta_{J2000} = +28^{\circ}13'1''$ , a position 1.9 off the CL 0809+2811 ROSAT centre and at similar distance to the bright star in the field, where we do not see a concentration of galaxies. Neither do we observe an overdensity of galaxies at the position of a secondary shear peak with  $S = 2.9$  (Fig. D.3). It is located at  $\alpha_{J2000} = 08^{\text{h}}09^{\text{m}}08^{\text{s}}$ ,  $\delta_{J2000} = +28^{\circ}05'22''$ . No cluster within 3' of this position is known to NED.

### D.4. CL 1357+6232

Lopes et al. (2004) conducted a cluster survey on digitised Second Palomar Observatory Sky Survey plates, using a Voronoi tessellation technique. In their catalogue, they quote a cluster of galaxies at  $\alpha_{J2000} = 13^{\text{h}}57^{\text{m}}22^{\text{s}}$ ,  $\delta_{J2000} = +62^{\circ}33'11''$ , where there is no source in the MegaCam image. Using the relation found between  $r'$  magnitude,  $g' - r'$  colour and  $z_{\text{spec}}$  for a subsample of clusters with spectroscopic redshifts, Lopes et al. (2004) assign  $z = 0.19$  to their detection. (NSCS J135722+623311, their #7243). Noting that the position of NSCS J135722+623311 is only 16'' from the ROSAT centre of CL 1357+6232, we speculate that it might be the result of a confusion of CL 1357+6232 with two bright galaxies to its east, one of which (SDSS J135723.83+623246.1) has a measured redshift of  $z = 0.078$ .

### D.5. CL 1416+4446

In addition to CL 1416+4446, we detect two other shear peaks at  $>3\sigma$  significance to the west and south-west of CL 1416+4446. Lopes et al. (2004) list a cluster NSCS J141623+444558 in their catalogue which, by NED, is identified with CL 1416+4446. Furthermore, Lopes et al. (2004) detected a cluster of galaxies at  $\alpha_{J2000} = 14^{\text{h}}16^{\text{m}}09^{\text{s}}$  and  $\delta_{J2000} = +44^{\circ}38'51''$ , with a redshift of  $z = 0.39$ . Less than 2' north-east of these coordinates we find the south-western shear peak which coincides with the  $g' = 20.1$  galaxy SDSS J141613.33+443951.3. For this source, SDSS (Adelman-McCarthy et al. 2008) quotes a spectroscopic redshift of  $z = 0.397$ . Note that the brighter galaxy SDSS J141603.01+443725.1, located 2' further to the south-west from the Lopes et al. (2004) cluster position has an SDSS  $z_{\text{spec}} = 0.310$  and does not correspond to an  $S$ -peak.

Barkhouse et al. (2006) detected a galaxy cluster at  $\alpha_{J2000} = 14^{\text{h}}16^{\text{m}}09^{\text{s}}6$ ,  $\delta_{J2000} = +44^{\circ}44'02''4$ , coincident with the western shear peak, comparing archival *Chandra* data to optical  $g'r'i'$  observations in the *Chandra* Multiwavelength Project. They assign a redshift  $z = 0.427$  to the cluster, designated BGV 50. In the same *Chandra* observation, Barkhouse et al. (2006) identified another cluster, BGV 53 at  $\alpha_{J2000} = 14^{\text{h}}16^{\text{m}}27^{\text{s}}6$  and  $\delta_{J2000} = +44^{\circ}52'44''4$  and a redshift of  $z = 0.452$ , which does not correspond to a bright galaxy in the MegaCam image or a peak in the  $S$ -statistics.

Out of the three confirmed clusters in the field, CL 1416+4446 not only is the only 400d X-ray cluster and the strongest lensing detection, but also appears to be the optically richest system in the MegaCam  $r'$ -band image. Therefore, CL 1416+4446 possibly presents the most massive system in a physically interacting super-structure, indicated by the  $z \approx 0.40$  redshifts of all mentioned clusters. Judging by the X-ray morphology, Vikhlinin et al. (2009a) classify CL 1416+4446 as a relaxed system, though. We conclude that the CL 1416+4446 field qualifies as an interesting candidate for further investigation concerning the existence of a super-cluster.

### D.6. Cross-identifications of CL 1701+6414

Vikhlinin et al. (1998), on whose 160d ROSAT catalogue the 400d sample builds (cf. Burenin et al. 2007) detect four clusters in the field: VMF 189 (A 2246), VMF 190 (CL 1701+6414), VMF 191, and VMF 192. In an independent ROSAT analysis, Donahue et al. (2002) detect these same four clusters plus RX J1702+6407, which we do not detect in WL. The redshift of  $z = 0.7$  found for the Donahue et al. (2002) optical counterpart of CL 1701+6414 deviates from the redshift of  $z = 0.45$  measured by Burenin et al. (2007) and all other references. CL 1701+6414 is further listed as RX J1701.3+6414 in the Bright Serendipitous High-Redshift Archival ROSAT Cluster sample (Bright SHARC, Romer et al. 2000).

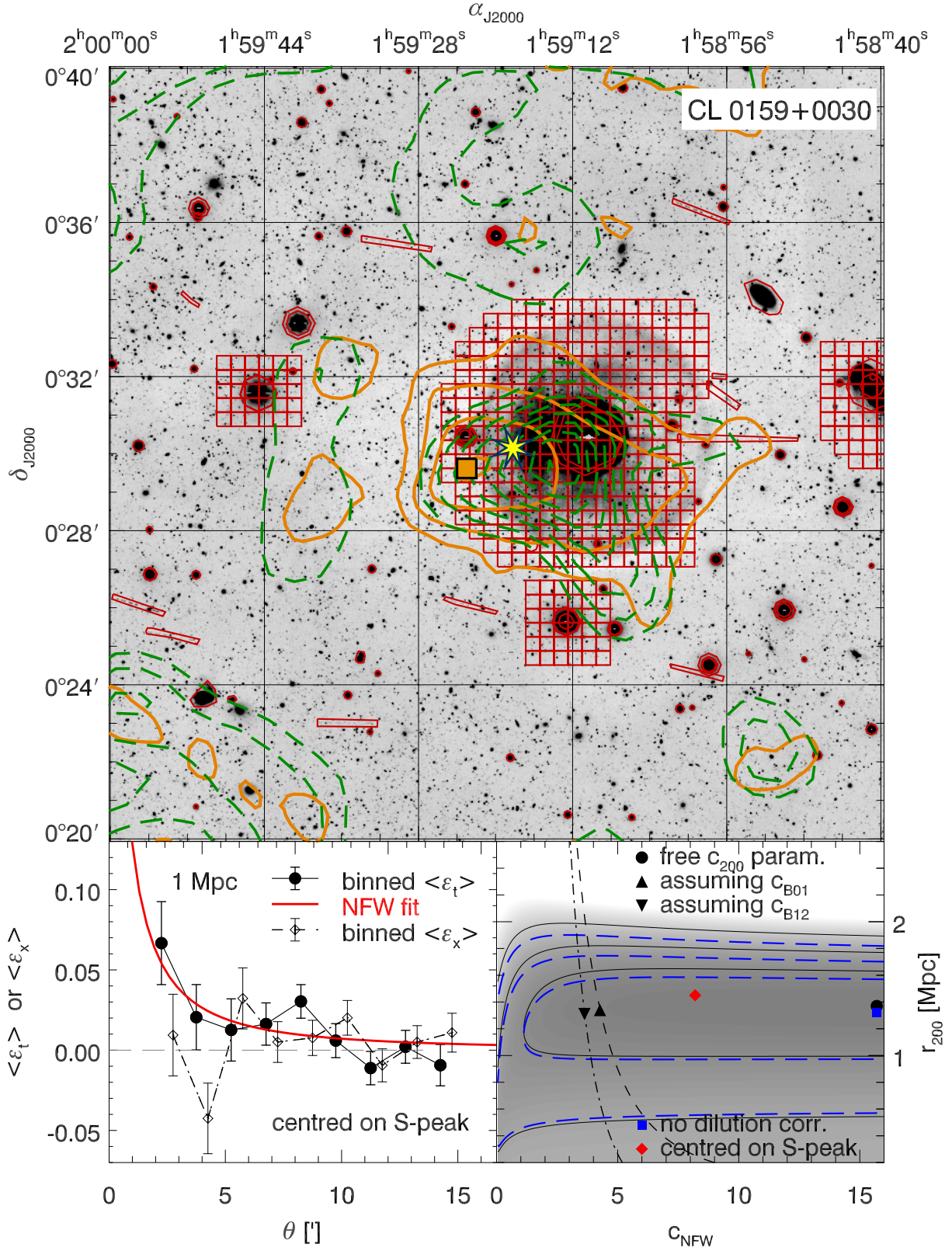


**Fig. D.1.** Like Fig. 2, but for CL 0159+0030. In the plot of  $r_{200}$  against  $c_{\text{NFW}}$ , a square and dashed contours denote the model minimising Eq. (3) if no dilution correction is assumed.

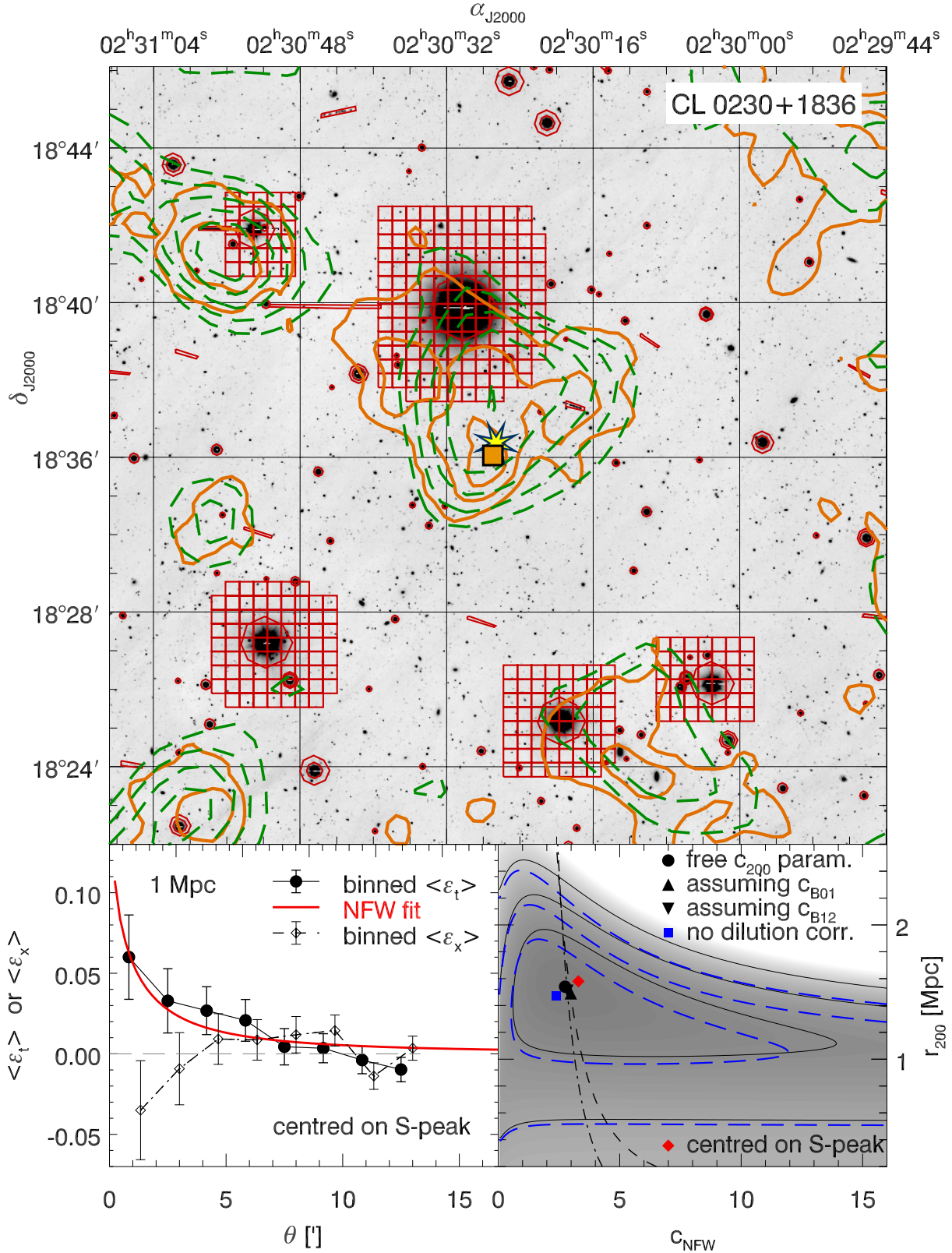


**Fig. D.2.** Like Fig. D.1, but for CL0230+0030. Note that, in the *lower right panel*, the filled circle and downward triangle, denoting the best parameters for the free- $c_{\text{NFW}}$  and B12-models are almost coincident.

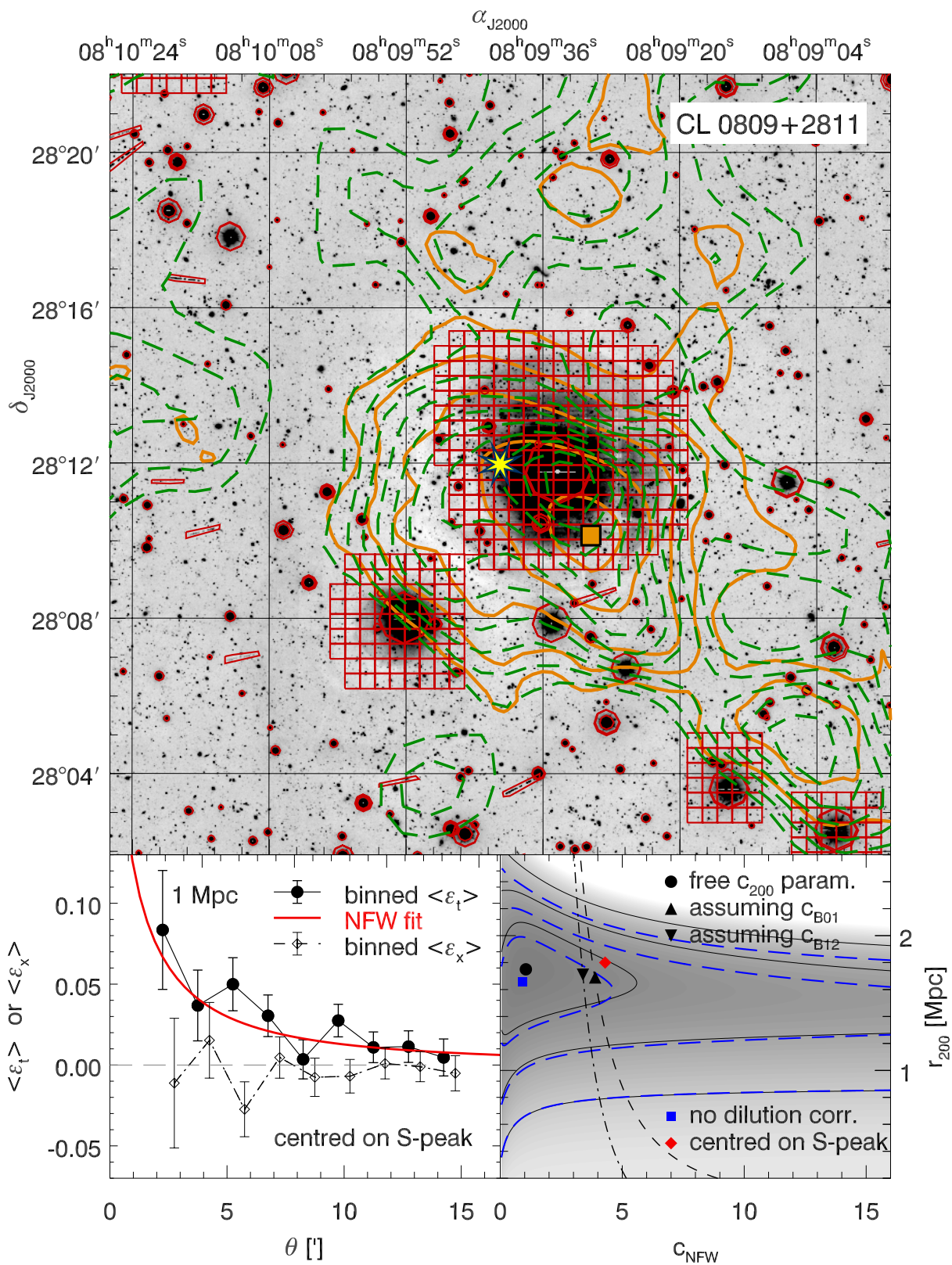
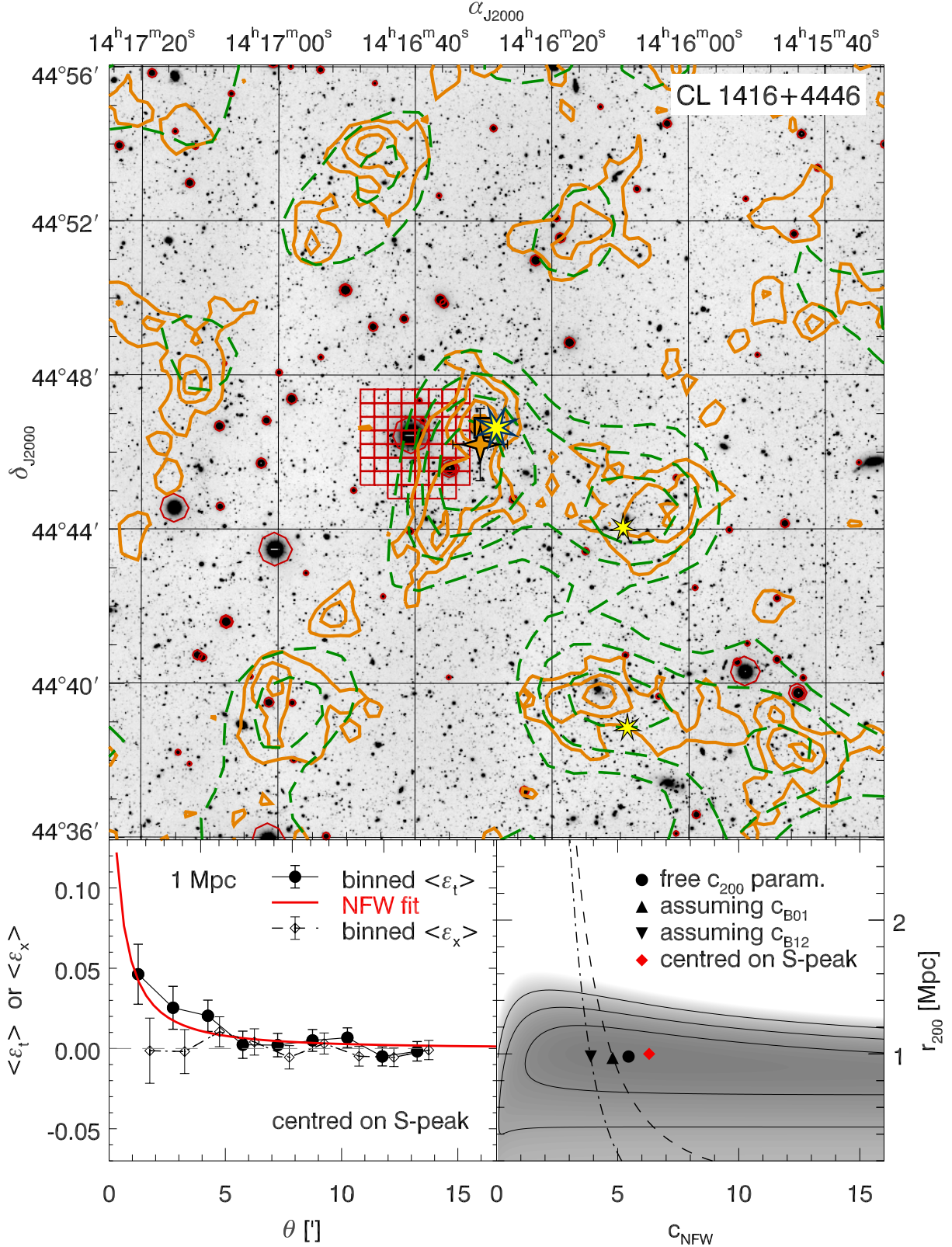


Fig. D.3. Like Fig. D.1, but for CL 0809+2811.



**Fig. D.4.** Like Fig. 2, but for CL 1416+4446. Small star symbols indicate the positions of further clusters in the field, which might be in physical connection to CL 1416+4446 as parts of a super-cluster.